

INFORMATION TO USERS

This manuscript has been reproduced from the microfilm master. UMI films the text directly from the original or copy submitted. Thus, some thesis and dissertation copies are in typewriter face, while others may be from any type of computer printer.

The quality of this reproduction is dependent upon the quality of the copy submitted. Broken or indistinct print, colored or poor-quality illustrations and photographs, print bleedthrough, substandard margins, and improper alignment can adversely affect reproduction.

In the unlikely event that the author did not send UMI a complete manuscript and there are missing pages, these will be noted. Also, if unauthorized copyright material had to be removed, a note will indicate the deletion.

Oversize materials (e.g., maps, drawings, charts) are reproduced by sectioning the original, beginning at the upper left-hand corner and continuing from left to right in equal sections with small overlaps.

Photographs included in the original manuscript have been reproduced xerographically in this copy. Higher quality 6" x 9" black and white photographic prints are available for any photographs or illustrations appearing in this copy for an additional charge. Contact UMI directly to order.

**Bell & Howell Information and Learning
300 North Zeeb Road, Ann Arbor, MI 48106-1346 USA
800-521-0600**

UMI[®]

**UNIVERSITY OF OKLAHOMA
GRADUATE COLLEGE**

**CHARACTERIZATION OF IV-VI SEMICONDUCTOR
MATERIALS AND DEVICES BY
FOURIER TRANSFORM INFRARED SPECTROSCOPY**

**A Dissertation
SUBMITTED TO THE GRADUATE FACULTY
In partial fulfillment of the requirements for the
degree of
Doctor of Philosophy**

**BY
I-Na Chao
Norman, Oklahoma
1999**

UMI Number: 9952410

**Copyright 1999 by
Chao, I-Na**

All rights reserved.

UMI[®]

UMI Microform 9952410

Copyright 2000 by Bell & Howell Information and Learning Company.

**All rights reserved. This microform edition is protected against
unauthorized copying under Title 17, United States Code.**

**Bell & Howell Information and Learning Company
300 North Zeeb Road
P.O. Box 1346
Ann Arbor, MI 48106-1346**

**©Copyright by I-Na Chao 1999
All Rights Reserved.**

**CHARACTERIZATION OF IV-VI SEMICONDUCTOR
MATERIALS AND DEVICES BY
FOURIER TRANSFORM INFRARED SPECTROSCOPY**

**A Dissertation APPROVED FOR THE
SCHOOL OF ELECTRICAL AND COMPUTER ENGINEERING**

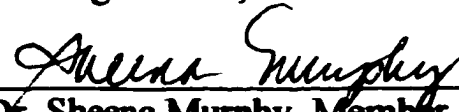
BY



Dr. Patrick J. McCann, Chairman



Dr. Roger Frech, Member



Dr. Sheena Murphy, Member



Dr. Michael Santos, Member



Dr. Zhisheng Shi, Member

ACKNOWLEDGMENTS

I am indebted to Professor Patrick McCann, my thesis advisor, for his guidance and support in seeing me through my doctoral research. My experimental work was made possible by the establishment of the FTIR characterization laboratory and the laser-testing laboratory. Special thanks are due to Dr. Shu Yuan (presently at Nanyang Technological University, Singapore) and Dr. Khosrow Namjou who are instrumental in implementing these facilities. I am also grateful to Dr. Ning Dai who has generously contributed FTIR transmission data on lead strontium selenide materials.

It is a pleasure to acknowledge all my committee members for their involvement as I proceeded with the task of finalizing the dissertation. A much-improved edition of this dissertation would not have been accomplished without their invaluable suggestions and constructive criticism. I thank Professor Zhisheng Shi (School of Electrical and Computer Engineering) for his expert advice on the calculation of refractive index. I thank Professor Roger Frech (Department of Chemistry and Biochemistry), Professor Sheena Murphy (Department of Physics and Astronomy), and Professor Mike Santos (Department of Physics and Astronomy) for the many valuable comments and critical suggestions.

Warm appreciation is extended to Dr. Jerry Crain, Director, Ms. Marita Hardcastle, Assistant to the Director, and Ms. Lynn Halverson, Graduate Program Assistant, for the encouragement and support throughout my graduate study.

This work is funded by the Earth System Science Fellowship program from National Aeronautical and Space Administration. Other funding comes from National Science Foundation and Ekips Technologies, Inc.

TABLE OF CONTENTS

ACKNOWLEDGMENTS	iv
TABLE OF CONTENTS	v
LIST OF TABLES	vii
LIST OF ILLUSTRATIONS	viii
ABSTRACT	x
CHAPTER	
1 INTRODUCTION	1
2 FUNDAMENTALS OF FOURIER TRANSFORM INFRARED SPECTROMETRY	6
3 TRANSMISSION STUDIES OF EPILAYERS GROWN BY MOLECULAR BEAM EPITAXY	13
3.1 Introduction	13
3.2 Growth Procedure	15
3.3 FTIR Spectroscopy Procedures	17
3.4 Experimental Results for PbSe	20
3.5 Experimental Results for PbEuSe	23
3.6 Experimental Results for PbSrSe	28
3.7 Discussions and Summary	33
4 TRANSMISSION STUDIES OF EPILAYERS GROWN BY LIQUID PHASE EPITAXY	37
4.1 Introduction	37
4.2 Growth Procedure	39

4.3	Results of FTIR Characterization	41
4.3.1	Optical Bandgap Energy	41
4.3.2	Effect of cryogenic Cycling	49
4.4	Discussions and Summary	51
5	EMISSION STUDIES OF DIODE LASER PUMPED IV-VI EPILAYERS	53
5.1	Introduction	53
5.2	Photoluminescence Experimental Procedures	54
5.3	Experimental Results	59
5.4	Summary of Experimental Results	77
5.5	Discussions	82
6	EMISSION STUDIES OF COMMERCIAL IV-VI LASERS	88
7	SUMMARY	98
	BIBLIOGRAPHY	103
	APPENDIX A	108
	The Genzel Interferometer	
	APPENDIX B	109
	Frequency Modulation Imposed by Interferometer	
	APPENDIX C	110
	Sampling and Spectral Aliasing	
	APPENDIX D	114
	Important FTIR Measurement Parameters	
	APPENDIX E	117
	Emission Spectra of Tunable Diode Laser #42	

LIST OF TABLES

Table	Title	Page
3.1	IV-VI epilayers grown by MBE on Si (111) and BaF ₂ (111) substrates for ten different samples.	18
3.2	Hole concentrations of four MBE-grown <i>p</i> -type PbEuSe layers.	18
3.3	Calculated refractive index of Pb _{1-x} Sr _x Se	33
4.1	Structure of the MBE-grown substrates used for the growth of IV-VI layers on Si(100) by LPE.	40
4.2	LPE layer composition and thickness for six different samples	40
5.1	Structure of five LPE-grown samples used in photoluminescence experiments.	58
5.2	Photoluminescence energies of PbSeTe from 5 K to 342 K	79
6.1	Single stable modes of a IV-VI tunable diode laser at various current and temperature settings.	91

LIST OF ILLUSTRATIONS

Figure	Title	Page
2.1	Schematic of a simple Michelson interferometer.	7
2.2	Schematic of interferogram/spectrum pairs.	10
3.1	FTIR transmission spectra of PbSe at three temperatures.	21
3.2	Fundamental absorption edge energies vs. temperature plot for PbSe.	23
3.3	FTIR transmission spectra of $Pb_{1-x}Eu_xSe$ layers on Si(111) at low and room temperatures.	24
3.4	FTIR transmission spectra of $Pb_{1-x}Eu_xSe$ layers on Si(111) at room temperature.	25
3.5	Absorption edge energy as a function of europium content in $Pb_{1-x}Eu_xSe$.	26
3.6	FTIR transmission spectra of p -PbEuSe epilayers with Different carrier concentrations.	27
3.7	FTIR transmission spectra for $Pb_{1-x}Sr_xSe$ on $BaF_2(111)$.	28
3.8	Absorption edge energy as a function of Sr content for $Pb_{1-x}Sr_xSe$.	29
3.9	Refractive index plots for $Pb_{1-x}Sr_xSe$ at room temperature.	32
4.1	FTIR transmission spectra of PbSe at two temperatures.	42
4.2	FTIR transmission spectra of PbSnSe, [Sn]=3%.	43
4.3	FTIR transmission spectra of PbSnSe, [Sn]=5%.	44
4.4	FTIR transmission spectra of PbSnSe, [Sn]=6%.	45
4.5	FTIR transmission spectra of PbSnSe, [Sn]=7%.	46
4.6	FTIR transmission spectra of PbSnSe, [Sn]=10%.	47
4.7	Absorption edge energy as a function of europium content in $Pb_{1-x}Sn_xSe$.	48
4.8	FTIR transmission spectra for two PbSnSe samples before and after cryogenic cooling.	49
5.1	Schematic of Photoluminescence experimental setup.	55
5.2	PL spectrum of GaInSb at 82 K.	58
5.3	PL spectrum of a IV-VI sample before normalization.	59

5.4	PL spectra of PbSeTe (sample Z26) at 82 K and two pump laser current levels.	61
5.5	PL spectra of PbSeTe (sample Z26) at 81 K and three pump laser current levels.	61
5.6	PL energy and intensity vs. pump laser current plots for PbSeTe (sample z26).	62
5.7	PL spectrum of PbSeTe (sample Z26) at 81 K showing crystal field splitting.	62
5.8	PL spectra of PbSeTe (sample Z26) at 274 K to 320 K.	64
5.9	PL spectra of PbSeTe (sample Z26) at 330 K to 342 K.	65
5.10	PL energy vs. temperature plot for PbSeTe (sample Z26).	68
5.11	Room temperature PL spectra of PbSeTe (sample C3).	69
5.12	Room temperature PL spectrum of PbSnSeTe (sample C36).	69
5.13	PL spectra for four different samples at two temperatures.	70
5.14	PL spectra of PbSnSeTe (sample C9) at 308 K to 335 K.	71
5.15	PL energy vs. temperature plot for PbSnSeTe (sample C9).	75
5.16	Photoluminescence spectrum of PbSeTe at 5 K.	76
5.17	Composite PL spectra of two different PbSeTe samples.	78
5.18	PL energy vs. temperature plots of two PbSeTe samples.	81
5.19	Graphic derivation of sample heating due to pump laser.	82
5.20	Schematic of the defect states in the Parada-Pratt Model	85
6.1	Schematic of experimental setup for measuring laser emission spectra.	89
6.2	Modal distribution of tunable diode laser #42.	93
6.3	Temperature tuning of diode laser emission (TDL #42).	94
6.4	Current tuning of diode laser emission (TDL #42).	95
6.5	Emission spectra of TDL #42 and HITRAN spectra of three different molecules.	97

ABSTRACT

Transmission and photoluminescence properties of IV-VI semiconductor materials grown by molecular beam epitaxy (MBE) and liquid phase epitaxy (LPE) were characterized using a vacuum-bench type Fourier transform infrared (FTIR) spectrometer. Samples for transmission measurements included $\text{Pb}_{1-x}\text{Eu}_x\text{Se}$ ($x = 0\%$, 2.44%, 7.32%) and $\text{Pb}_{1-x}\text{Sr}_x\text{Se}$ ($x = 0\%$, 7.83%, 15.7%, 26.1%) grown by MBE on Si(111) and $\text{BaF}_2(111)$ substrates, respectively. $\text{Pb}_{1-x}\text{Sn}_x\text{Se}$ ($x = 0\%$, 3%, 5%, 6%, 7%, 10%) samples grown by LPE on MBE-prepared Si(100) substrates were also measured. Fundamental absorption edge energies for these alloys were derived from the transmission spectra and their dependence on composition and temperature were reported. Refractive indices for $\text{Pb}_{1-x}\text{Sr}_x\text{Se}$ were calculated based on the interference data. Effects of alloy disorder, impurity and free-carrier absorption, and cryogenic cycling are observed in the transmission spectral data. Photoluminescence experiments performed on LPE-grown PbSe, PbTe, PbSeTe, and PbSnSeTe (liquid tin contents of 5% and 40%) epilayers show unusual, strong, and above bandgap emissions at temperatures ranging from cryogenic to above room temperature. These emissions may be the first direct experimental observation of defect states associated with anion (chalcogen) vacancies theorized three decades ago. These measurements provide useful information for designing structures that will be used for fabrication of mid-IR lasers.

Emissions from a commercial IV-VI semiconductor PbEuSe diode laser were also obtained using a modular type FTIR spectrometer. The laser exhibits wide (up to 4 cm^{-1}) continuous wave, single-mode tuning regions between 90 K to 116 K for currents in the range of 400 mA to 1000 mA. This type of mid-IR laser characterization is very useful for designing laser-based molecular spectroscopy instrumentation.

CHAPTER 1

Introduction

Matter absorbs infrared radiation by interacting with the electric field vector of the electromagnetic wave in a number of ways that lead to, for example, molecular vibrations, electron-hole pair generation, and free carrier absorption. The absorbance differs from one substance to another and is also a function of the frequency of the radiation. This frequency- and constituent-dependent, measurable property of matter has been investigated by spectroscopists using Fourier transform infrared (FTIR) spectroscopy. FTIR spectrometers, equipped with a broadband radiation source, offer a wide infrared spectral coverage from 200 cm^{-1} to $10,000\text{ cm}^{-1}$. In this spectral range, the interaction between matter and radiation ranges from the rovibrational transitions in gases and the vibrational and electronic transitions in solids. The FTIR method has found dozens of industrial applications in which these transitions are probed. For example, semiconductor process gas emissions [1] and interstitial oxygen in silicon wafers [2] are monitored using FTIR spectroscopy.

In the mid-IR spectral region FTIR spectroscopy is an ideal tool for optical characterization of IV-VI semiconductors materials and devices. In addition to the ease of preparing as-grown samples for spectral analysis, the FTIR method is non-invasive and non-destructive. Typically, FT mid-IR absorption spectroscopy uses a broadband radiation source comprised of low-energy photons ($400\text{--}4,000\text{ cm}^{-1}$ or $50\text{--}500\text{ meV}$). These energy levels are much below the activation energies (in the eV range) for chemical reactions. Therefore, optical characterization using FTIR technique is often the appropriate first step in non-invasive study of new semiconductor materials.

FTIR transmission spectroscopy has been used in characterizing IV-VI semiconductor alloys such as PbSeTe, PbSnSeTe, and PbSnSe grown by liquid phase epitaxy (LPE), and PbSe, PbEuSe, and PbEuTe grown by molecular beam epitaxy (MBE). The LPE-grown epilayers include $\text{Pb}_{1-x}\text{Sn}_x\text{Se}_{1-y}\text{Te}_y$ alloys grown on bulk BaF_2 (100) substrates [3, 4] and $\text{Pb}_{1-x}\text{Sn}_x\text{Se}$ alloys on MBE-prepared $\text{PbSe}/\text{BaF}_2/\text{CaF}_2/\text{Si}$ (100) substrates [5]. The MBE-grown epilayers include $\text{Pb}_{1-x}\text{Eu}_x\text{Se}$ alloys grown on CaF_2/Si (111) substrates [6] and $\text{Pb}_{1-x}\text{Eu}_x\text{Te}$ grown on BaF_2 (111) substrates [7]. The FTIR data show that the electronic transitions between the bonding (valence band) and the anti-bonding (conduction band) states in these epilayers can range from 300 cm^{-1} to over 3000 cm^{-1} . Room temperature index of refraction data have been obtained from the PbSnSe [5] and PbEuTe [7] layers. Based on these data, optical confinement in these IV-VI semiconductors can be achieved by controlling the alloy composition (tin or europium concentration).

Coherent mid-IR radiation can be obtained from IV-VI lasers by optical or electrical excitation and the emission spectra can be characterized using a high-resolution FTIR spectrometer. The emission spectra can provide information such as the temperature and current tuning range and the modal behavior of the laser [8]. In most commercial IV-VI lasers the resonant cavity is a Fabry-Perot type and the mode behavior differs from one device to the other. This necessitates individual device testing, which poses a challenge for conventional geometry of FT instruments. IV-VI laser emission spectra have been obtained using a conventional vacuum-bench FTIR spectrometer [9], which required major modification in order to accommodate the emission source. The modular spectrometer design recently developed by Oriel Instruments of Stratford, Connecticut has made the FT method much more versatile and accessible for performing device testing.

Since gas molecules have absorption features that are comprised of very closely spaced, discrete lines, a high-resolution radiation source is necessary for resolving these

features. This has been the driving force for the development of high-resolution FTIR spectrometers in the recent decades. Concurrently, diode lasers were shown to be useful tunable high-resolution sources for infrared molecular spectroscopy [10]. Today molecular spectroscopic applications are the primary application of IV-VI diode lasers. Spectral characterization of IV-VI lasers is essential in order to select appropriate laser spectroscopy applications. Presently, commercially available IV-VI tunable diode lasers [11, 12, 13] have achieved a spectral coverage from 700 to 3,300 cm^{-1} with continuous wave (cw) operation. Tunable diode laser (TDL) spectrometers equipped with IV-VI lasers can probe the strong fundamental absorption features in the mid-IR spectral region. IV-VI TDL spectroscopy has the advantages of performing gas sensing such as plasma etching end-point detection [14] with higher speed and smaller components than FTIR spectroscopy.

The major drawback of IV-VI lasers is that they require cryogenic cooling systems, such as liquid nitrogen dewars or closed cycle cryogenic compressors. Using a new laser fabrication method [15], IV-VI alloys can be bonded directly to copper heat sinks after the removal of BaF_2 or Si substrate by dissolving the water-soluble fluoride material. It is predicted that this method has the potential of enabling laser cooling using thermoelectric modules [16], thus eliminating the cost and inconvenience of cryogenic cooling. A low-cost, user-friendly mid-IR TDL spectrometer, if available, could complement or even replace FTIR instruments in many gas-sensing applications.

Preliminary FTIR transmission studies on the IV-VI samples have yielded helpful information on heterostructure laser design, such as composition and temperature dependent bandgap energy and composition and frequency dependent refractive index. However, some IV-VI alloys grown on Si (100) substrates suffer from surface cracks [5], which may compromise the quality of the devices fabricated from these epilayers. The cracks in the PbSnSe are due to the mismatch of thermal expansion coefficients between the substrate and the epilayer. Spectral analysis of thermally

cycled, IV-VI on Si samples suggested that cracking is associated with solid-solution hardening in PbSnSe alloys. Continued work is necessary in order to improve the growth technology, which in turn will help realize the new thermoelectrically cooled IV-VI lasers.

Photoluminescence (PL) spectra of IV-VI epilayers grown on bulk (100) BaF₂ substrates have been obtained using two completely different experimental setups [3, 17]. PL signals [3] associated with transitions across the band gap were observed at low temperatures from PbSe_{0.78}Te_{0.22} and Pb_{0.95}Sn_{0.05}Se_{0.80}Te_{0.20} alloys. PL signals thought to originate from the defect states were observed at low temperatures and room temperature using both experimental setups. The “new” PL energy at room temperature is centered around 3800 cm⁻¹ (2.6 μm) bordering the near- and mid-IR region, which has been accessed only by a few experimental semiconductor lasers.

There has been a strong research interest on extending the III-V room-temperature lasing wavelength to the mid-IR spectral region. Recently, the mid-IR spectral region was accessed by quantum cascade lasers operated in pulsed mode at room temperature [18] and in cw mode at low temperatures [8]. Adding antimony can extend lasing wavelengths of III-V lasers to the mid-IR spectral region but at the expense of cryogenic operating temperature and poor device yield [19]. On the other hand, effort on increasing the operating temperature of IV-VI lasers has resulted in a record-breaking cw operating temperature of 223 K from a PbEuSeTe/PbTe diode laser [20]. The recent success [21] in bonding IV-VI epilayers to copper using the new IV-VI laser fabrication technology promises further increase of cw operating temperature to above 240 K. The new room temperature PL energies observed shows the prospect of not only the elimination of laser cooling systems, but also the extension of the spectral coverage of IV-VI lasers to above 3300 cm⁻¹. It is highly possible that the new-generation IV-VI lasers will dominate the market of high-resolution, mid-IR radiation source in the ever-expanding gas sensing spectroscopic applications.

This work is devoted to the study of the IV-VI materials and lasers using FTIR spectroscopy. FTIR transmission and PL studies were performed on as-grown samples, which are made available using the growth technologies developed at University of Oklahoma. Chapter 2 describes the FTIR instrumentation. Chapter 3 describes transmission studies of layers grown by molecular beam epitaxy. Chapter 4 describes transmission studies of IV-VI layers grown by liquid phase epitaxy. Chapter 5 discusses preliminary results from near-IR diode laser pumping of LPE-grown IV-VI epilayers. Chapter 6 describes measured emission spectra of commercial IV-VI lasers, and chapter 7 provides a summary of this overall work and suggestions for future work.

CHAPTER 2

Fundamentals of Fourier Transform Infrared Spectrometry

Fourier transform infrared spectrometry is a technique in which a key optical device called an interferometer is used to modulate the intensity of radiation based on the principle of optical interference. The modulated radiation contains spectral information, which can be recovered using Fourier transform mathematics. A basic insight into interferometry and the recovery of spectra is helpful in understanding FTIR spectrometry and interpreting the spectral information. This chapter will address these two aspects without exhaustive mathematical representation. Most of the data in this work were collected using a Bruker IFS 113 (sold in US as IBM IR/98) FTIR spectrometer. Instrumental configuration and measurement parameters pertaining to the spectrometer will be addressed as they are related to the above subjects.

The interferometers in commercial FTIR spectrometers operate on the same principle as the version that Michelson invented more than a hundred years ago. A schematic of a simplified Michelson-type interferometer is shown in Figure 2.1. The beamsplitter divides the incoming radiation into two beams with one going to a movable mirror and the other to a fixed mirror. The reflected beams from both mirrors will have traveled through different path lengths when they recombine at the beamsplitter. For the geometry shown, the optical path difference is twice the physical distance that the moving mirror has traveled. In other words, the “optical velocity” V_{op} (cm/s) of the mirror is twice its physical velocity and the optical path difference can be expressed by $\zeta = V_{op} t$. For monochromatic radiation having a

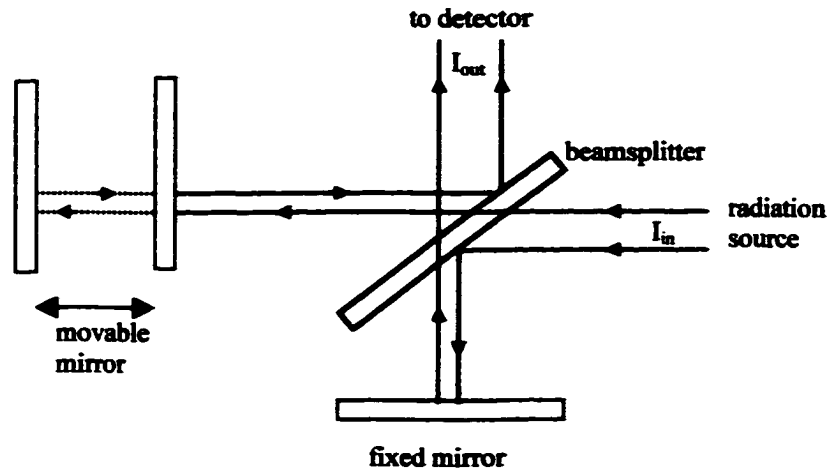


Figure 2.1 Schematic of a simple Michelson interferometer. The incident radiation is shown as two separate beams for ease of visualization of their optical paths. Both the movable and the fixed mirrors are single-sided plane mirrors with the plane perpendicular with each other. The mirrors are equidistant from the beamsplitter when the movable mirror is at rest.

wavelength λ_0 , total constructive and destructive interference occur at $\zeta = n\lambda_0$ and $\zeta = (n+1/2)\lambda_0$, respectively, where n is an integer. The interference pattern is registered at the detector as the change in intensity of the radiation.

The overall variation of the intensity of the monochromatic radiation emerging from an interferometer is described by

$$I_{out}(\zeta) \propto I_{in}(\lambda_0) \cdot [1 + \cos(2\pi\zeta/\lambda_0)] = I_{in}(\nu_0) + I_{in}(\nu_0) \cdot \cos(2\pi\nu_0\zeta) \quad (2-1)$$

where I_{in} and I_{out} are the intensities of the radiation entering and leaving the interferometer, respectively; and ν_0 is the wavenumber ($\nu_0 \equiv 1/\lambda_0, \text{ cm}^{-1}$) of the radiation. The first term of equation (2-1) is just a dc component. What we are interested in is the second term, which shows that the signal leaving the interferometer is sinusoidally modulated. We shall focus on this term in the following discussions.

The intensity of a polychromatic radiation emerging from an interferometer is described by

$$I_{\text{out}}(\zeta) \propto \int_0^{+\infty} I_{\text{in}}(\nu) \cdot \cos(2\pi\zeta\nu) \cdot d\nu \quad (2-2)$$

assuming an ideal beamsplitter whose reflectance and transmittance are frequency independent. The intensity of radiation at the detector is

$$I(\zeta) \propto \int_0^{+\infty} Z(\nu) \cdot I_{\text{in}}(\nu) \cdot \cos(2\pi\zeta\nu) d\nu = \int_0^{+\infty} I(\nu) \cdot \cos(2\pi\zeta\nu) d\nu \quad (2-3)$$

where $I(\nu) \equiv Z(\nu) I_{\text{in}}(\nu)$ and $Z(\nu)$ is the detector response function. Thus the intensity of radiation at the detector is a function of the optical path difference and contains all the spectral information of the source radiation. $I(\zeta)$ is commonly referred to as the interferogram and $I(\nu)$ the spectrum. Mathematically $I(\nu)$ can be retrieved by performing harmonic decomposition of $I(\zeta)$ using cosine Fourier transform, i.e.,

$$I(\nu) \propto \int_0^{+\infty} I(\zeta) \cdot \cos(2\pi\zeta\nu) \cdot d\zeta \quad (2-4)$$

The above discussion illustrates how in theory a spectrum can be computed from the interferogram at infinitely high resolution and scan distance. In practice, the source radiation and the detector's response are band-limited, and the mirror travels a finite distance that is controlled by a servoloop system. Mathematically a finite distance is realized by multiplying $I(\zeta)$ in the right-hand side of Equation (2-4) with a truncation function, which is unity between the scan limits and zero at all other points. If the distance through which the mirror has traveled per scan (one complete back and forth motion) is known, then the spectrum can in practice be computed. The actual spectral

computation, in addition to modifying the interferogram by a truncation function, involves phase correction, apodization, zero fills, and a Fourier transform. A comprehensive coverage on these topics can be found in [22] and will not be presented here.

The Bruker IFS 113 spectrometer used in this study has a dual interferometer configuration that includes a Genzel-type main interferometer (see Appendix A) and a Michelson-type reference interferometer. The mirrors of both interferometers are air bearing driven and are mounted on the same mechanical arm that slides in unison at a constant velocity. The Genzel-type interferometer is based on the same optical principle as the Michelson-type except that the optical path difference is four times the physical distance that the mirror has traveled. The main interferometer modulates the IR radiation of interest while the reference interferometer modulates the radiation of a reference laser and “white” visible light. The spectrum/interferogram pairs for a monochromatic radiation and a broadband radiation are shown in Figure 2.2. The interferogram of the monochromatic radiation is a sinusoidal signal. The interferogram of the broadband radiation represents the summation of the amplitudes of all the component sinusoidal signals. A maximum intensity occurs at the point of zero path difference (ZPD) where the mirror is at rest and all component signals are in phase. The intensity of a monochromatic radiation emerging from an interferometer is said to be modulated at a frequency related to the mirror velocity. The derivation of modulation frequency and the effect of modulation are described in Appendix B.

Since the interferogram is in analog form it must be discretized before it can be analyzed by digital computers. The key operation in analog-to-digital conversion is sampling, a brief discussion of which can be found in Appendix C. In practice, the interferogram of interest is sampled at finite intervals of the optical path difference with the aid of laser interferometry. Since a laser’s interferogram is sinusoidal, each zero crossing on the waveform occurs at uniform increment of optical path difference. The

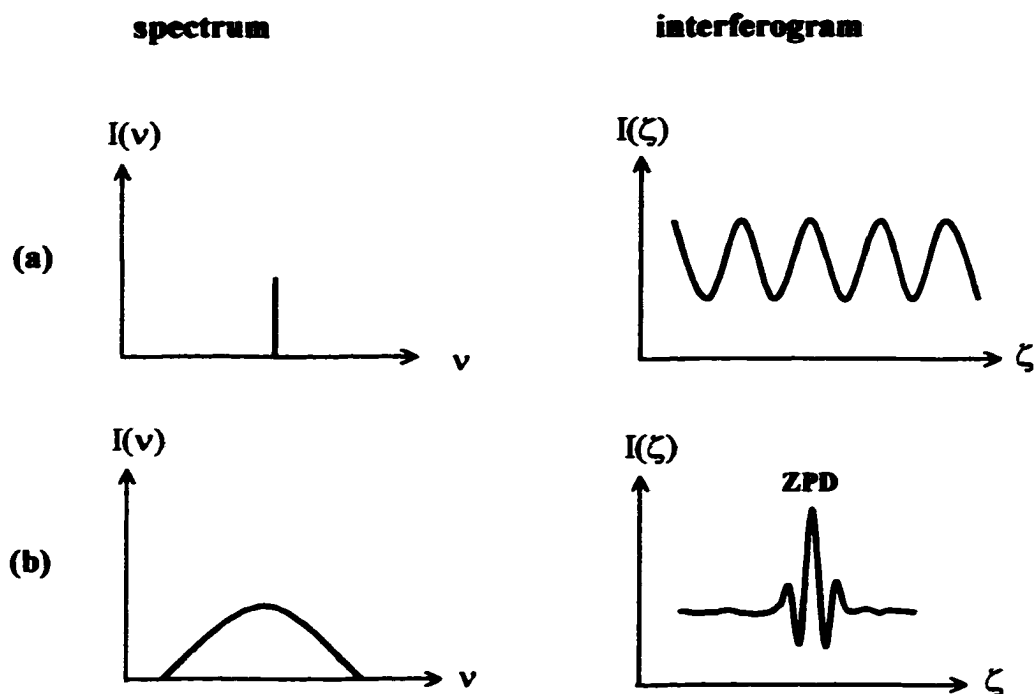


Figure 2.2 Schematics of interferogram/spectrum pairs for (a) a monochromatic radiation, and (b) a broadband radiation. The interferogram of the monochromatic radiation has a cosine waveform caused by the alternation of constructive and destructive interference. The interferogram of the broadband signal has peak intensity at the point of zero path difference (ZPD). The origin of the axes is arbitrary.

zero crossings at successive increments are used as the sampling points for the interferogram of interest. By tracking the number of zero crossings, the position of the mirror is also known and the distance through which it has traveled can be calculated. The emission frequency (wavelength) of helium neon (He-Ne) laser at 15800 cm^{-1} ($0.6329 \text{ }\mu\text{m}$) is used as a wavenumber standard for most commercial FTIR spectrometers. For example, sampling at every other zero crossings corresponds to a sampling interval of $0.6329 \text{ }\mu\text{m}$, sampling at every fourth zero crossings corresponds to an interval of $2 \times 0.6329 \text{ }\mu\text{m}$, and at every eighth zero crossings an interval of 4×0.6329

μm . In terms of sampling frequencies, the above intervals correspond to $15,800\text{ cm}^{-1}$, 7900 cm^{-1} , and 3950 cm^{-1} , respectively.

The signal-to-noise ratio of measurements can be increased using signal averaging techniques. This is achieved by executing multiple scans and co-adding the resultant interferograms. It is critical to start sampling each interferogram at the same place so that data from each scan be co-added at the same sampling points. The ZPD point from a white light interferogram is used to mark the absolute position of the moving mirror, and the peak voltage at this point is used to signal the start of a scan. The zero crossing on the laser interferogram immediately following this voltage burst is then used to signal the start of sampling. Thus the first data point of the interferogram of interest is always sampled at the same optical path difference. Measurements using modern FTIR spectrometers have very high reproducibility. This is, if several spectra of a sample are collected consecutively without varying any test parameters, they will be accurate to within hundredths or thousands of a wavenumber.

According to the sampling theorem the sampling frequency must be at least twice the bandwidth of radiation of interest in order that the spectrum be recovered without aliasing (see Appendix C). For example, a sampling interval of $0.6329\text{ }\mu\text{m}$ can be used to adequately sample radiation having a bandwidth up to $7,900\text{ cm}^{-1}$ and this is normally used in FT spectroscopy. To restrict the bandwidth and to reduce noise, the signal is usually optically and electronically filtered before it is digitized. Band limiting by the Bruker IFS 113 instrument is executed by several measurement parameters. A description of these parameters can be found in Appendix D. An example of spectral aliasing using inappropriately chosen measurement parameters is also given in Appendix D.

An important factor to consider when performing infrared spectroscopy is the presence of water vapor. Water molecules have strong absorption bands in the mid-infrared in the regions of $1500\text{--}1800\text{ cm}^{-1}$ and $3600\text{--}3900\text{ cm}^{-1}$ [23]. There are twenty

and seventeen strong ro-vibrational lines, respectively, in the above mentioned bands whose linestrength is in the magnitude of 10^{-19} cm⁻¹/molecule-cm⁻². The presence of water vapor in the optical path of the spectrometer can affect the instrument, the sample, and the spectrum. Another interfering gas species for mid-IR measurements is CO₂, which has strong absorption band at 2430 cm⁻¹. Therefore dry nitrogen is recommended for purging H₂O and CO₂ from the optical bench of FTIR spectrometers. A vacuum bench flushed with dry nitrogen provides the best measurement environment where mid-IR spectroscopy is performed by an interferometer type instrument.

CHAPTER 3

Transmission Studies of Epilayers Grown by Molecular Beam Epitaxy

3.1 Introduction

IV-VI semiconductor mid-infrared diode lasers have been traditionally fabricated from $\text{Pb}_{1-x}\text{Sn}_x\text{Se}$ and $\text{Pb}_{1-x}\text{Sn}_x\text{Te}$ alloys whose bandgap energies span from 0 to 300 meV depending on composition and temperature. The incorporation of rare earth elements such as europium into IV-VI materials increases the bandgaps even more and extends laser emission toward shorter wavelengths. IV-VI diode lasers operating in the range of 3–8 μm have been fabricated using MBE-grown $\text{Pb}_{1-x}\text{Eu}_x\text{Se}$ alloys on PbSe substrates [13, 24]. Another attractive materials system for fabricating mid-infrared lasers is $\text{Pb}_{1-x}\text{Sr}_x\text{Se}$. Like europium, the addition of strontium also extends laser emission to shorter wavelengths [25].

$\text{Pb}_{1-x}\text{Eu}_x\text{Se}$ and $\text{Pb}_{1-x}\text{Sr}_x\text{Se}$ alloys have been grown on (111)-oriented BaF_2 substrates by MBE [26]. Preliminary studies indicated no difference between the refractive indices of PbEuSe and PbSrSe. With 10% Eu or Sr contents the fundamental absorption edges of these alloys are ≈ 450 meV (2.2 μm). However, for both ternary systems the FWHM of the x-ray diffraction rocking curve increases while the carrier mobility decreases with increasing Eu or Sr contents. IV-VI lasers with wavelengths shorter than 3 μm that are fabricated from these ternary systems, therefore, may be challenged by these physical restrictions. Of the two ternary systems PbSrSe may be better for laser fabrication due to the higher achievable carrier concentrations in *p*-type MBE-grown films.

Motivated by device integration with the mature silicon technology, Eu-based IV-VI semiconductors have also been grown on Si substrates. For example, photovoltaic infrared sensor arrays have been fabricated from PbEuSe/PbSe epilayers grown on (111)-oriented Si substrates by MBE [27]. IV-VI epitaxy on Si is enabled by growing a fluoride buffer layer between the Si substrate and the IV-VI layers. The large thermal expansion coefficient mismatch between the IV-VI layer and the Si substrate, however, contributes to an in-plane tensile strain in the IV-VI layer when the sample is cooled to room temperature after growth. This thermally induced strain is relieved mostly by plastic deformation (dislocation glide) along {100} planes in the $\langle 110 \rangle$ directions.

IV-VI on fluoride heteroepitaxy has also been motivated by the prospect of increasing the laser operating temperature using the recently developed new laser fabrication technology [16]. In this method the removal of the Si substrate by dissolving the water-soluble fluoride layer allows bonding of IV-VI epilayers between two copper heat sinks. Since copper is a much better heat conductor than the traditionally used PbSe or PbTe substrate materials Joule heating in the active layer can be dissipated more effectively at a higher heat sink temperature.

Diode lasers fabricated from IV-VI alloys, however, require high carrier concentration not easily attainable using the MBE growth method. The volatility of group VI elements and the difficulty in controlling the stoichiometry of alloy composition during MBE growth often results in the as-grown samples being weakly *n*- or *p*-type. Pb_{1-x}Eu_xSe layers with high carrier concentrations have recently been realized on CaF₂/Si (111) substrates [6]. High resolution x-ray diffraction (HRXRD) and electrical characterization of these alloys revealed good crystalline quality with carrier concentrations as high as 10¹⁸ cm⁻³. The results of preliminary FTIR studies of the absorption edge energies as a function of Eu content and temperature were also reported.

The precise knowledge of optical constants above and below the fundamental absorption edge is important for the design of IV-VI double heterostructure (DH) and multilayer quantum well lasers. This is particularly true at low-temperatures since all commercial IV-VI diode lasers still operate at cryogenic temperatures. Although several authors [7, 28, 29, 30] have investigated the refractive index of PbEuTe, there are few published reports on PbEuSe and PbSrSe alloys. This chapter concerns the growth procedure and FTIR characterization of $\text{Pb}_{1-x}\text{Eu}_x\text{Se}$ and $\text{Pb}_{1-x}\text{Sr}_x\text{Se}$ alloys. Analysis of the resultant transmission spectra leading to the determination of absorption edges and refractive indices will be presented.

3.2 Growth Procedure

Samples that are characterized by FTIR spectroscopy include the unintentionally doped p -PbEuSe on $\text{CaF}_2/p\text{-Si}(111)$ structures; and the intentionally doped p -PbEuSe on $\text{CaF}_2/p^+\text{-Si}(111)$ structures with varying dopant levels. Normally Se evaporates from grown layers during MBE growth resulting in group VI vacancies thus making the alloy n -type. The unintentionally doped p -type layers were grown with a selenium overpressure to compensate for the evaporation. With the growth surface under a Se rich condition group IV vacancies form and the alloy becomes p -type [31]. Adjusting the PbSe/Se flux ratios can vary the Se pressure over the growth surface. In this growth the Se overpressure was increased by an additional selenium flux provided by an EPI valved cracker effusion cell. These p -type layers shall hereinafter be referred to as the “undoped” layers to differentiate from those that are intentionally doped (hereinafter the “doped”) by the introduction of impurities.

The growth was carried out in an Intevac Modular GEN II MBE system. Silicon wafers with offcut angles less than 0.3° were outgassed in the buffer chamber at 200°C for one hour before loading into the growth chamber. They were subsequently primed using a reduced-temperature thermal cleaning procedure [32]. This procedure

minimizes chemical reactions between Se vapor and fluoride or silicon thus enhancing good CaF_2 epitaxy on Si. To prepare for CaF_2 growth high-purity bulk polycrystalline CaF_2 was heated in an effusion cell at high temperatures ($> 1260\text{ }^\circ\text{C}$). All CaF_2 layers were then grown on thermally cleaned $\text{Si}(111)$ at $700\text{ }^\circ\text{C}$ for a specific duration of time depending on the desired thickness.

PbSe growth was accomplished by heating bulk PbSe in a low-temperature ($650\text{--}700\text{ }^\circ\text{C}$) effusion cell. PbEuSe growth was accomplished by evaporating bulk PbSe and elemental Eu from low-temperature effusion cells. The europium content was controlled by adjusting Eu flux relative to the PbSe flux. Eu to PbSe flux ratios were 0, 1%, and 3% for the undoped samples (W202, W214, and W215, respectively) and 1% for the doped samples (W233, W234, and W235) in the growth experiments. The corresponding atomic concentrations of Eu in PbEuSe, estimated from the flux ratio using the empirical relation $[\text{Eu}](\text{x}) = 2.44 \times \text{Eu flux ratio}$ [26], are 2.44% and 7.32%.

Doping of PbEuSe layers was accomplished by evaporating Tl_2Se from fast dopant effusion cells. It has been shown [32] that there exists a monotonically increasing, linear relationship between the beam equivalent pressure and the carrier concentration. A higher Tl dopant level was obtained by holding the effusion cell at a higher temperature, which results in an increase in the equivalent beam pressure.

All PbSe and PbEuSe layers were grown at $280\text{ }^\circ\text{C}$ with the exception of a PbSe buffer layer in sample W202 that was grown at $310\text{ }^\circ\text{C}$. Growing a PbSe cap layer minimized surface oxidation of the PbEuSe layer. Initially the growth of PbSe and PbEuSe on $\text{CaF}_2/\text{Si}(111)$ proceeded in a three-dimensional mode as evidenced by the appearance of a spotty pattern by reflection high-energy electron diffraction (RHEED). However, the RHEED patterns gradually became streaky as the growth continued, indicating a smooth growth surface. The PbSe buffer layer was grown at a slightly higher temperature to enhance the transition from 3-D to 2-D growth. This buffer layer also serves to bridge the lattice mismatch between PbSe ($a_0 = 6.126\text{ \AA}$) and CaF_2 ($a_0 =$

5.463 Å). When viewed under a Nomarski optical microscope, the surface of the layers appears to be mirror smooth. The crosshatches running along the three $\langle 110 \rangle$ directions are likely due to dislocation glide leaving steps on the surface. This is evidence of the thermal mismatch strain relief mentioned earlier.

PbSe, Se, and Sr were used as source materials for the growth of PbSrSe. The growth procedure was similar to that of PbEuSe with an excess Se flux to make the film p -type. Three Sr flux ratios (3%, 6%, and 10%) were incorporated in the growth experiments. The corresponding atomic Sr content in PbSrSe, estimated using the relation $[\text{Sr}](\%) = 2.61 \times \text{Sr flux ratio}$ [26], are 7.83%, 15.7%, and 26.1%. A PbSe cap layer was also grown to prevent surface oxidation of the PbSrSe layer.

The epilayer structures of the samples and their average thicknesses are listed in Table 3.1. The thickness of the epilayers in each sample is measured using a Tencor step scan profiler. Several measurements are made on each sample and the average is taken. Since each measurement usually differs at the third decimal point, the variation of thickness per sample is less than 1%.

The carrier concentration was obtained from Hall mobility measurements. The undoped PbSe and PbEuSe layers typically have hole concentrations in the low 10^{17} cm^{-3} range. Table 3.2 shows the hole concentration (in cm^{-3}) in the PbEuSe epilayers of four samples, all of which were grown with 1% Eu flux ratio.

3.3 FTIR Spectroscopy Procedures

The transmission measurements were performed using a vacuum bench Bruker IFS 113 Fourier transform infrared spectrometer. The source radiation was generated by a graphite globar, which was resistively heated at 22 volts and 4 amperes from a Hewlett Packard 6263B DC power supply. The globar emits a broadband radiation in the mid-infrared range of approximately 100 cm^{-1} to 5000 cm^{-1} . The source radiation was directed to the interferometer chamber where it is modulated by a Genzel-type

Table 3.1 Listing of epilayers (the IV-VI layers plus the CaF₂ layer) on Si and BaF₂ substrates for ten different samples. The IV-VI layer of interest is indicated in boldface letters. The small print denotes the flux ratio of europium or strontium and the predicted thickness determined from the growth rate and the growth time. The thickness in the right column is the averaged measured thickness of the epilayers in a sample. Both the Si and the BaF₂ substrates are (111) oriented.

Sample #	Layer Description with Flux Ratio and Predicted Thickness	Measured Thickness (μm)
W202	PbSe /PbSe, 3000 Å/CaF ₂ , 20 Å/ <i>p</i> -Si	4.175
W214	PbSe, 1500 Å/ PbEuSe , 1%, 2.2 μm /CaF ₂ , 50 Å/ <i>p</i> -Si	2.556
W215	PbSe, 1500 Å/ PbEuSe , 3%, 2.2 μm /CaF ₂ , 50 Å/ <i>p</i> -Si	2.517
W233	PbSe, 1614 Å/ PbEuSe , 1%, 2.421 μm /CaF ₂ , 455 Å/ <i>p</i> ⁺ -Si	2.39
W234	PbSe, 1614 Å/ PbEuSe , 1%, 2.421 μm /CaF ₂ , 579 Å/ <i>p</i> ⁺ -Si	2.39
W235	PbSe, 1614 Å/ PbEuSe , 1%, 2.421 μm /PbSe, 1614 Å/ CaF ₂ , 313 Å/ <i>p</i> ⁺ -Si	2.39
B17	PbSe /BaF ₂	2.29*
B14	PbSe, 100 Å/ PbSrSe /BaF ₂	3.32*
B15	PbSe, 100 Å/ PbSrSe /BaF ₂	3.43*
B16	PbSe, 100 Å/ PbSrSe /BaF ₂	3.81*

* with 0.04 μm uncertainty

Table 3.2 Hole concentrations of four *p*-type PbEuSe sample layers.

Sample #	Hole concentrations (cm^{-3})	
	77 K	300 K
W214	1.24×10^{17}	1.65×10^{17}
W233	3.37×10^{17}	4.98×10^{17}
W234	1.19×10^{18}	1.03×10^{18}
W235	3.5×10^{18}	2.79×10^{18}

interferometer equipped with a germanium-coated potassium bromide (KBr) beamsplitter. The beamsplitter allows transmission of radiation in the 400-4000 cm^{-1} spectral range.

The modulated radiation emerging from the interferometer chamber enters one of the two sample chambers through an intermediate chamber that houses switching and collimating mirrors. The front sample chamber contains a custom-made cryostat and sample holder assembly while the back sample chamber is usually kept empty. The sample and the background blackbody spectra can be measured by directing radiation to the front and the back chambers, respectively.

To prepare for transmission measurements as-grown samples approximately 10 mm by 10 mm in surface dimension were gently pressed against the opening of the sample holder. The sample holder is made out of copper and is attached to the lower portion of the cryostat by an adjustable screw. The sample holder can rotate 360° and its opening is coaxial with the port where the modulated radiation enters the sample chamber. All transmission spectra were obtained with the radiation normal to the sample holder and incident upon the unpolished backside of the Si wafer. The upper portion of the cryostat rises above the sample chamber portion of the optical bench, permitting its filling with liquid nitrogen. Samples were cooled after the optical bench was vacuumed to ~15 mBar. A silicon temperature sensor mounted next to the sample on the sample holder monitored the sample heat sink temperature via a LakeShore 330 Autotuning temperature controller.

The transmitted radiation was directed to a photoconductive, liquid nitrogen cooled mercury cadmium telluride (MCT) detector. The detector signal (the interferogram) was displayed on a Hewlett Packard 54600B oscilloscope. The nominal detection range is from 600 cm^{-1} (17 μm) to 5,000 cm^{-1} (2 μm) with peak detectivity at 700 cm^{-1} (14 μm). The detector cuts off completely at ~420 cm^{-1} at which nearly total absorption is seen on the measured spectra.

There was usually a 30-minute wait prior to the data collection, which allows the optical system to reach thermal stabilization. Since the scanning mirror was air cushion driven the optical bench was continuously kept under vacuum during data collection. To change the sample, the optical bench was vented and then re-vacuumed. The optical bench was normally vented with compressed air supplied in the laboratory.

A software controlled instrument calibration procedure was observed prior to the commencement of each data collection. When the proper parameters for scan control were secured the interferogram was displayed on the spectrometer's computer screen. The interferogram was also monitored on an oscilloscope during measurements. A typical spectral measurement involved data collection and averaging over one hundred scans.

Dividing the transmission obtained from the sample and that from a separate piece of a substrate having the same thickness as the substrate used in the sample normalizes the transmission spectrum of interest. Ratioing the two transmissions over a common frequency range cancels out the effect of blackbody spectral background, the reflection at the substrate-to-air interface, and the absorption within the substrate. It also cancels out the instrumental effects associated with the bandpass functions of the filters and the detector.

3.4 Experimental Results for PbSe

The FTIR transmission measurements were performed on the samples described in section 3.2 in the mid-infrared region of $400\text{--}5000\text{ cm}^{-1}$. The substrate spectrum used to normalize the spectrum of PbSe/CaF₂/Si was obtained from a bare Si wafer. The transmission range of Si and CaF₂ is $1500\text{--}8300\text{ cm}^{-1}$ and $1400\text{--}52,600\text{ cm}^{-1}$ [33], respectively, with comparable infrared limits. Since Si has an index of refraction about 2.5 times larger than that of CaF₂ in its transmission range, it is unlikely that multiple reflections can occur in the CaF₂ layer. Since the CaF₂ layer is very thin ($\leq 0.005\text{ }\mu\text{m}$),

infrared absorption by CaF_2 is negligible. Thus the Si wafer is a convenient source for obtaining the substrate spectrum. Figure 3.1 shows the normalized transmission spectra

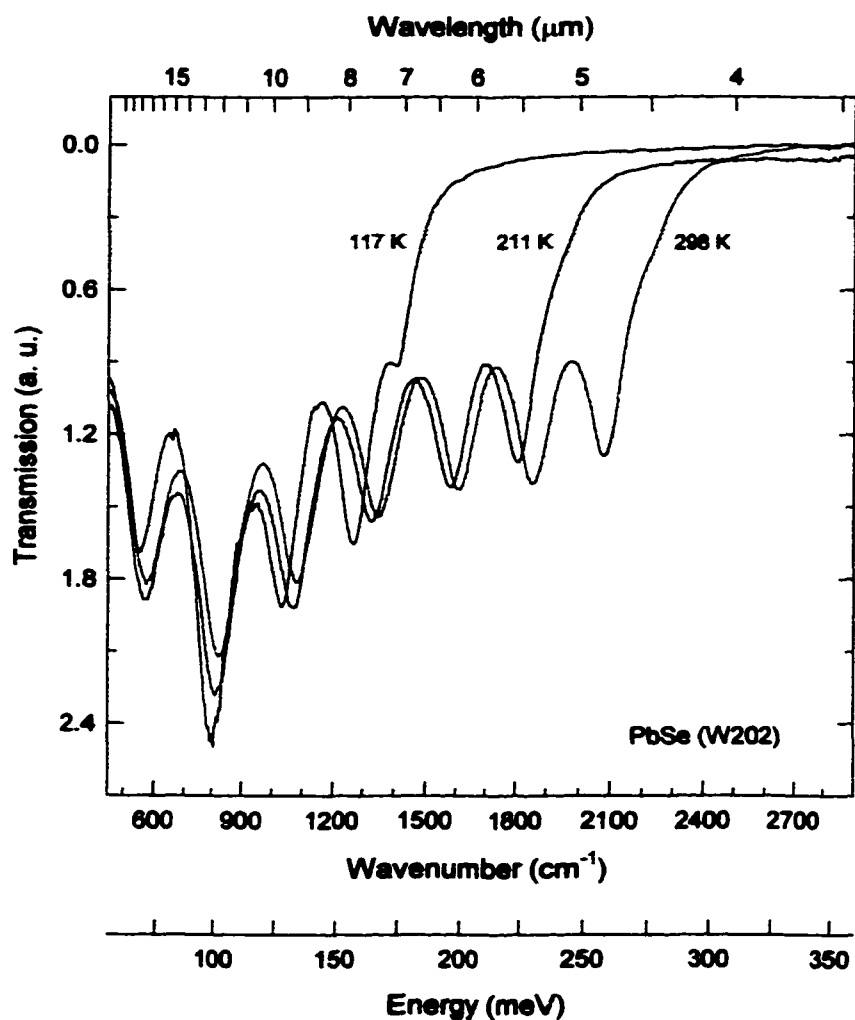


Figure 3.1 FTIR transmission spectra of PbSe at three temperatures.

of the main PbSe layer in sample W202 measured at three temperatures. The sharp absorption edge is characteristic of the direct bandgap of IV-VI semiconductors. The shift of the fundamental absorption edge toward lower energy as temperature decreases

is also characteristic of the IV-VI material whose bandgap energy is known to exhibit positive temperature dependence. The presence of the Fabry-Perot interference fringes reflects the smooth morphology of the PbSe layers. The fringes are due to multiple internal reflections in PbSe, which is known to have larger index of refraction than either Si or CaF₂ (3.4 and 1.4, respectively, in their transparent regions).

A direct gap semiconductor is expected to be transparent at all photon energies below the bandgap. However, an increased in absorption at energies from ~1000 cm⁻¹ to the absorption edge is observed for the PbSe sample. The reason for this peculiar “absorption shoulder” is not clear at the present time. Care should be taken when interpreting the transmission spectrum at the spectral region below 500 cm⁻¹, which is near the detector cutoff.

The transmission spectrum of PbSe (Figure 3.1) also gives information about its absorption edge energies. The absorption edge cannot be obtained using the conventional method of taking the sharp-rising edge to the “zero intercept” because transmission is not uniformly flat over the energies below the edge. Using the intercept of two lines, one from the edge and a second formed by the transmission maxima, absorption edges of PbSe at 2100 cm⁻¹, 1820 cm⁻¹, and 1340 cm⁻¹ corresponding to the three measurement temperatures were obtained. These values are plotted as a function of the sample heat sink temperature, shown in Figure 3.2. Also plotted are data points at three different temperatures from the Zemel et al. [34] in which the fundamental absorption edge is derived from the peak of the plot of index of refraction. These data points, while obtained from a completely different method show little scatter from the linear fit to the data points in the present study. Also shown in Figure 3.2 are plots generated from the analytical form described by Strauss [35] based on optical transmission method and Preier [36] based on optical absorption and laser emission methods.

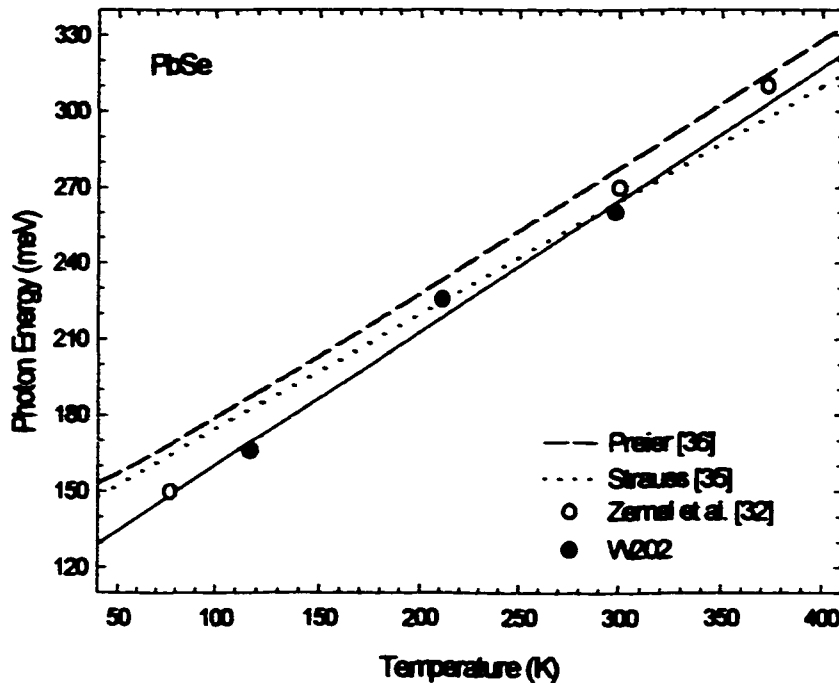


Figure 3.2 Fundamental absorption edge energies versus temperature plot. The solid line (slope ≈ 0.5 meV/K) is the linear fit to the data of W202.

3.5 Experimental Results for PbEuSe

Transmission spectra of PbEuSe/CaF₂/Si with atomic Eu content of 2.44% and 7.32% (samples W214 and W215) were measured at room temperature and at low temperature. Normalized by the same substrate spectra used for PbSe, the spectra of PbEuSe together with those of PbSe are shown in Figure 3.3. Apparent from these spectra is the shift of the fundamental absorption edge toward higher energy as the Eu content increases. Again, the presence of Fabry-Perot interference fringes indicates the good quality of the PbEuSe epitaxial layers.

A separate set of spectra at room temperature is presented in Figure 3.4. The “absorption shoulder” observed in PbSe’s transmission spectra is not seen for the two PbEuSe layers. Rather, there is almost uniformly reduced transmission at energies below the absorption edge. The width of the fringe for the two PbEuSe samples is

comparable due to similar layer thickness (2.401 μm and 2.362 μm , respectively). The fringe spacing of the PbSe sample is much closer because it is a thicker layer (3.873 μm). The optical finesse (i.e., the sharpness of the fringe), however, appears to be poorer for the PbEuSe sample having a higher Eu concentration.

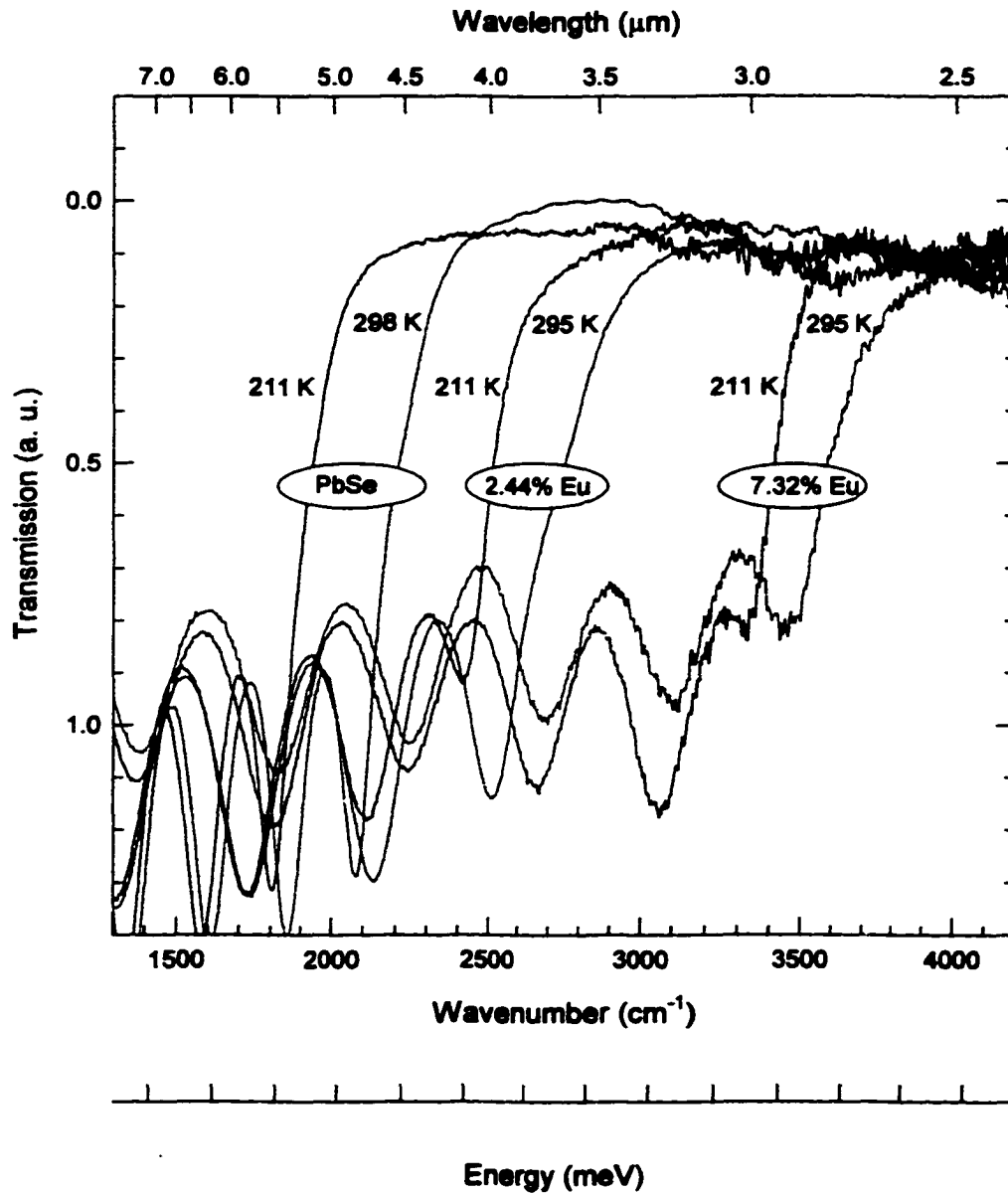


Figure 3.3 FTIR transmission spectra of $\text{Pb}_{1-x}\text{Eu}_x\text{Se}$ layers on Si(111) at room and low temperatures.

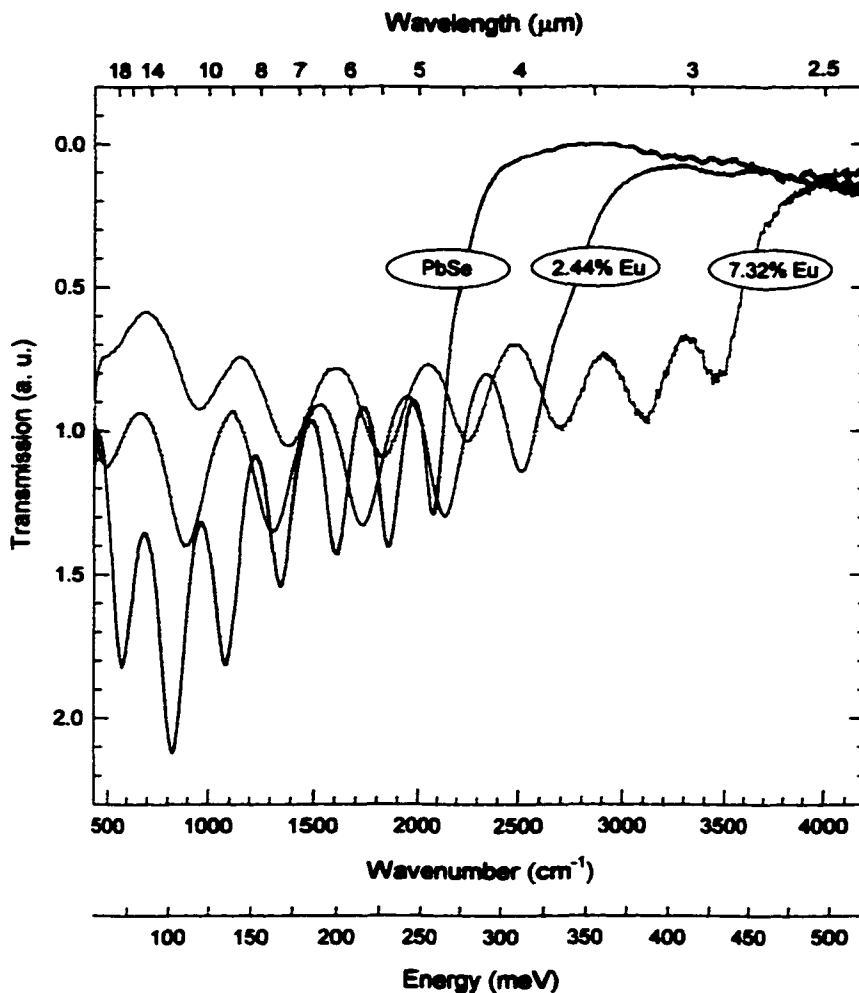


Figure 3.4 FTIR transmission spectra of $Pb_{1-x}Eu_xSe$ layers on Si (111) at room temperature.

The absorption edge energy as a function of the Eu content is plotted at two temperatures, see Figure 3.5. The absorption edge energy increases with the Eu content as expected and there appears to be a linear relationship with a slope $dE/dx = \sim 24$ meV, per atomic % Eu. This value is within fair agreement with that reported by Lambrecht et al. [26] who also obtained a linear relations with $dE/dx = \sim 28$ m eV per % Eu at 300 K. From Figure 3.5 one observes a weaker temperature dependence of the absorption

edge with increasing Eu content. This trend has also been reported by Herrmann et al. [37] based on their PbEuSe samples.

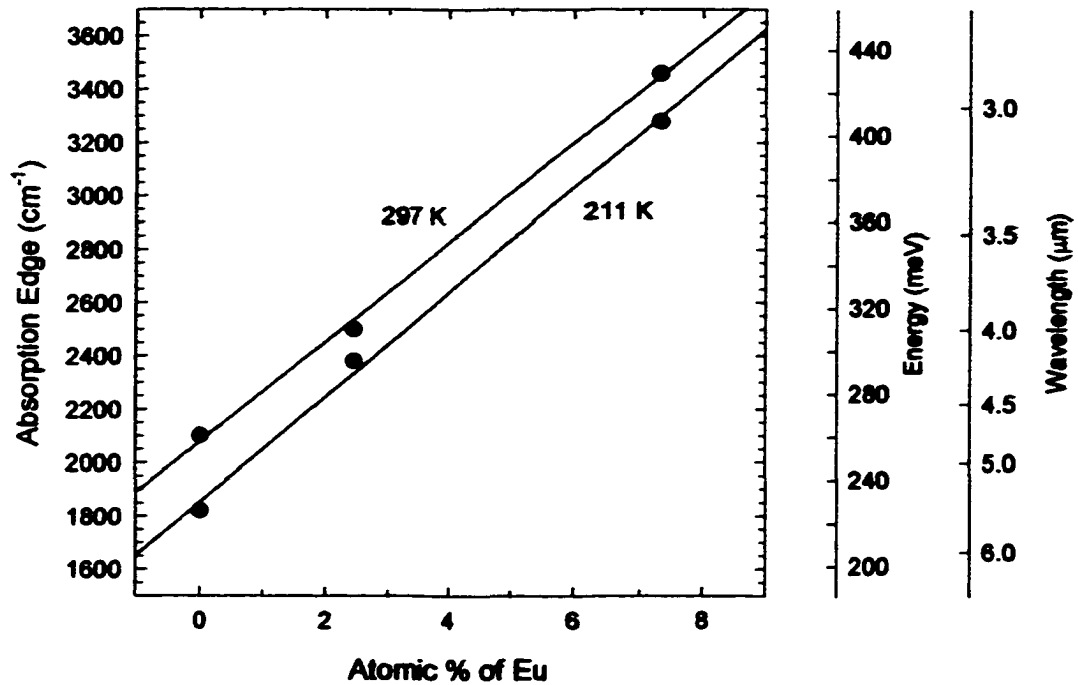


Figure 3.5 Absorption edge energy as a function of europium content in $\text{Pb}_{1-x}\text{Eu}_x\text{Se}$ ($x = 0\%$, 2.44% , 7.32%) at two temperatures. The solid lines are first-order linear regression fits.

Normalized transmission spectra of the thallium doped PbEuSe samples (W233, W234, and W235), measured at room temperature, are shown in Figure 3.6. The substrate spectrum was obtained from a $\text{CaF}_2/p^+\text{-Si}(111)$ substrate. The spectrum of the undoped PbEuSe sample, which also has a 2.44% Eu content is included for comparison. The thickness of the IV-VI layers in the doped samples is comparable: $2.34 \mu\text{m}$ for W233, $2.33 \mu\text{m}$ for W234, and $2.36 \mu\text{m}$ for W235. Compared to the undoped PbEuSe the doped layers show a marked increase of absorption at energies below the absorption edge.

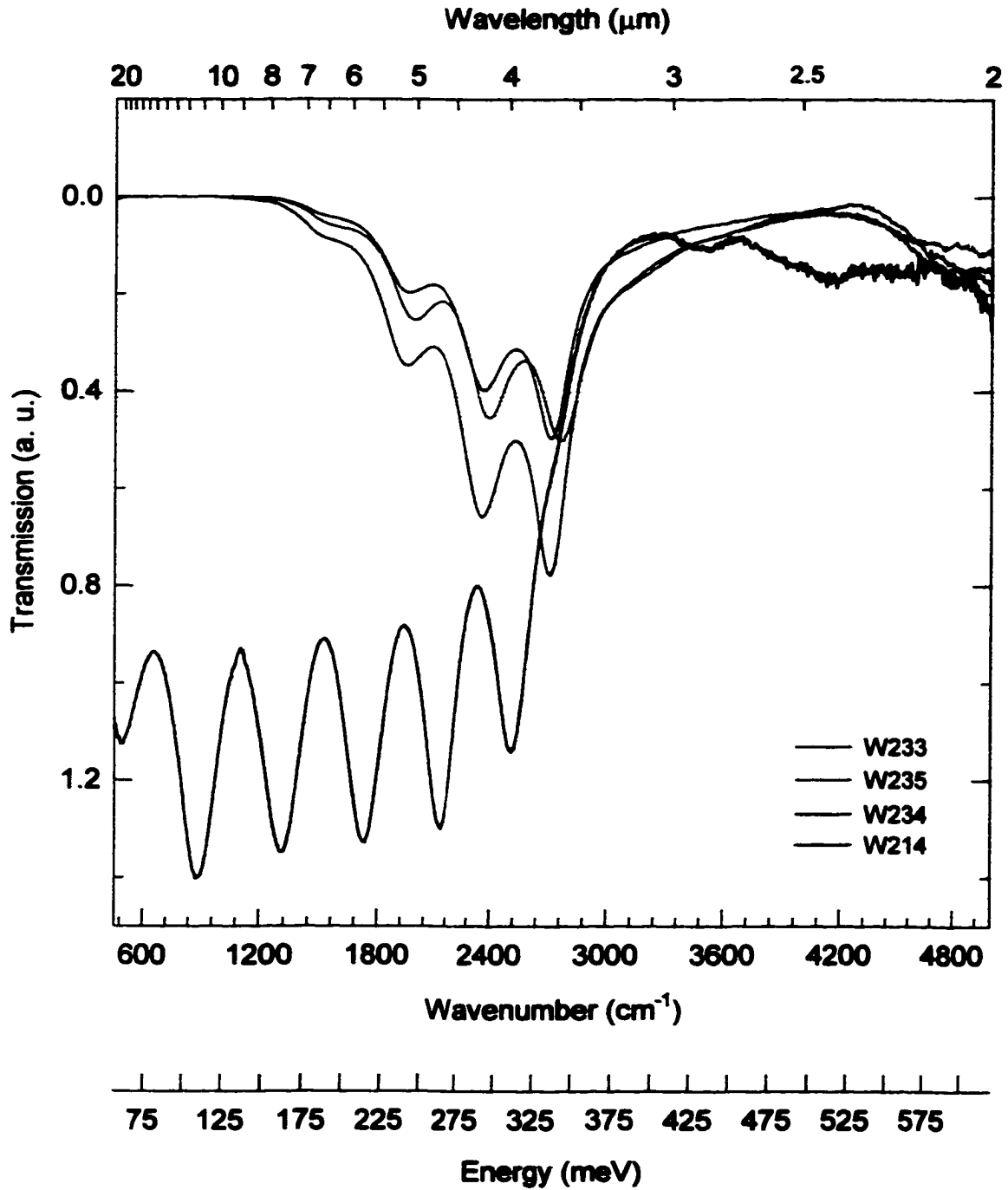


Figure 3.6 FTIR transmission spectra of *p*-PbEuSe epilayers with different carrier concentrations. The top spectra are obtained from thallium doped samples (from top: W233, W235, W234). The bottom spectrum is from the undoped sample (W214). All samples shown here have 2.44% Eu content.

3.6 Experimental Results for PbSrSe

Room temperature transmission spectra of MBE-grown $\text{Pb}_{1-x}\text{Sr}_x\text{Se}$ layers on $\text{BaF}_2(111)$ ($x = 0, 7.83\%, 15.7\%$, and 26.1% , corresponding to samples B17, B14, B15, and B16) were measured using a different FTIR spectrometer (BioRad model FTS-60A). The spectrometer is equipped with a MCT detector with a cutoff wavelength of $\sim 700 \text{ cm}^{-1}$ ($14.3 \mu\text{m}$).

The normalized transmission spectra for four different $\text{Pb}_{1-x}\text{Sr}_x\text{Se}$ samples are shown in Figure 3.7. The fundamental absorption edge energy of PbSe is comparable to that of PbSe grown on Si(111) substrate. Like $\text{Pb}_{1-x}\text{Eu}_x\text{Se}$ alloys the absorption edge energy increased with increasing Sr contents. Unlike $\text{Pb}_{1-x}\text{Eu}_x\text{Se}$ these alloys are fairly uniformly transparent over broad energies below the absorption edge.

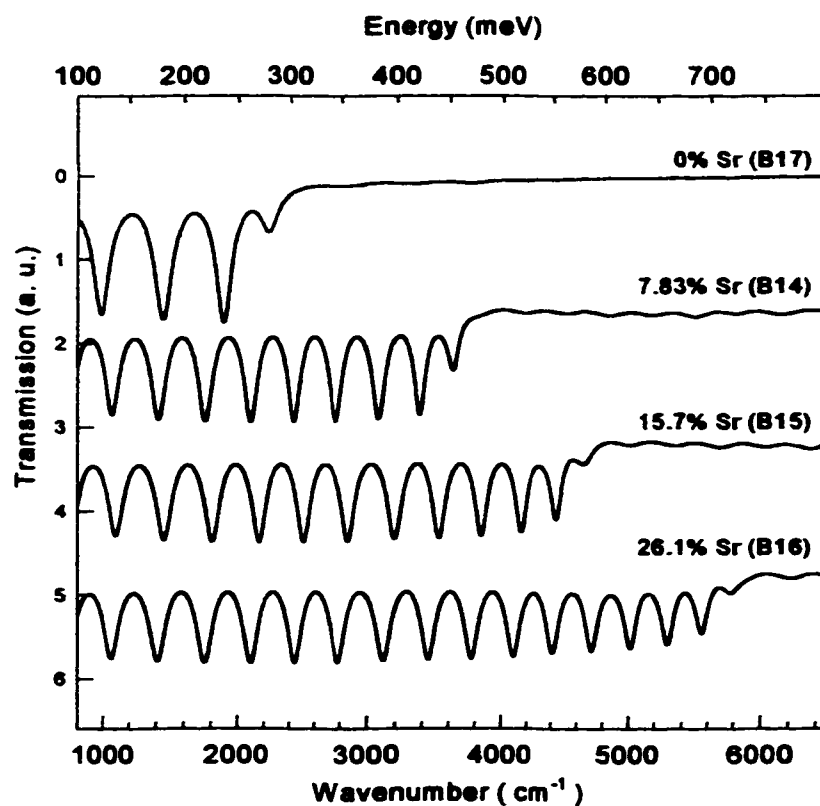


Figure 3.7 Room temperature transmission spectra for $\text{Pb}_{1-x}\text{Sr}_x\text{Se}$ alloys grown on $\text{BaF}_2(111)$ substrates.

The shifting of the fundamental absorption edge toward higher energy with increasing Sr content is demonstrated in Figure 3.8. The absorption edge energy is

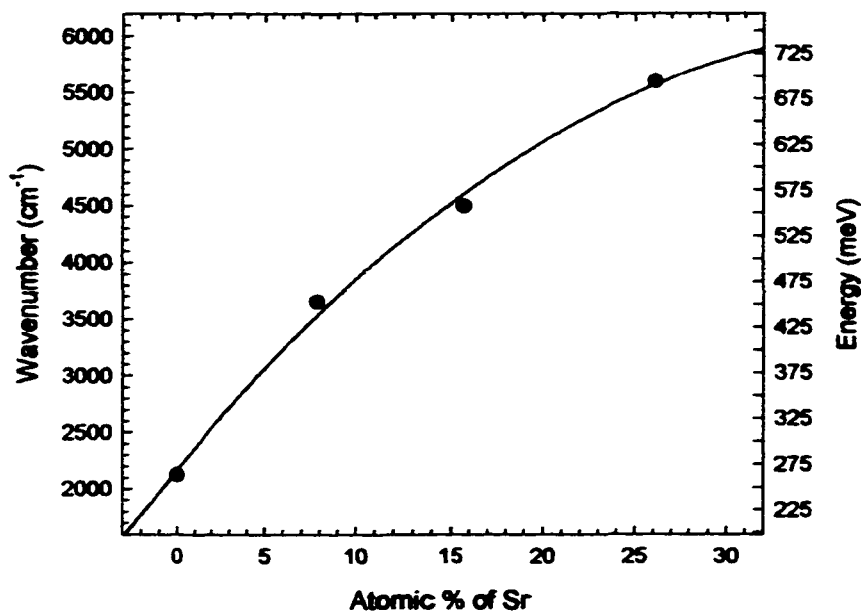


Figure 3.8 The fundamental absorption edge as a function of Sr content for $\text{Pb}_{1-x}\text{Sr}_x\text{Se}$ layers on BaF_2 (111).

taken as the intercept of the edge with a horizontal line drawn across the mid-point of the fringes. The variation of the absorption edge of PbSrSe as a function of Sr content shows a parabolic fit, contrary to the linear fit for PbEuSe . These trends agree well with those obtained by Lambrecht et al. [26] but the energy values for PbSrSe are again consistently lower than those of Lambrecht et al. The initial slope of dE/dx is 24 meV per % Sr compared to their value of 37 meV. The absorption edge of PbSe at room temperature is 260 meV compared to their value of 280 meV although their data is said to have an uncertainty of 20 meV. The absorption edges of PbSrSe differ significantly between the two works. For example, an 8% Sr sample had values of 437 meV and 520 meV [26] in the two different methods. The discrepancy (for both PbEuSe and

PbSrSe) may be attributed to the method of estimating the atomic Eu or Sr contents in the present work. An x-ray diffraction study is currently being conducted, which should yield more accurate values for the actual compositions.

The optical constants of thin films may be experimentally determined using a combination of absorptance, reflectance, and transmittance measurements. A widely used method that determines the refractive index of a single-layer thin film based on the interference of measured FTIR transmission spectra is described here.

For normal incidence of radiation upon a weakly absorbing layer ($k/n \ll 1$, where k is the extinction coefficient and n the refractive index of the layer), the transmittance can be expressed as [38]

$$T = \frac{(1 - \gamma_{12}^2)(1 - \gamma_{23}^2)\exp(-\alpha d)}{1 + 2\gamma_{12}\gamma_{23}\exp(-\alpha d)\cos(2\delta) + \gamma_{12}^2\gamma_{23}^2\exp(-2\alpha d)} \quad (3-1)$$

where

$$\gamma_{12} = \frac{n_1 - n_2}{n_1 + n_2}, \quad \gamma_{23} = \frac{n_2 - n_3}{n_2 + n_3}, \quad \delta = \frac{2\pi n_2 d}{\lambda}$$

The refractive indices of the air, the film (having a thickness of d and absorption coefficient of α), and the substrate (assuming transparency) are represented by n_1 , n_2 , and n_3 , respectively. For n_2 greater than n_1 and n_3 the cosine term in the denominator describes the interference arising from multiple reflections of light traveling in the film with a wavelength of λ . Designating n_2 as n and equating $2nd = m\lambda$, then $\cos(2\delta) = \cos(2\pi m)$. Thus the condition for the transmission maximum or the transmission minimum to occur in the film is when m is an integer (1, 2, 3, ...) or a half integer (1/2, 3/2, 5/2, ...), respectively. Rewriting $2n_m d = m\lambda_m$, where n_m is the refractive index of the light with a wavelength of λ_m at the m^{th} fringe order, it can be shown that

$$m = \frac{\beta \lambda_{m+1}}{\lambda_m - \beta \lambda_{m+1}} \quad (3-2)$$

Assume that n does not change appreciably from λ_m to λ_{m+1} (i.e., $\beta \equiv n_m/n_{m+1} \approx 1$), then

$$m \approx \frac{\lambda_{m+1}}{\lambda_m - \lambda_{m+1}} = \frac{v_m}{v_{m+1} - v_m} \quad (3-3)$$

where $v=1/\lambda$. And the refractive index at the m^{th} fringe order is

$$n_m = \frac{m}{2dv} \quad (3-4)$$

Once the fringe order is determined from the transmission spectrum according to equation (3-3) the refractive index can be calculated using equation (3-4).

BaF₂ is transparent from visible region to $\sim 11\mu\text{m}$ ($\sim 900\text{ cm}^{-1}$) and has a refractive index value of ~ 1.4 [33] in its transparent region. Therefore, the refractive indices of Pb_{1-x}Sr_xSe grown on BaF₂ substrates can be calculated based on the transmission spectra shown in Figure 3.7 and using the method discussed above. Here we neglect the very thin PbSe cap layers for samples B14, B15, and B16 (if interference does occur in the cap layer the fringes will be widely separated). The film thicknesses used for the calculation are the values listed in Table 3.1 and m and n values calculated are based on transmission maxima. The refractive index of Pb_{1-x}Sr_xSe as a function of photon energy below the fundamental absorption edge is plotted in Figure 3.9. It can be seen that increasing Sr content has the same effect of decreasing the refractive index as increasing the Eu contents in Pb_{1-x}Eu_xTe alloys [30] whose refractive indices were

calculated using the same method. These plots reflect a rather homogeneous trend as functions of both photon energy and alloy composition.

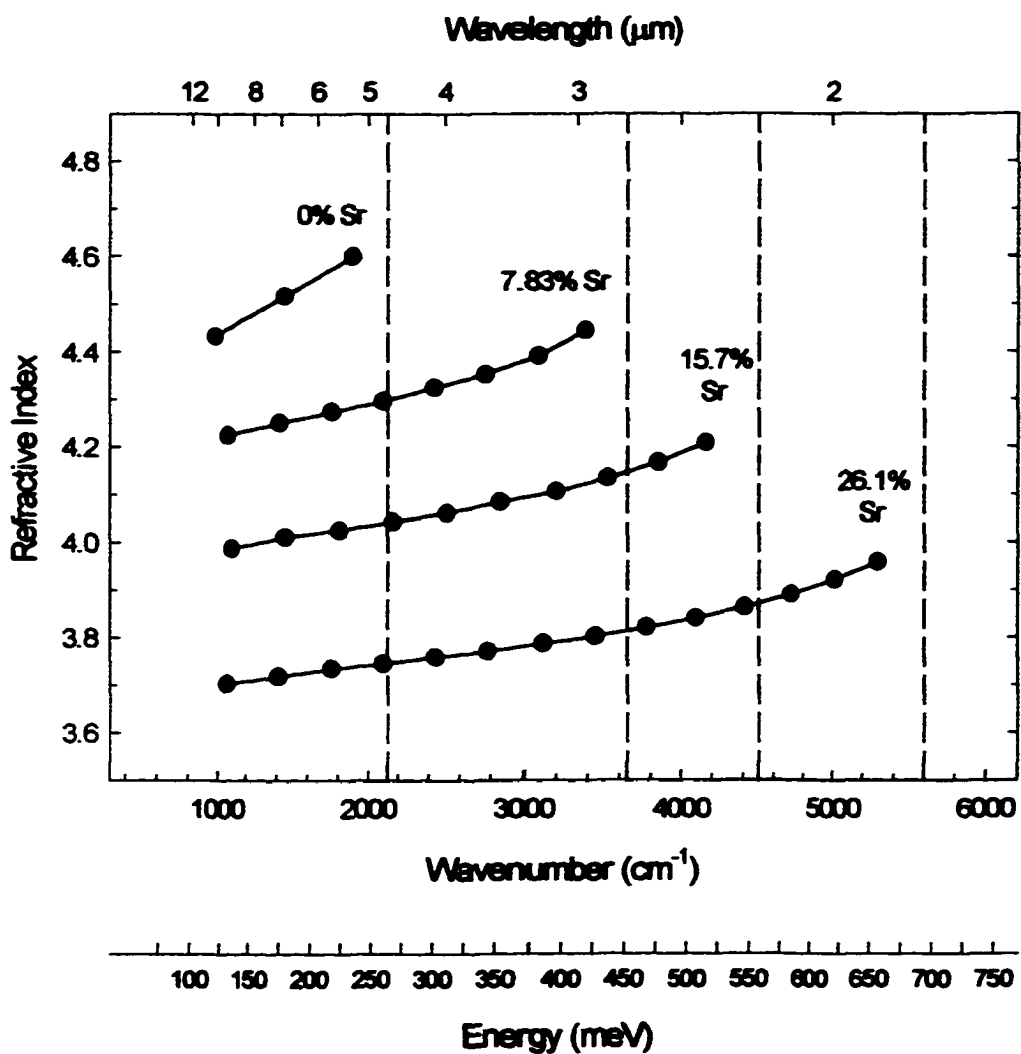


Figure 3.9 Room temperature refractive index plots of Pb_{1-x}Sr_xSe (x = 0%, 7.83%, 15.7%, 26.1%) layers on BaF₂ (111). The intercepts of the dashed lines with the wavenumber axis are the absorption edge energies for each alloy.

The refractive index at the absorption edge for each alloy can be estimated by extrapolating the line connecting the data points to the dashed line for each plot. The estimated refractive index values are listed in Table 3.3.

Table 3.3 Calculated room temperature refractive index for $\text{Pb}_{1-x}\text{Sr}_x\text{Se}$.

Sample #	n	λ
B17, [Sr]=0%	4.7	4.71 μm
B14, [Sr]=7.83	4.5	2.74 μm
B15, [Sr]= 15.7	4.3	2.22 μm
B16, [Sr]= 26.1	4.1	1.79 μm

3.7 Discussion and Summary

The transmission spectra of PbEuSe (see Figure 34) show an increased absorption over a broad photon energy range below the fundamental absorption edge. The same observation has been made on $\text{Pb}_{1-x}\text{Eu}_x\text{Te}$ samples for $x > 0.02$ [28] and on other $\text{Pb}_{1-x}\text{Eu}_x\text{Se}$ samples [37]. Those authors have attributed this enhanced absorption to alloy composition fluctuations. The compositional fluctuations may also be responsible for the poorer optical finesse seen on the spectrum of PbEuSe with the highest Eu content. The enhanced absorption is also observed for PbSrSe (Figure 3.7) but it only becomes more significant for $x > 0.1$. It has been suggested [29] that the enhanced absorption can also be attributed to the interaction of band states between the localized $4f^7$ Eu atomic states and the $5p^6$ valence band states. Since the strontium atom does not have an unfilled inner shell like europium, this aspect cannot be held accountable for what is observed for PbSrSe . It, however, may be a possible explanation for the increased absorption with higher Eu content in the longer wavelength region.

Several mechanisms may be accountable for the strong absorption of the thallium-doped samples at energies below and above the absorption edge (see Figure 3.6). In a semiconductor with a large enough carrier concentration there can be metallic conduction where absorption by the carriers is of the same order of magnitude as the fundamental absorption [39]. This may be the reason why the doped PbEuSe samples show such strong absorption in the long wavelength region. The absorption in the intermediate frequency range may be due to transitions involving states such as thallium acceptor levels inside the bandgap. The effect of impurity and free carrier absorption in doped PbEuSe samples merit some consideration when designing photonic devices. The absorption features above the bandgap energy also differ between the doped samples and the undoped sample. Self-compensation is known to occur in thallium doped IV-VI semiconductors. There can exist defect states deep inside the conduction band much like the predicted vacancy states [40] in *n*-type samples. Further studies need to be conducted in order to evaluate the origin for the strong absorption feature above the absorption edge.

The dispersion of infrared radiation in a material is dependent on a multitude of variables such as band structure, alloy composition, carrier concentration, sample temperature, and state of system (i.e., equilibrium vs. non-equilibrium). By far there is no all-inclusive, systematic method for determining the refractive index of an alloy. The theoretical determination of refractive index for PbSe has been carried out using quantum mechanical oscillator models and first principle considerations [41]. These include the contribution from interband absorption near the bandgap energy and at higher photon energies, the contribution from free carrier absorption, and the contribution from phonon absorption. The refractive index for PbSe has been determined experimentally [34, 42] and semi-empirically [43, 44]. The comparison has been made [45] for the refractive index of PbSe between the theoretical calculation and the experimental data from Zemel et al. [34] and Opyd [43]. The agreement is quite

good, especially at room temperature, despite a lower carrier concentration ($3 \times 10^{17} \text{ cm}^{-3}$) assumed in the theoretical work. The published values of refractive index for PbSe are 4.6 to 4.9 in the near- to mid-infrared spectral region [34, 44, 46]. The refractive index value of 4.7 for PbSe (sample #17) in Table 3.3 is in fair agreement with these data. Therefore, calculation of refractive index based on interference of light transmission through a thin film is a simple and useful method for the calculation of refractive index of the layer.

Equation (3-1) is not adequate to describe light transmission through sample structures which consist of several thin layers such as those grown Si substrates (see Table 3.1). A further complication arises when one considers multiple reflections inside Si substrate whose refractive index is greater than the two neighboring media. A comprehensive treatment for calculating optical constants for multiple-layer structures is beyond the scope of this study but can be found in Macleod's text [47].

As stated by Zemel et al. [34], strain effects due to the difference in thermal expansion coefficients of the film and the substrate play an important role on the optical behavior near the absorption edge. The plastic deformation in PbEuSe epilayers due to the large mismatch of thermal expansion coefficients between the alloys and Si substrates may need further study in evaluating its role on the optical properties of these layers.

In summary, this study showed that the incorporation of europium and strontium into the IV-VI semiconductors has the effect of increasing the bandgap energies. The refractive index of PbSrSe decreases with increasing Sr contents. These are desirable material properties for designing double heterostructures that can achieve both electrical and optical confinement in the active layer. The PbSrSe alloys appear to have certain advantages over the PbEuSe alloys. PbSrSe has been favored as a photonic material due to higher achievable carrier concentration [26]. The initial rate of increase of absorption edge with composition for PbSrSe is appreciably larger than that for

PbEuSe, which is also observed by other authors [26]. It has been shown that PbSrSe/PbSe/PbSrSe DH lasers achieved higher operating temperatures than PbEuSe/PbSe/PbEuSe DH lasers [25]. This may be due to better optical and electrical confinement in the active PbSe layer. In terms of crystal quality, PbSrSe exhibits a smaller degree of alloy disorder than PbEuSe. This feature has been confirmed by other reports [29, 37] based on the two ternaries grown on same substrate materials. The effect of alloy disorder, free carrier absorption, impurity absorption, and substrate compatibility on the optical and electrical properties of thin films merit further study.

CHAPTER 4

Transmission Studies of Epilayers Grown by Liquid Phase Epitaxy

4.1 Introduction

The development of IV-VI semiconductor mid-infrared diode lasers has been motivated by their application in high-resolution molecular spectroscopy. Commercially available but costly PbSe and PbSnSe lasers are grown on costly PbSe or PbTe substrates. Motivated by the economy of silicon wafers and device integration with mature silicon technology, $\text{Pb}_{1-x}\text{Sn}_x\text{Se}$ semiconductor materials have been grown on Si (111) substrates using group IIa fluoride insulators as buffer layers [48, 49]. The growth of IV-VI materials on Si has allowed fabrication of monolithic infrared detector arrays in which infrared detection is performed in the IV-VI semiconductor layer and signal processing can be performed in the Si wafer.

The conventional PbSe bulk substrate, being a very poor thermal conductor, restricts the laser operating temperature to within the cryogenic temperature range. Motivated by the prospect of increasing laser operating temperature [16], $\text{Pb}_{1-x}\text{Sn}_x\text{Se}$ alloys have recently been grown on Si (100) using an innovative hybrid technique [5]. The Si substrates can be removed through selective etching of a MBE-grown BaF_2 buffer layer [50]. The freeing of IV-VI epitaxial layers from Si allows the formation of in-plane {100} faceted Fabry-Perot laser cavities without the hindrance of Si that cleaves preferentially in the $\langle 111 \rangle$ directions. IV-VI lasers fabricated using a minimum of thermally resistive IV-VI materials should have continuous wave operating temperatures greater than 260 K, within the range of thermoelectric cooling modules.

IV-VI on Si growth technology, however, suffers an inherent thermal expansion coefficient mismatch between IV-VI semiconductors and Si. This mismatch causes an in-plane tensile strain in the IV-VI films when cooled down following growth. In a totally elastic material, this strain can be calculated from $\Delta\alpha\Delta T$, where $\Delta\alpha$ is the difference in thermal expansion coefficient between the layer and the substrate, and ΔT is the difference between growth and room temperature. Because of this tensile strain MBE-grown PbSe layers on cooling down from a 280°C growth temperature develop high crack densities [51]. Surprisingly, PbSe layers obtained by liquid phase epitaxy (LPE) growth on those MBE-grown structures are crack free [52]. This is peculiar considering the fact that LPE growth temperatures are almost 200°C higher than MBE growth temperatures, thus subjecting the LPE grown layers to greater thermal strain.

LPE-grown $\text{Pb}_{1-x}\text{Sn}_x\text{Se}$ ($x = 0\%$, 3%, 5%, 7%, 9%, 10%, and 15%) layers on MBE prepared substrates have been studied using Nomarski microscopy, high resolution x-ray diffraction (HRXRD), and Fourier transform infrared (FTIR) spectroscopy [5]. These layers show excellent surface morphologies and good growth solution wipeoffs. Although most PbSe layers were free of cracks over an $8\times 8\text{ mm}^2$ area, PbSnSe layers exhibited varying crack densities ranging from zero in the center of films to over 30 cracks/cm at the periphery. IV-VI layers would sustain an in-plane tensile strain of 0.74% if no plastic deformation were present. HRXRD measurements of crack-free PbSe layers revealed a lattice parameter normal to the substrate of 6.122 Å. (The unstrained lattice parameter is 6.126 Å). These data along with known elastic constants [53] indicate a residual in-plane tensile strain of only 0.21% suggesting that most of the thermal expansion mismatch strain in PbSe is absorbed by plastic deformation.

The essential findings of the FTIR experiments performed in this study have been reported in reference 4. An in-depth analysis of the FTIR data, together with

pertinent discussions as they are related to the results of other characterization methods, will be presented in this chapter.

4.2 Growth Procedure

PbSe and $\text{Pb}_{1-x}\text{Sn}_x\text{Se}$ layers were grown by LPE from Pb-rich $(\text{Pb}_{1-x}\text{Sn}_x)_{1-z}\text{Se}_z$ liquid solutions on $\text{PbSe}/\text{BaF}_2/\text{CaF}_2/\text{Si}(100)$ structures prepared by MBE. The LPE layers were grown in a home-made LPE growth apparatus comprised of a graphite boat enclosed in a transparent quartz tube surrounded by a heater coil. Detailed description of LPE growth procedure have been presented elsewhere [5, 52]. The LPE growth solutions were prepared by combining weighed amounts of Pb, PbSe, and Sn according to relations derived from the molecular weights of the respective constituents. Based on phase equilibria data [54] the selenium concentration, z , was chosen to be 0.25 atomic % corresponding to a nucleation temperature of about 470°C for growth of a $\text{Pb}_{0.95}\text{Sn}_{0.05}\text{Se}$ layer.

The MBE-grown buffer layer structure was grown on a (100)-oriented, 3-inch diameter, p -type silicon wafer using an Intevac Gen II MBE system. The MBE growth was accomplished by first growing a thin CaF_2 layer at 580°C on the thermally cleaned silicon wafer, followed by growth of a BaF_2 layer. The final MBE layer was a PbSe layer grown at 280°C. The structures of three similar MBE substrates are listed in Table 4.1. For W113 a 3200 Å thick BaF_2 layer was grown at 580°C and annealed at 800°C for 3 minutes, followed by the growth of an additional 1500 Å at 700°C. For W245 a 2000 Å thick BaF_2 layer was grown at 580°C and annealed at 900°C for 3 minutes, followed by the growth of an additional 7000 Å at 700°C. The MBE structure was then cleaved along {111} planes into $1 \times 1 \text{ cm}^2$ sized substrates with edges parallel to the $\langle 110 \rangle$ directions.

Table 4.1 Structure of the MBE-grown substrates used for the growth of LPE layers.

Sample	Layer Structure
W113	PbSe, 1000 Å/BaF ₂ , 4700 Å/CaF ₂ , 200 Å/ <i>p</i> -Si(100)
W222	PbSe, 2.2 μm/BaF ₂ , 4700 Å/CaF ₂ , 400 Å/ <i>p</i> -Si(100)
W245	PbSe, 8100 Å/BaF ₂ , 9000 Å/CaF ₂ , 570 Å/ <i>p</i> -Si(100)

Tin concentrations, x_s , in the liquid growth solutions were chosen to be 0%, 3%, 5%, 6%, 7%, 9%, and 10%. The LPE grown samples corresponding to these compositions are listed in Table 4.2. Also listed in the Table are the thicknesses of the LPE layers measured using a Tencor step scan profiler.

Table 4.2 LPE layer composition and thickness and MBE substrates used for growing the LPE layers.

Sample	Tin, x_s (%)	MBE Substrates	PbSnSe Thickness (μm)
H9	0	W113	2.22
H13	3	W222	4.26
H12	5	W222	4.67
H15	6	W113	3.83
H14	7	W222	4.68
H17	10	W245	4.51

4.3 Results of FTIR Characterization

4.3.1 Optical Bandgap Energy

The FTIR measurements of the samples mentioned in the previous section were performed using a vacuum bench Bruker IFS 113 FTIR spectrometer equipped with a HgCdTe detector having peak detectivity at 14 μm . The experimental procedure has been described in Chapter 3 and will not be repeated here. The transmission spectra were normalized using the MBE grown structure $\text{BaF}_2/\text{CaF}_2/\text{Si}(100)$, in which the thicknesses of the BaF_2 and CaF_2 layers are 4000 \AA and 600 \AA , respectively. The normalized transmission spectra for samples H9-H17, measured at room temperature and at lower temperatures, are shown in Figures 4.1 to 4.6. Note that all spectra show below bandgap Fabry-Perot interference fringes as a result of multiple internal reflection within the IV-VI layers. The fringe spacing for sample H9 (Figure 4.1) is the largest because the LPE layer is the thinnest among all the samples. The fringe spacing for samples H12 (Figure 4.3) and H14 (Figure 4.5) is comparable because the thicknesses of the LPE layers in both structures are the same.

The absorption edge energy was read from a transmission spectrum as the intersection of two straight lines, one tangent to the transmission maxima below the absorption edge and the other tangent to the emerging absorption edge. From the transmission spectra (Figures 4.1 to 4.6) these values are plotted as a function of tin content in the liquid growth solution at the two measurement temperatures, see Figure 4.7. The absorption edge energies cover the 4.6 μm to 16 μm mid- to far-infrared spectral range for tin contents of 0%–10%, respectively. They are in good agreement with emission energies of PbSnSe lasers [55] fabricated from the vapor phase grown $\text{Pb}_{1-x}\text{Sn}_x\text{Se}$ alloys ($x = 6\%$ and 10%) and with the empirical expression $E_G(\text{meV}) = 130 - 890x + 0.45T$ derived from transmission data for vapor phase grown $\text{Pb}_{1-x}\text{Sn}_x\text{Se}$ alloys [35]. At low temperatures and for greater tin contents there is a larger discrepancy between the data and those from other authors. This is in part due to the

difficulty in obtaining accurate absorption edges because there are fewer interference fringes to serve as a reference for samples having $x = 6\%$, 7% , and 10% .

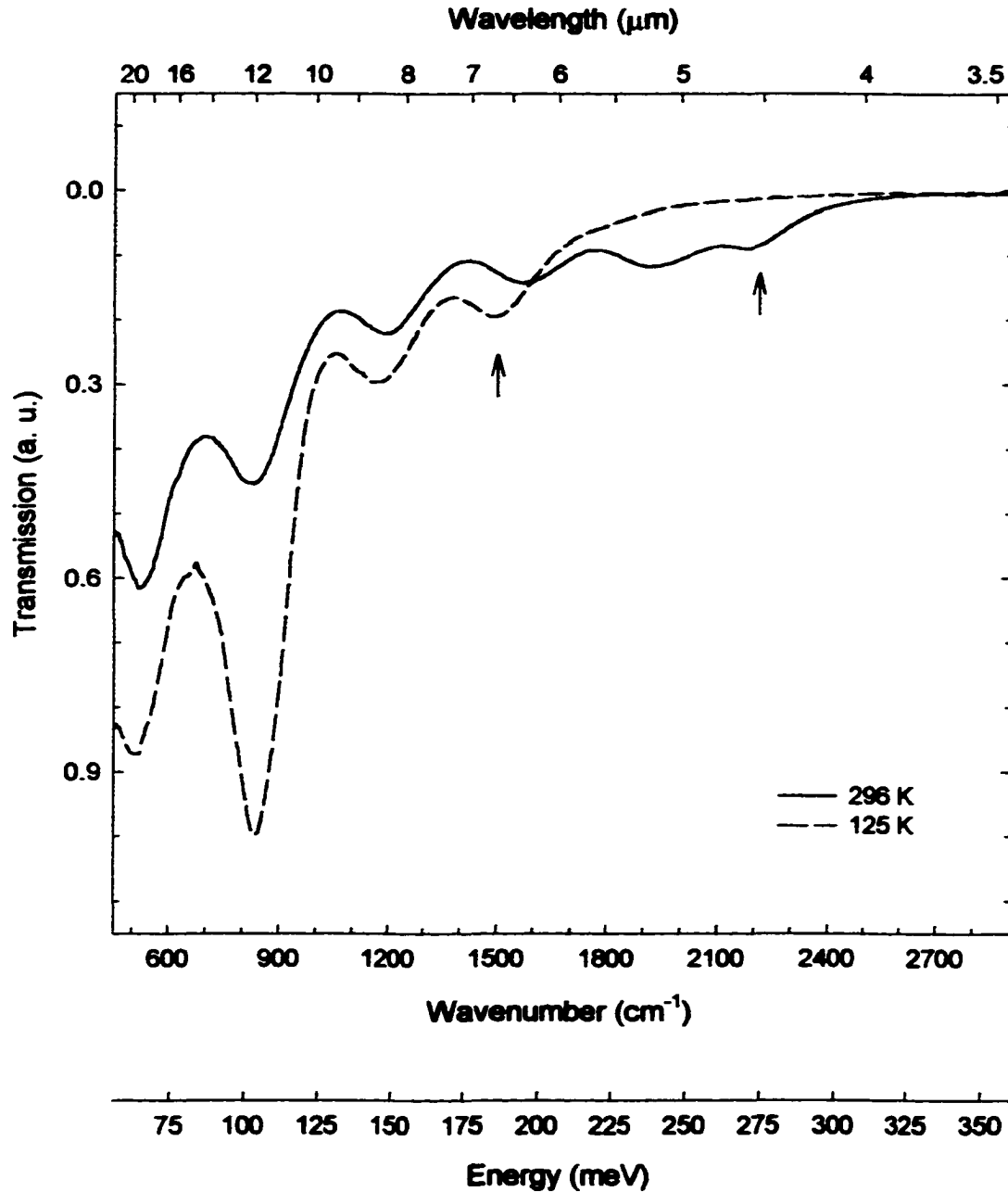


Figure 4.1 Transmission spectra of PbSe (H9) at room temperature (solid line) and at 125 K (dashed line). The arrows denote the fundamental absorption edges.

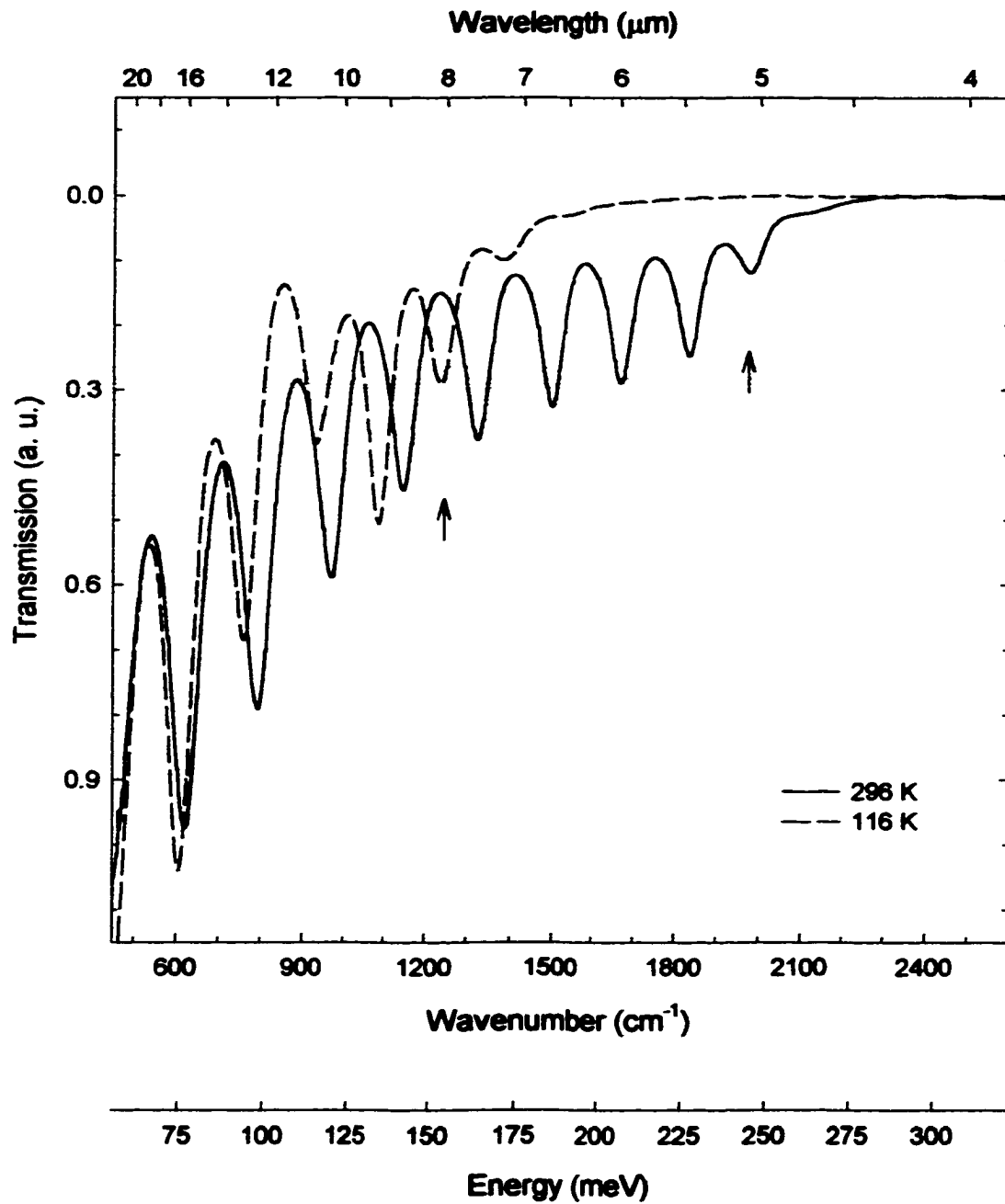


Figure 4.2 Transmission spectra of PbSnSe (H13, 3% tin) at room temperature (solid line) and at 116 K (dashed line). The arrows denote the fundamental absorption edges.

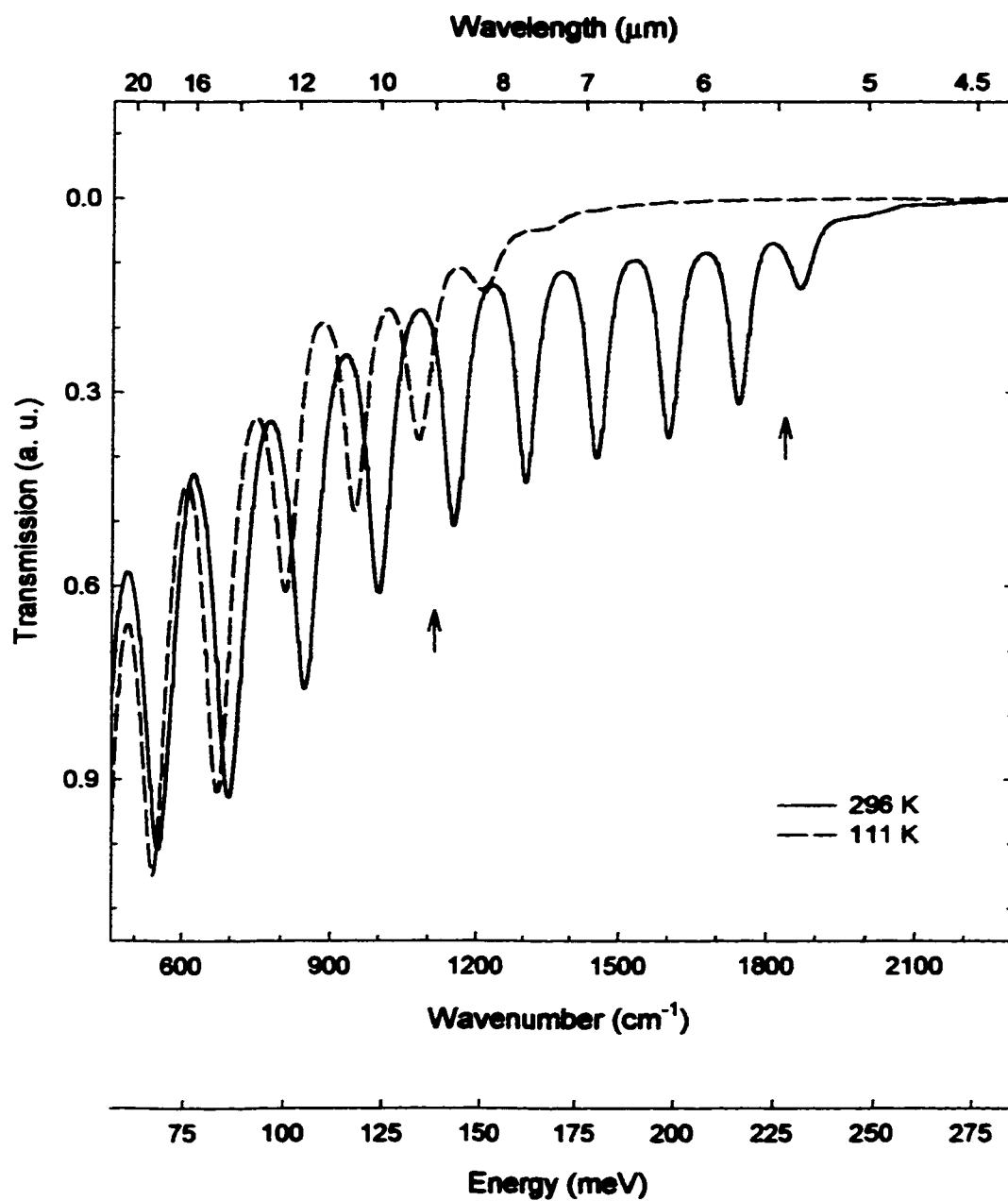


Figure 4.3 Transmission spectra of PbSnSe (H12, 5% tin) at room temperature (solid line) and at 111 K (dashed line). The arrows denote the fundamental absorption edges.

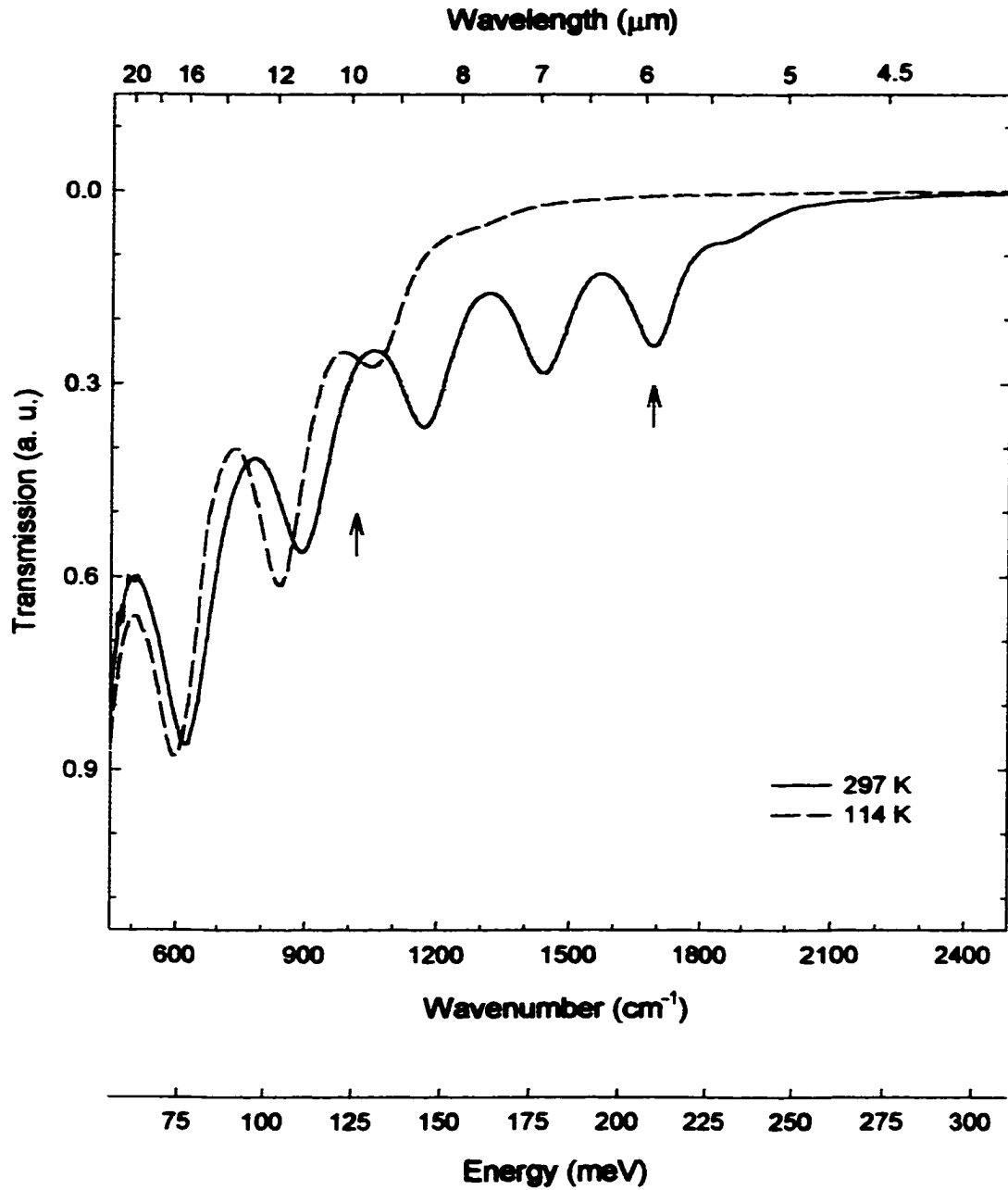


Figure 4.4 Transmission spectra of PbSnSe (H15, 6% tin) at room temperature (solid line) and at 114 K (dashed line). The arrows denote the fundamental absorption edges.

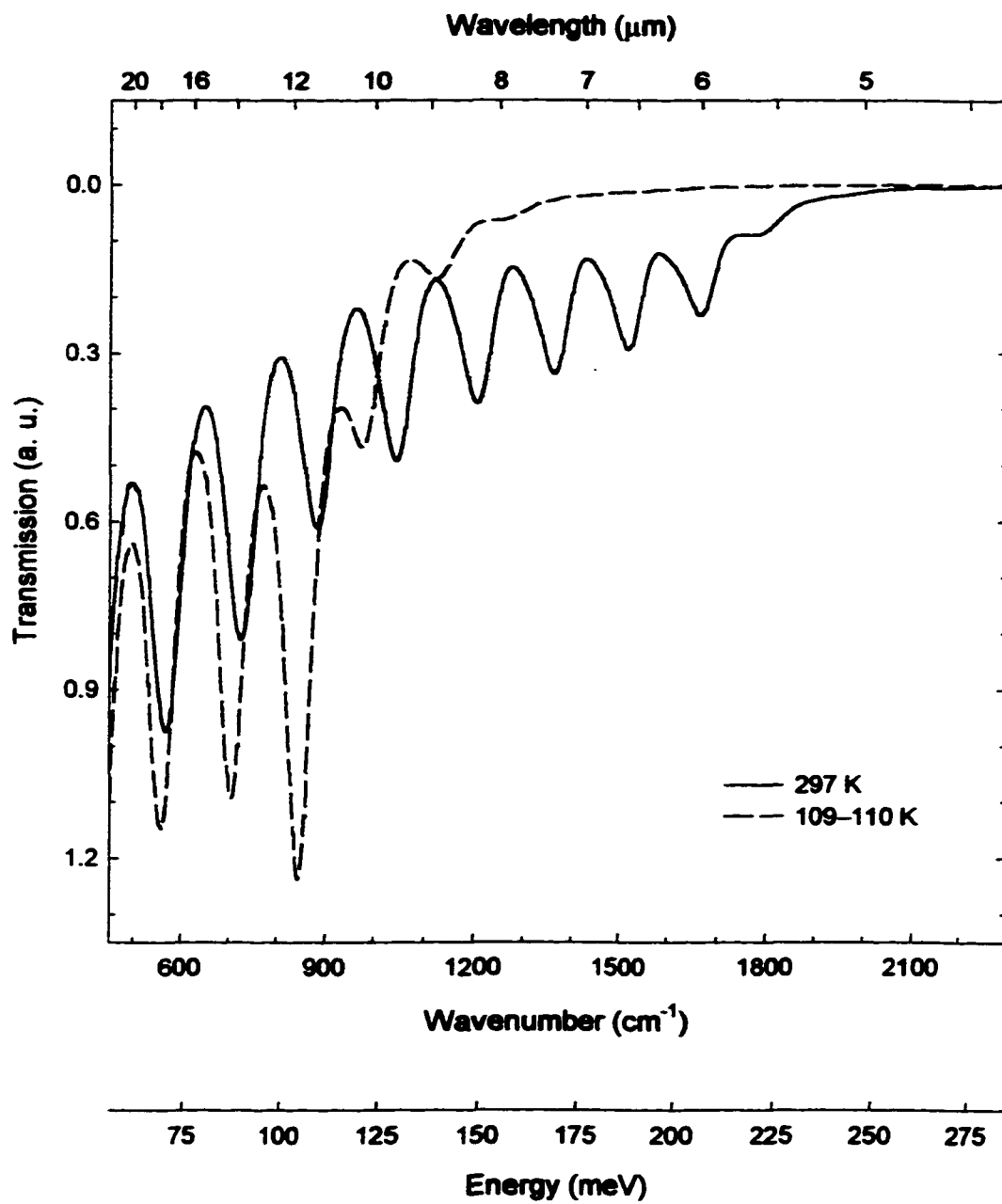


Figure 4.5 Transmission spectra of PbSnSe (H14, 7% tin) at room temperature (solid line) and at 109–110 K (dashed line).

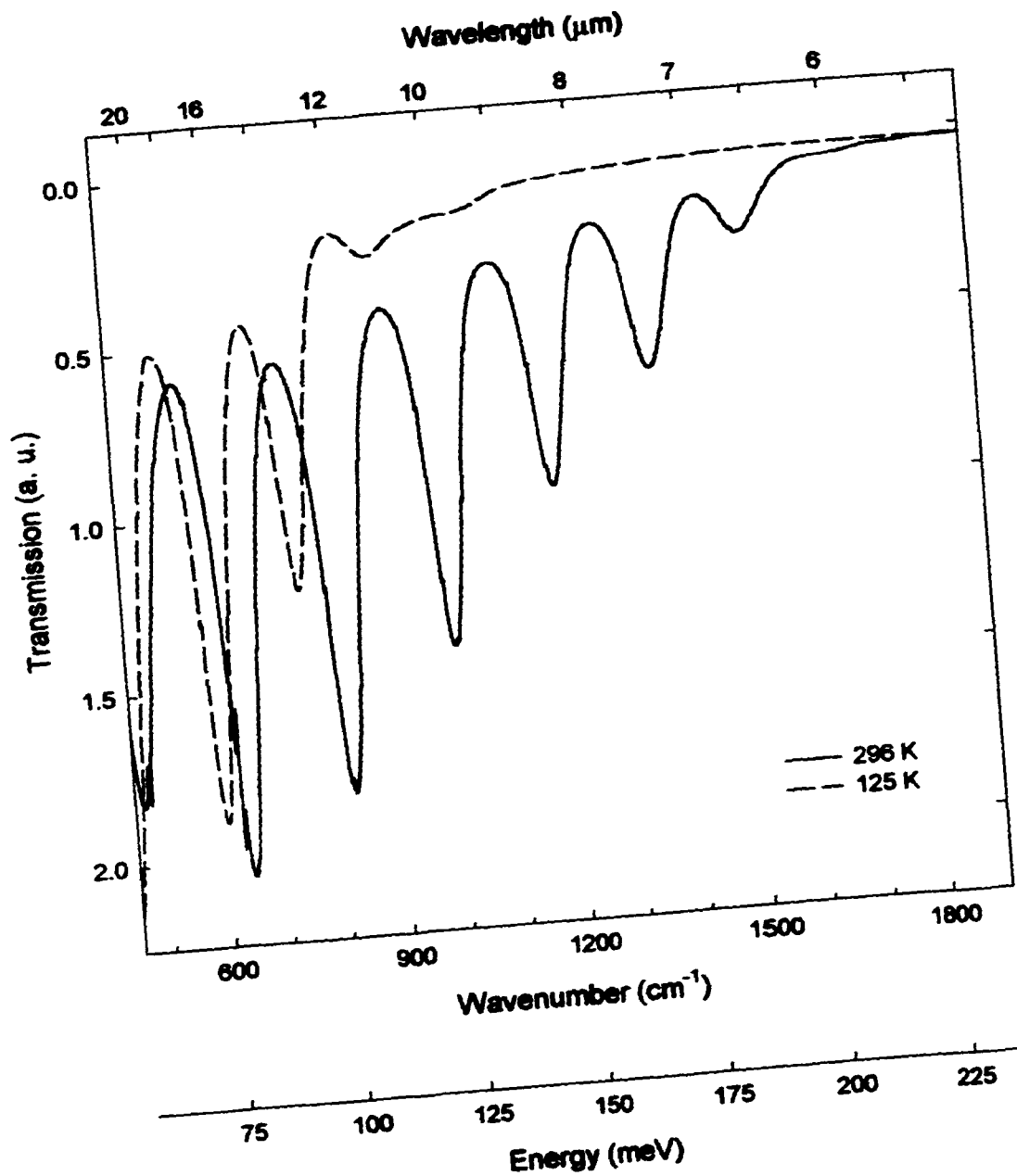


Figure 4.6 Transmission spectra of PbSnSe (H17, 10% tin) at room temperature (solid line) and at 125 K (dashed line).

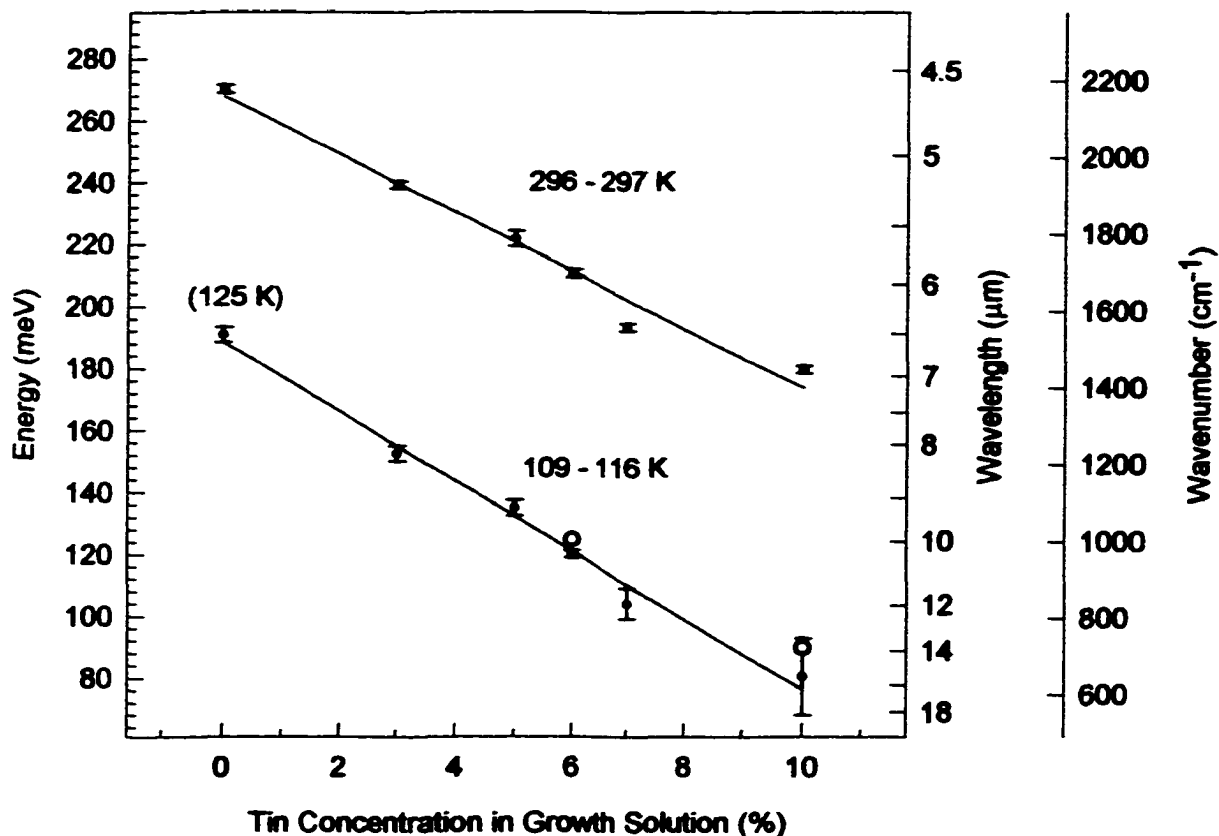


Figure 4.7 Absorption edge energy vs. percentage tin for $Pb_{1-x}Sn_xSe$ Layers with 0%, 3%, 5%, 6%, 7%, and 10% tin (H9, H13, H12, H15, H14, and H17) in the liquid growth solution. Data in unfilled circles are from laser emissions at 100 K [55]. Dotted lines are from transmission data at 297 K and 100 K [35].

4.3.2 Effect of Cryogenic Cycling

Transmission measurements for two samples, H9 (0% tin) and H12 (5% Sn) were performed following a cryogenic cycle. Sample H9 was initially characterized at 293 K, then cooled down to 125 K for low temperature measurement, then warmed up to 293.4 K to be re-tested. Measurements for sample H12 followed a similar sequence: 295.8 K, 111 K, and 294.3 K. Figure 4.8 shows the transmission spectra at room

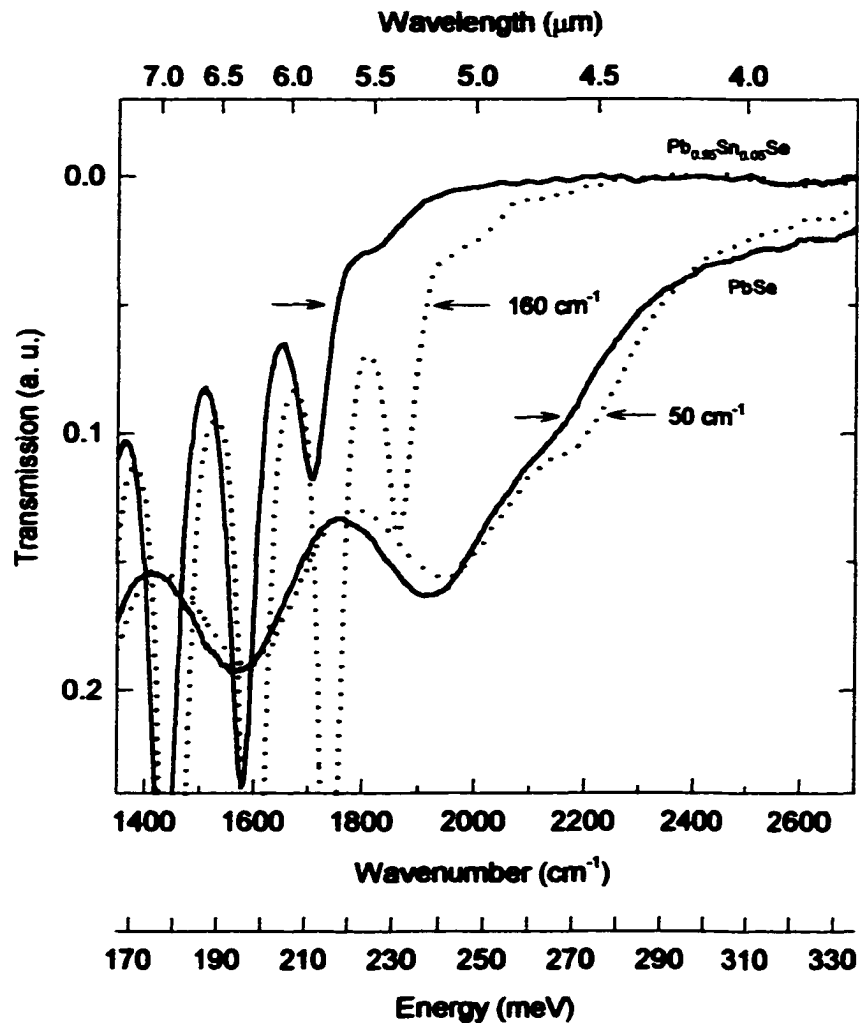


Figure 4.8 Room temperature FTIR transmission spectra for a PbSe (H9) and a Pb_{0.95}Sn_{0.05}Se (H12) layer before (dotted lines) and after (solid lines) cryogenic cooling. The ternary layer exhibits a much larger absorption edge shift than the binary layer.

temperature before and after cryogenic cycling. The absorption edge for both samples shifted toward lower energies as the result of thermal cycling. A much larger shift of $\sim 160 \text{ cm}^{-1}$ is seen from the ternary material than the $\sim 50 \text{ cm}^{-1}$ seen from binary material. Using previous published data of 0.41 meV/K (rate of change of absorption edge energy with temperature) for IV-VI materials [4], the difference of 1.5 K in sample heat sink temperature should only contribute to a change of 0.615 meV or $\sim 5 \text{ cm}^{-1}$ in absorption edge. The relationship between change in bandgap energy and change in strain for (100)-oriented PbTe layers has been derived from elastic moduli and deformation potentials [56],

$$\Delta\varepsilon_{\parallel} = 0.312 \Delta E_g \text{ (eV)}, \quad (4-1)$$

where ε_{\parallel} is the in-plane tensile strain. Using this relationship (reliable deformation potentials for PbSe could not be found) a shift of 50 cm^{-1} (6.15 meV) corresponds to a change in strain of 0.19% .

When examined under a Nomarski microscopy the PbSe layer, which was crack-free before the cryogenic cycling, showed surface cracks that has also been observed by other investigators [52]. HRXRD measurements of these cracked PbSe layers show a lattice parameter of 6.126 \AA (a value equal to that of the unstrained layer) suggesting a total relaxation of the 0.21% residual strain [5]. Thus the absorption edge shifts can best be explained by relaxation of residual strain in the crystal through the mechanism of crack formation due to the stress induced by cryogenic cycling. The HRXRD measurements of PbSe also revealed an increased full width half maximum value, from below 200 arc sec to 238 arc sec . Thus the crystalline quality also suffered degradation due to the thermal expansion mismatch strain between 125 K and room temperature.

It was also noted that the already cracked PbSnSe layer sustained more cracks after cryogenic cycling. Using Eq. (4-1) and assuming that these additional cracks

cause complete relaxation for a shift of 160 cm^{-1} (19.84 meV), an as-grown residual strain of 0.62% is obtained for the ternary layer. This value is in good agreement with the 0.74% residual strain expected if the LPE-grown layer is not subject to plastic deformation. As-grown PbSnSe layers have larger residual strain, thus a larger absorption edge shift, than as-grown PbSe layers. The primary strain relaxation mechanism for the PbSnSe layer is through the crack formation and that plastic deformation plays only a small part. This is supported by the fact that all PbSnSe as-grown layers were cracked.

Both the PbSnSe and the PbSe LPE layers were grown on the same MBE substrate but the former is twice as thick ($4.7 \mu\text{m}$ vs. $2.2 \mu\text{m}$) than the later. If the residual strain is the same for both, one may argue that the thick layer would be more likely to crack (when exceeding the critical thickness). The much larger residual strain ($3\times$) in the ternary layer, however, should accommodate even greater critical thickness before its relaxation. Therefore, one must consider the possibility of solid solution hardening in the PbSnSe layer as the main cause for cracking.

4.4 Discussions and Summary

This study shows that the absorption edge energy of $\text{Pb}_{1-x}\text{Sn}_x\text{Se}$ alloys grown by LPE growth method decreases monotonically as tin content increases. At low temperatures, the absorption edge also shifts congruently toward lower energies for all alloy compositions ($x = 0$ to 10%). These properties are important with respect for electrical confinement in designing heterostructure lasers. In this aspect the LPE-grown layers on silicon-based MBE substrates appear to behave like traditional bulk or epitaxial $\text{Pb}_{1-x}\text{Sn}_x\text{Se}$ layers that have been used to fabricate commercially available PbSnSe lasers.

All transmission spectra of the LPE-grown $\text{Pb}_{1-x}\text{Sn}_x\text{Se}$ do not show the absorption edge of the MBE-grown PbSe. (Absorption edges of both PbSeTe and

PbSnSeTe layers have been observed on the transmission spectra of such LPE-grown heterostructures [4].) This may be due to the diffusion of tin from the LPE-grown PbSnSe layer to the MBE-grown PbSe layer since the former was grown at a much high temperature than the latter. For example, in sample H17 the LPE layer is much thicker than the MBE layer (4.51 μm vs. 0.81 μm), and it is reasonable to expect diffusion of tin across the thickness of the MBE layer during the 40 minute LPE growth.

Furthermore, the LPE growth is not isothermal while MBE is isothermal. As the LPE growth temperature gradually decreases during growth, tin segregates less into the solid from the liquid growth solution and the bandgap of PbSnSe can increase with the layer thickness. Solid diffusion at the heterointerface and change of composition as a function of layer thickness can result in “band tilting” [57]. Further study on the effect of band tilting may be required to fully understand these epitaxial layers grown by the hybrid LPE-MBE method.

Lasers operating at cryogenic temperatures must endure numerous temperature cycles without degradation. Some potential problems need to be addressed if laser devices are to be fabricated from these special IV-VI materials. These include the significant increase in microscopic cracking and shift of absorption edge after cryogenic cycling. The cracking associated with solid solution hardening seen in PbSnSe layers may limit the range of composition attainable. More research is needed to evaluate the correlation of cryogenic cycling and solid solution hardening for layers having greater tin content.

CHAPTER 5

Emission Studies of diode Laser Pumped IV-VI Epilayers

5.1 Introduction

An unusual property of IV-VI semiconductors is the remarkably high intrinsic carrier concentrations associated with deviations from stoichiometric composition. Excess metal (chalcogen vacancy) makes the material *n*-type and excess chalcogen (metal vacancy) makes it *p*-type. In crystals grown from lead-rich liquid solutions by liquid phase epitaxy (LPE) the electron concentration is well into the 10^{18} cm^{-3} range [58, 59], driving the Fermi level inside the conduction band edge. This is why *n*-type IV-VI semiconductors behave like a dilute metal with no carrier freeze-out at low temperatures.

A well-accepted explanation for this phenomenon was first proposed by Parada and Pratt [40] using one-electron energy band calculations on PbTe and subsequently confirmed by other theoretical investigations [60, 61, 62, 63]. The central theme of the Parada-Pratt model is that the localized potential of a lattice vacancy strongly perturbs the valence band states of the vacant atom such that some states are liberated with associated charge transfer. The energies of said vacancy defect states were calculated and were shown to reside deep inside the electronic energy bands. There have since been a number of experimental works [3, 64, 65] conducted in an effort to explore and quantify the physical properties of the predicted defect states.

The understanding of defect processes in semiconductors is not straightforward and often requires analyzing data from several different experimental techniques [66]. Photoluminescence (PL) spectroscopy is a direct and widely used tool for studying

electronic transitions in semiconductor compounds. PL experiments are usually conducted at low temperatures to prevent thermal ionization of the optically active centers and to minimize spectral line broadening. In this work, photoluminescence experiments of IV-VI epilayers grown by LPE were performed. Unusual and interesting experimental results, observed in the course of this study, are reported in this chapter.

5.2 Photoluminescence Experimental Procedures

The PL experiments were performed using a modified Bruker IR/98 FTIR spectrometer. The spectrometer (described previously in Chapter 2) is an interferometer type instrument with a KBr beamsplitter and is capable of performing transmission measurements in the spectral range of $400\text{--}4000\text{ cm}^{-1}$. The existing infrared radiation source is a globar situated in the source chamber whose radiation is directed to the interferometer chamber through a swivel plane mirror. A photoluminescence chamber containing a custom-designed cryostat and optics was constructed and placed adjacent to the source chamber. The radiation from the PL chamber can enter into the source chamber through an open port. It can be guided into the interferometer chamber by repositioning the swivel plane mirror. The radiation of interest is subsequently processed by the spectrometer in the manner described in Chapter 2.

The cryostat interfaces with the PL chamber through a cylindrical housing. The cylindrical housing is equipped with a germanium window and pipes that can be connected to a vacuum pump. The top portion of the cryostat is a hollow stainless steel cylinder. The lower portion is a copper arm that houses the PL assembly (the pump laser and the sample), electrical connectors, a heater, and a temperature sensor.

A near infrared GaAlAs diode laser (Hitachi LD HL 8325G) with emission wavelength of 830 nm (1.5 eV) was used as the pump source for the PL measurements.

The laser beam was focused by a Melles Griot Micro PL-CX lens with 4.0 mm focal length. The laser, the lens and the sample were mounted on separate copper housings that were screwed to the copper arm of the cryostat. The arrangement allowed a $\sim 45^\circ$ incident angle of the laser beam. By rotating the cryostat the laser beam was aligned with a small ZnSe window (~ 1 cm in diameter) that has a transmission range of 0.63 to $18 \mu\text{m}$. The geometry and optical pathway in the PL experimental setup is shown in Figure 5.1.

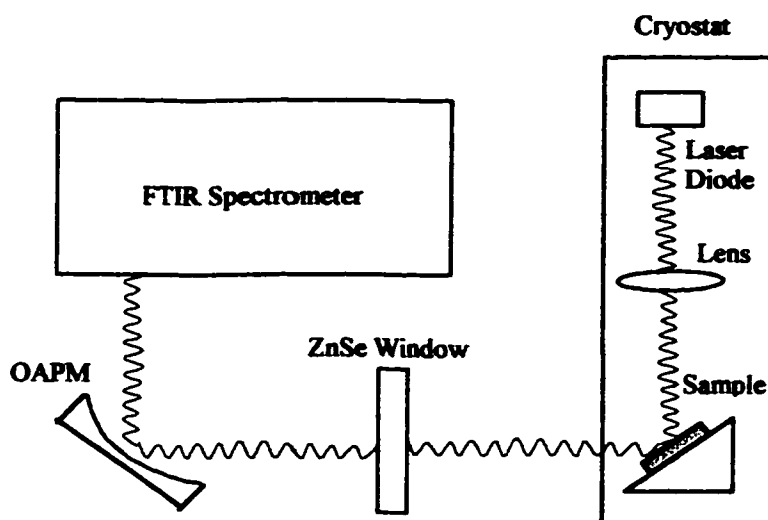


Figure 5.1 Schematic of the photoluminescence experimental setup. The geometry of the laser, the lens and the sample assembly allows easy alignment of the laser beam. Emission from the diode laser is focused by the lens. Scattered PL from the sample, after transmission through a ZnSe window, is guided to the source chamber by a combination of a plane mirror and two off-axis parabolic mirrors (not all of which are shown). A swivel plane mirror in the source chamber (not shown) is positioned to direct the beam to the interferometer chamber, therefore bypassing the globar assembly.

The cryostat was cooled by adding liquid nitrogen to its top portion and could be heated up to 324 K by a resistive heater mounted at the end of the copper arm. A

silicon temperature sensor is placed near the sample to monitor the sample heat sink temperature. The heater and the sensor are connected to a temperature controller (LakeShore 330 Autotuning). For obtaining temperatures above 324 K a homemade device was used consisted of a resistive cartridge heater (Chromalox CIR-2013 120V 100W) mounted on a long copper rod. The rod reached to the bottom of the hollow cylinder where it was in direct contact with the copper arm of the cryostat.

The laser package contains a reverse-biased monitor photodiode that shares a common ground with the laser diode. The laser diode was driven by a modular laser diode controller (ILX LIGHTWAVE LDC-3752). The photodiode was biased separately by a 5 V DC power supply (Tetronix PS281) and its output current was measured by a current meter (Keithley 197 Autoranging Microvolt Digital Multimeter). Normally, the current meter should display a 0.5-mA reading when the laser is operated continuously (cw) at 120 mA. At room temperature and 120 mA the output power of the laser, which is linear with current, is 40 mW according to the manufacturer's specification. This arrangement allows the experimenter to monitor the actual output of the pump laser during its operation.

For alignment purpose, a small Radioshack light bulb was connected instead of the laser diode and the reflected light by the sample was modulated by a mechanical chopper placed between the detector and the interferometer. The cryostat was adjusted vertically and rotated until the signal seen on an oscilloscope was maximized. For control purpose, PL measurements were also conducted using dummy samples including a piece of silicon wafer, a mirror, and a BaF₂ substrate.

For test runs at room and above room temperatures the pump laser was operated cw at 120 mA (unless stated otherwise). Higher current levels were employed for low temperature testing. The spectral resolution of the spectrometer was set at 4 cm⁻¹ for all PL measurements. The cryostat housing was kept under vacuum at below 10 mTorr

using a homemade cryogenic sorption pump. The spectrometer was kept under vacuum at below 20 mBar as done for transmission measurements (Chapters 3 and 4). The optical bench of the spectrometer was normally flushed with purified dry nitrogen before and after the PL measurements.

In general, test runs were conducted after the system (vacuum pressures, temperature, etc.) stabilized. With the sample loaded and the pump laser turned off, the spectrum (reference spectrum) of the thermal background (blackbody radiation) of the system was measured. This was followed by data collection with the laser turned on. Alternatively, the spectral data with laser on was collected first, followed by the measurement of the reference spectrum. The reference spectrum was subtracted from the measured sample spectrum to obtain a normalized sample spectrum.

To test the system, trial runs were performed on an MBE-grown superlattice structure containing GaInSb/InAs superlattice wells (courtesy of Y.-H. Zhang, Hughes Research Laboratories, Malibu, California). Diode lasers have been fabricated from structures similar to this sample, and they have exhibited emission wavelengths between 3 and 4 μm [67]. Using the modified Bruker FTIR spectrometer, PL spectra from this sample were obtained at liquid nitrogen temperatures. Figure 5.2 shows an example of such a spectrum averaged over 500 scans with the pump laser operating at 160 mA.

The IV-VI samples (a few mm^2 to one cm^2 in size) were grown from lead-rich growth solutions by liquid phase epitaxy on BaF_2 substrates. The growth procedures have been described elsewhere [4]. The samples were loaded onto the PL assembly as-grown, i.e., with substrates attached and no special preparation. Photoluminescence studies were performed on samples having binary, ternary, and quaternary epilayers, see Table 5.1.

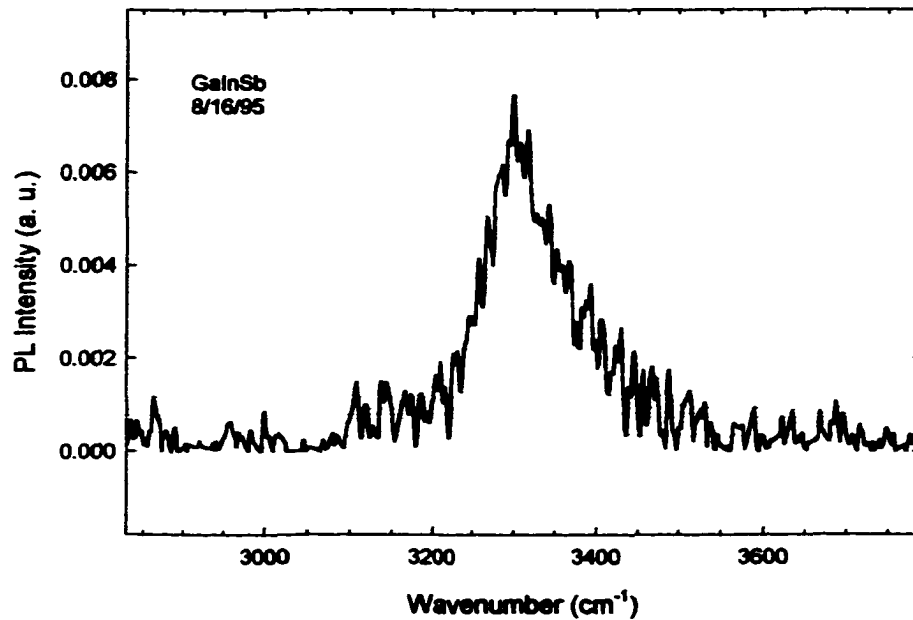


Figure 5.2 Photoluminescence spectrum at 82 K obtained from the GaInSb layer of a superlattice structure grown by MBE. The FTIR spectrometer resolution was 4 cm^{-1} . The actual temperature ranged from 82.02 to 82.54 K during measurement.

Table 5.1 Structure of IV-VI samples grown by liquid phase epitaxy. The samples are not intentionally doped (they are intrinsic *n*-type semiconductors) and the layers are typically 2-3 μm thick.

Sample #	Structure
S37	PbSe/PbSeTe/(100) BaF ₂
S43	PbTe/PbSeTe/(100) BaF ₂
Z26, C3	PbSeTe/(100) BaF ₂
C36	PbSnSeTe/PbSeTe/(100) BaF ₂ , [Sn]=5%
C9	PbSnSeTe/PbSeTe/(100) BaF ₂ , [Sn]=40%

5.3 Experimental Results

In the beginning, the goal of conducting the photoluminescence experiments was to investigate the band-to-band transitions in the above-mentioned LPE-grown IV-VI epilayers. The experiments were performed at cryogenic temperatures in order to minimize the thermal excitation of electrons across the narrow bandgap of the IV-VI materials. The band-to-band transitions at the expected bandgap energies were not observed on the spectra of the samples. Instead, some unexpected, intense, and very sharp features were observed at photon energies beyond the bandgap energies. The anomalous feature on the raw (not normalized) PL spectrum, shown in Figure 5.3, stands well above the background noise level and the magnitude of its intensity is comparable with the height of the blackbody radiation curve. This is remarkable considering the fact that the detector is much less sensitive at the photon energy (~ 3220 cm^{-1} or ~ 3.1 μm) where the feature is observed.

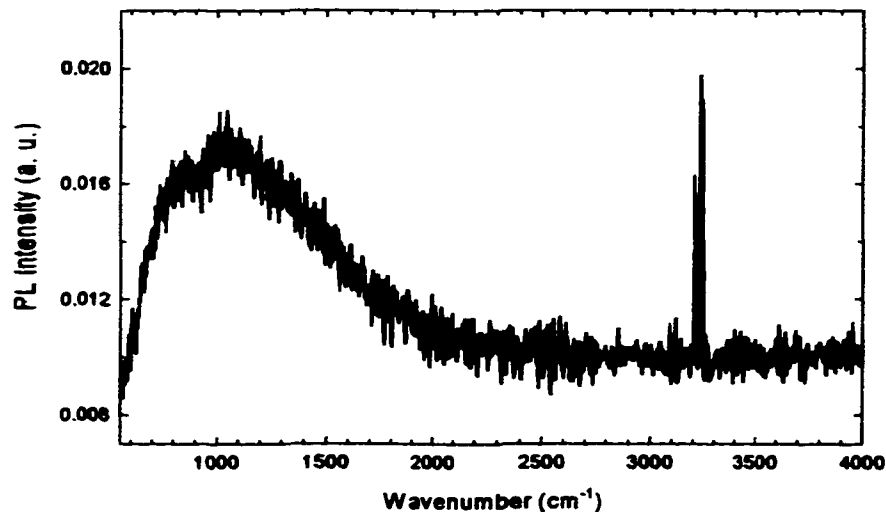


Figure 5.3 Photoluminescence spectrum (before normalization) from a IV-VI semiconductor sample showing a feature at photon energies well above the bandgap for this material. The bandgap PL energy of this sample, which was not seen, is expected at ~ 1700 cm^{-1} .

The full range (up to 5000 cm^{-1}) of the raw spectrum is actually comprised of two photoluminescence features that are mutually symmetric (i.e., mirror images) with respect to 3950 cm^{-1} . (Recall that this number is an integer division of the frequency generated by the reference laser in the interferometer). A similar spectrum showing spectral aliasing can be found in Appendix D, Figure D.1. Initially, the spectrum was misinterpreted as having two physical PL peaks of different energies. It was understood later that the peak below 3950 cm^{-1} was the true feature. The peak above 3950 cm^{-1} was not real and was due to the “fold back” of the next spectral replica at (see Appendix C, Figure C.2). The measurement parameters were set according to the instrumental specifications. For example, the HFQ parameter was set at 5000 and the SSP parameter was set at -1 (see Appendix D), which should allow adequate sampling for signal frequency up to 7900 cm^{-1} . In retrospect it was suspected that the FTIR system must have generated an inadequate sampling frequency (f_s) of 3950 cm^{-1} due probably to software control error. To avoid complication, some PL spectra shown in this Chapter were truncated at wavenumbers above 3950 cm^{-1} .

Photoluminescence spectra from a $\text{PbSe}_{0.78}\text{Te}_{0.22}$ layer (sample #Z26) were measured at cryogenic temperatures to above room temperature. Figures 5.4 and 5.5 show PL spectra collected in two separate sequences during the same day. Like what was shown in Figure 5.3, these samples exhibited PL intensities similar to the blackbody intensity.

Interestingly, each of the above spectra exhibits a peak at lower energy and a broader feature at a higher energy. The PL feature at the higher energy becomes more resolved as pump power increases. It is also shown in Figure 5.5 that at a given sample heat sink temperature both the intensity and the energy of the PL increase with the irradiation power of the pump laser. The relationship is plotted in Figure 5.6.

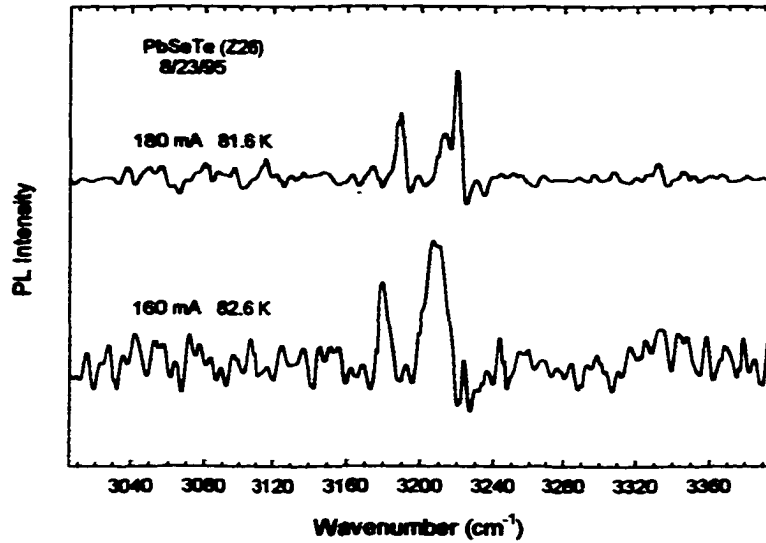


Figure 5.4 PL spectra for $\text{PbSe}_{0.78}\text{Te}_{0.22}$ (Z26) measured consecutively while increasing the laser current. The temperature varied from 82.48 to 82.81 K at 160 mA and from 81.19 to 82.04 K at 180 mA during the measurements. The temperatures shown are the median values. The top plot was averaged over 300 scans and the bottom, 100 scans.

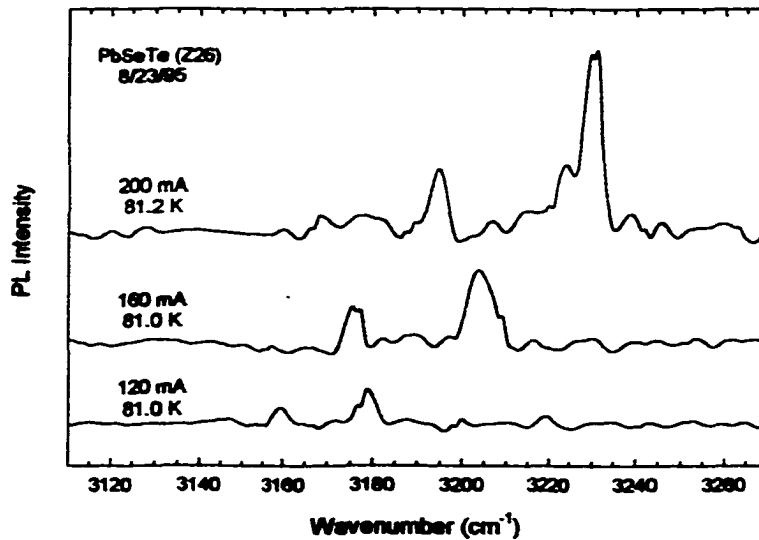


Figure 5.5 PL spectra for $\text{PbSe}_{0.78}\text{Te}_{0.22}$ (Z26) taken consecutively while increasing laser current. The temperatures shown are the median values with maximal deviations no greater than 0.7 K during each measurement. The spectra were averaged over 500, 500 and 300 scans at the laser current of 120, 160, and 200 mA, respectively.

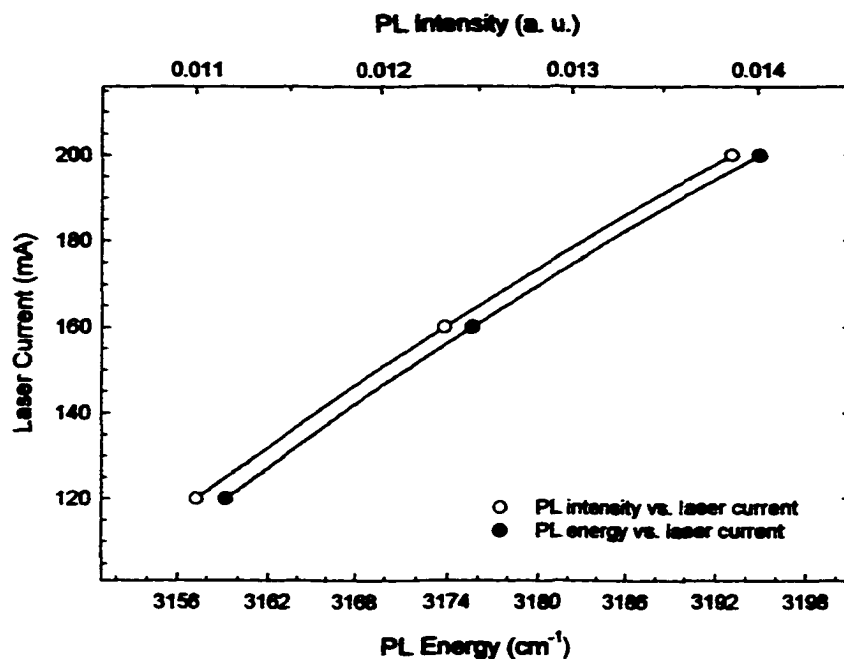


Figure 5.6 Plots of PL intensity vs. laser current, top, and PL energy vs. laser current, bottom, from the lower energy peak of the luminescence in Figure 5.5. The slope of the bottom plot is $\sim 0.41 \text{ cm}^{-1}$ per mA.

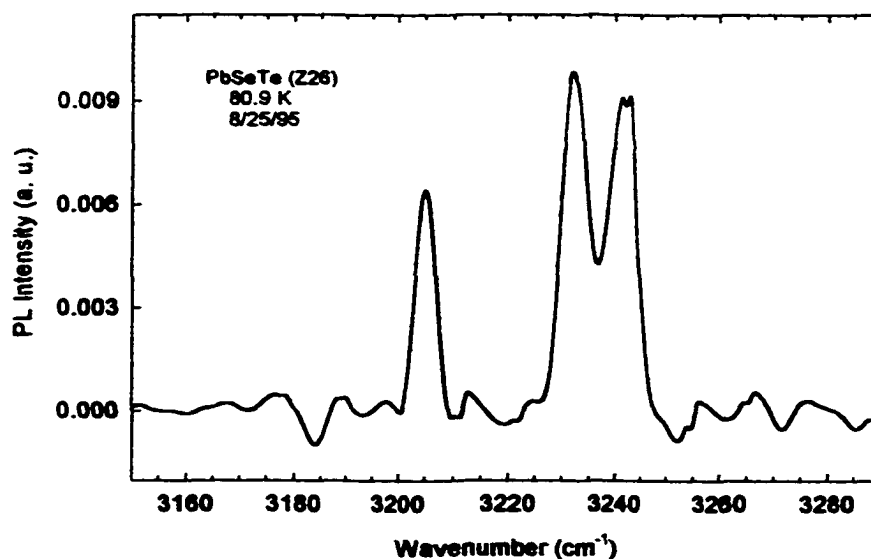


Figure 5.7 PL spectrum for PbSe_{0.78}Te_{0.22} (Z26) at 81 K and 220 mA laser current. The spectrum was collected over 1000 scans (longer than 30 minutes) during which time temperature varied from 80.11-81.62 K.

When irradiated at a still higher laser power (current = 220 mA) the higher energy PL feature becomes completely resolved, see Figure 5.7. The three luminescence peaks have energy separations of, from left to right, 27 and 10 cm^{-1} compared to 29 and 6 cm^{-1} . The intensity of the PL feature in the raw spectrum, shown in Figure 5.3, now rises above the height of the blackbody spectrum.

PL spectra for this sample were obtained from below room temperature to above room temperature, see Figure 5.8. While multiple PL peaks were observed at low temperatures, a single peak was obtained at higher temperatures. The luminescence energy increases with temperature similar to the bandgap energy of IV-VI semiconductors. The linewidth of this luminescence, however, does not show temperature broadening normally seen in band-to-band transitions. Amazingly, the intensity of luminescence is also not affected by high temperatures. The PL intensities in general are far above the background and it is no longer necessary to normalize the spectra.

To investigate further the behavior of the unusual luminescence, PL spectra were collected over small increments of temperature at even higher measurement temperatures. While the temperature drift during a test run at cryogenic temperatures did not seem to affect the quality of the spectrum collected, it is not true at higher measurement temperatures. It is important that the temperature be stable to within half a degree at higher temperatures. Figure 5.9 presents a complete series of PL spectra of the sample taken consecutively over small increments of temperature in one day. The PL intensity appears to have either diminished or disappeared at certain temperatures. The reason for this behavior is not clear at this time.

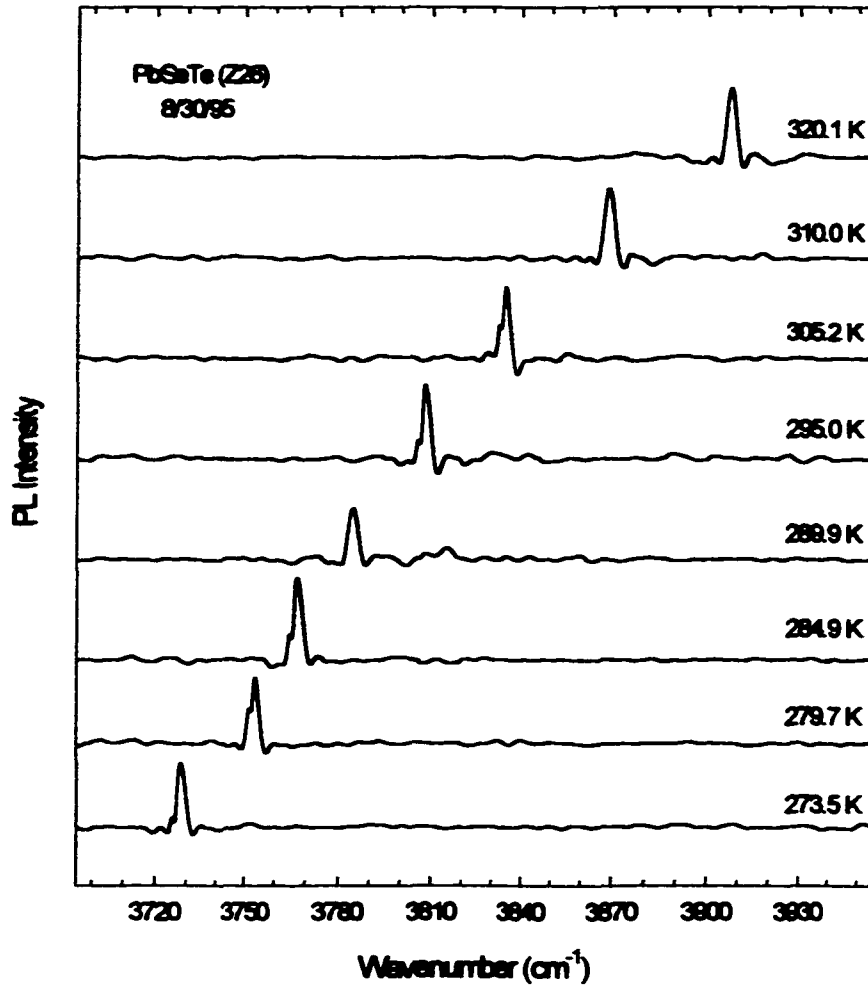


Figure 5.8 A series of PL spectra for PbSeTe (Z26) measured at below and above room temperatures. The temperature variation during a test run is within ± 0.1 K of the median values shown on the plot. The bottom five spectra were taken in sequence while the top three were not. All spectra were averaged over 100 scans and plotted using the same scale.

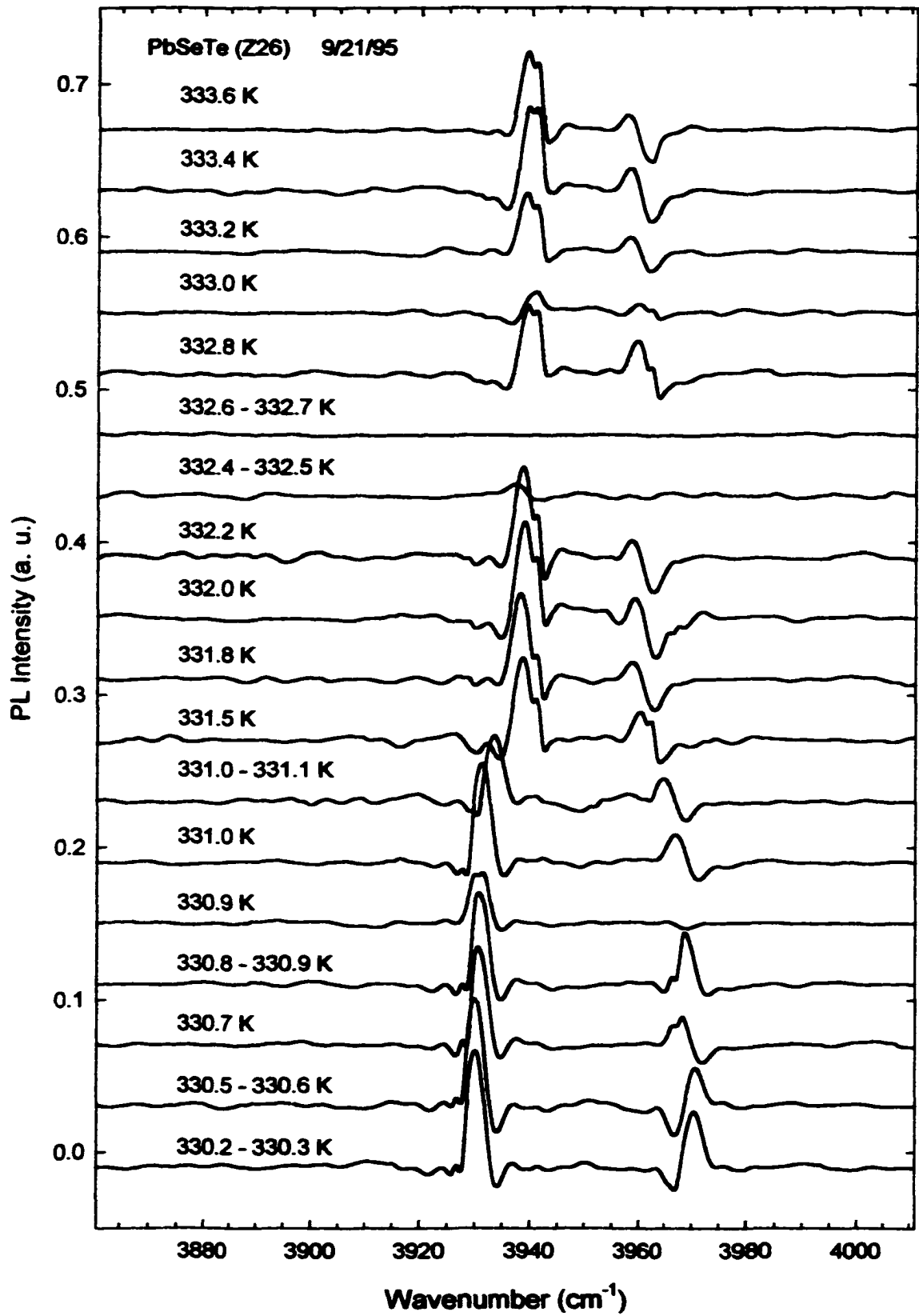


Figure 5.9 (a)

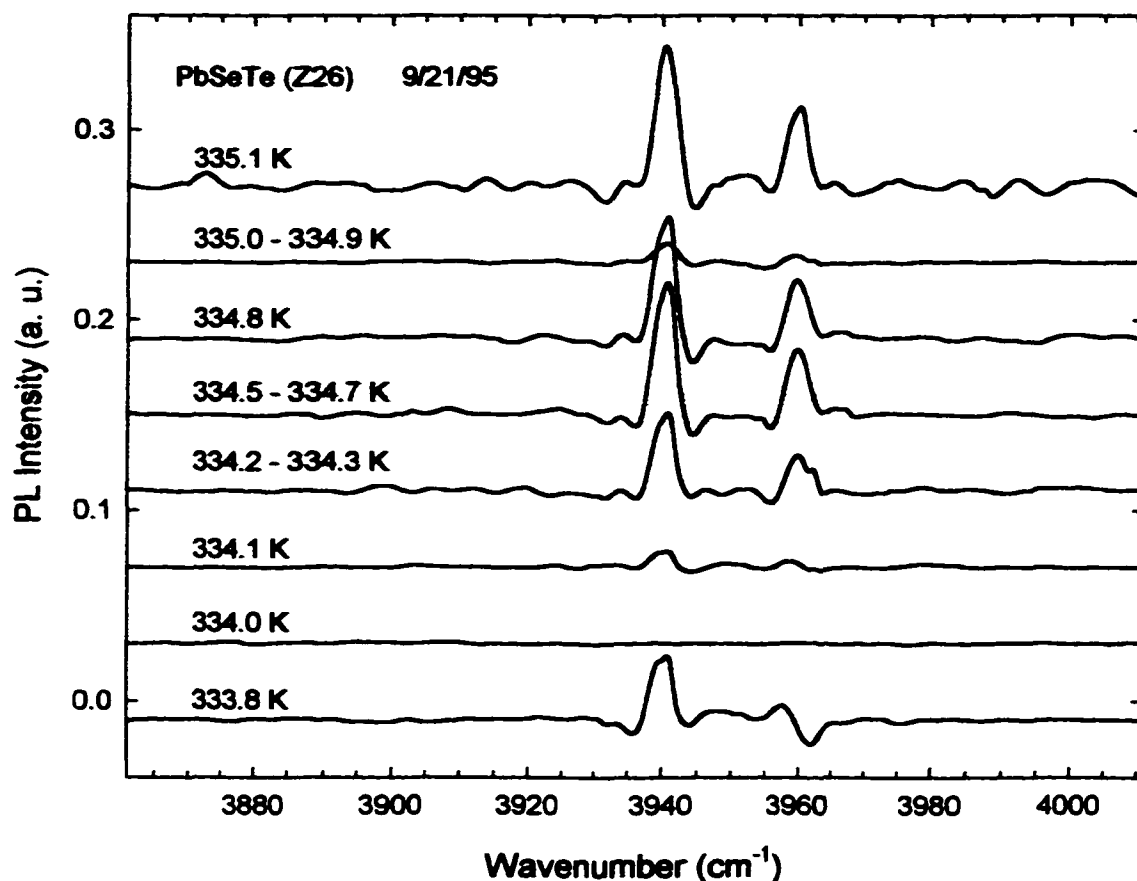


Figure 5.9 (b)

Figure 5.9 High temperature PL spectra of PbSeTe (Z26) at 330.2-342.0 K in three parts: (a) previous page, (b) this page, and (c) next page. In parts (a) and (b) the left peak in each spectrum is a real feature while the right peak is an alias. The lower six spectra in part (c) show a complex feature around 3950 cm^{-1} (the sampling frequency) made up of the real and the alias PL peaks. As the true PL peak moves beyond 3950 cm^{-1} it begins to “fold back” showing an alias to the left of 3950 cm^{-1} . This phenomenon is seen on spectra in the middle and the top portions of part (c). Numbers of scans range from 10 to 100. There was no correlation between the smoothness of a spectrum and the number of scans per measurement.

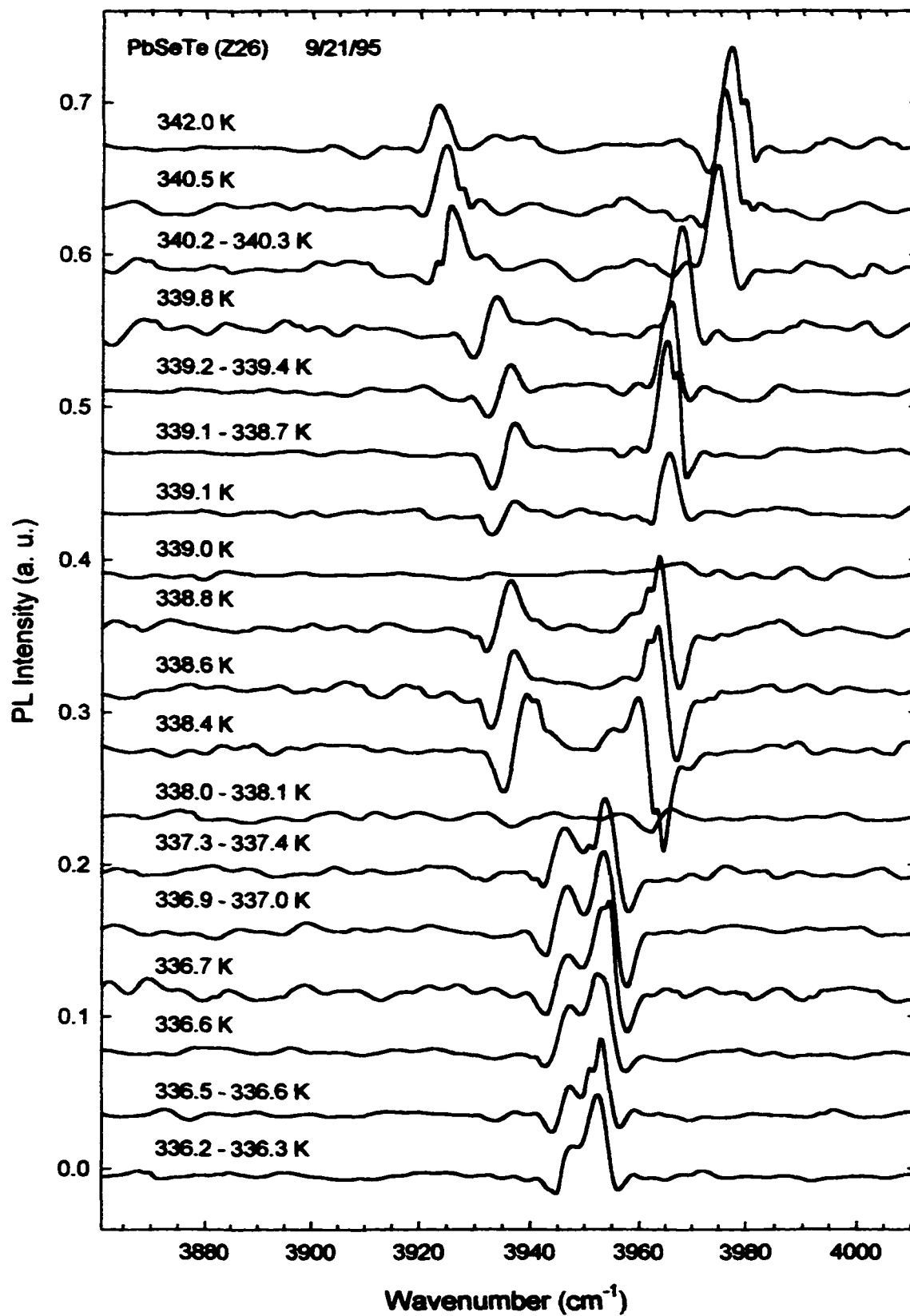


Figure 5.9 (c)

A plot of peak PL energies as a function of temperature in the above ascending temperature series is shown in Figure 5.10. Interestingly, the PL energy “hops” at certain temperatures.

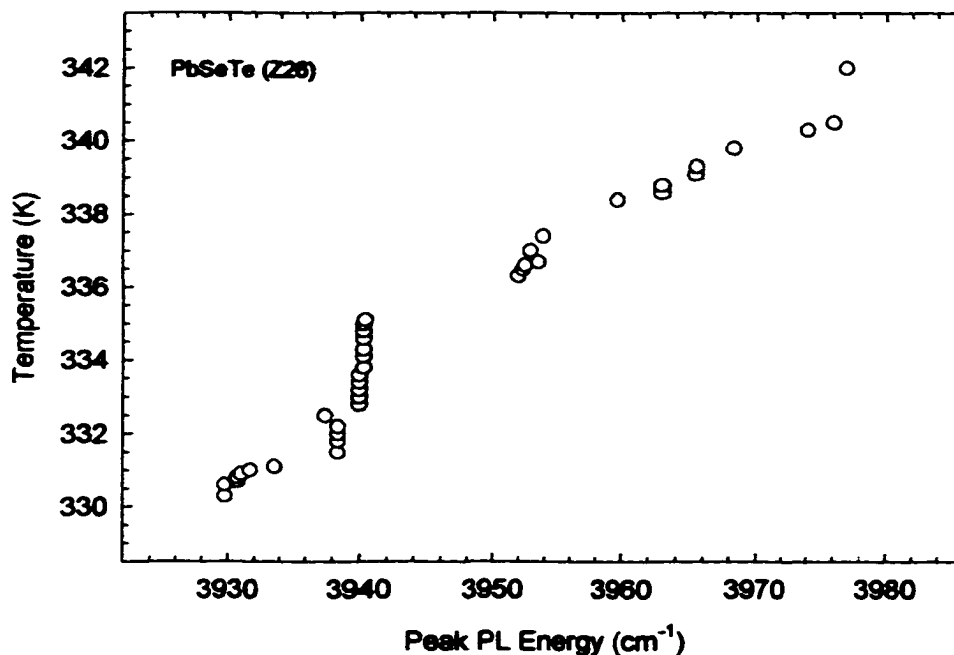


Figure 5.10 PL energy vs. temperature plot for PbSeTe (Z26) based on spectral data in Figure 5.9.

Room temperature and higher temperature luminescence measurements were also performed on several other LPE-grown IV-VI samples. Figure 5.11 shows room temperature spectra of a PbSeTe layer (similar to Z26) and Figure 5.12, room temperature spectrum of a PbSnSeTe ([Sn]=5%) layer. Notice that the room temperature PL among these two different samples occur at the same energy. Still, more amazing findings were observed on the PL spectra obtained at the same two temperatures (305 K and 315 K) from four different samples having binary, ternary, and

quaternary ([Sn]=40%) compositions. The pinning of the PL energy was quite evident on these spectra shown in Figure 5.13.

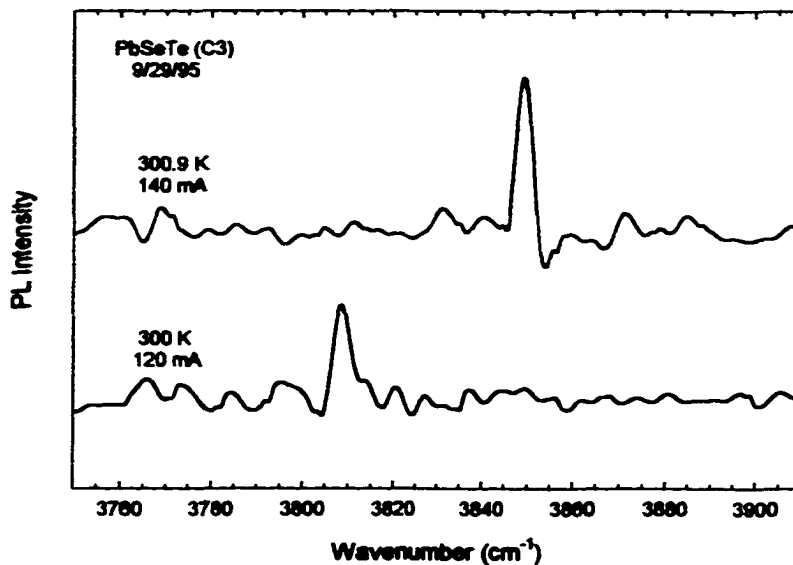


Figure 5.11 Room temperature PL spectra of PbSeTe (C3) at two different temperatures and laser current. Notice the ~ 40 cm⁻¹ span in PL energy.

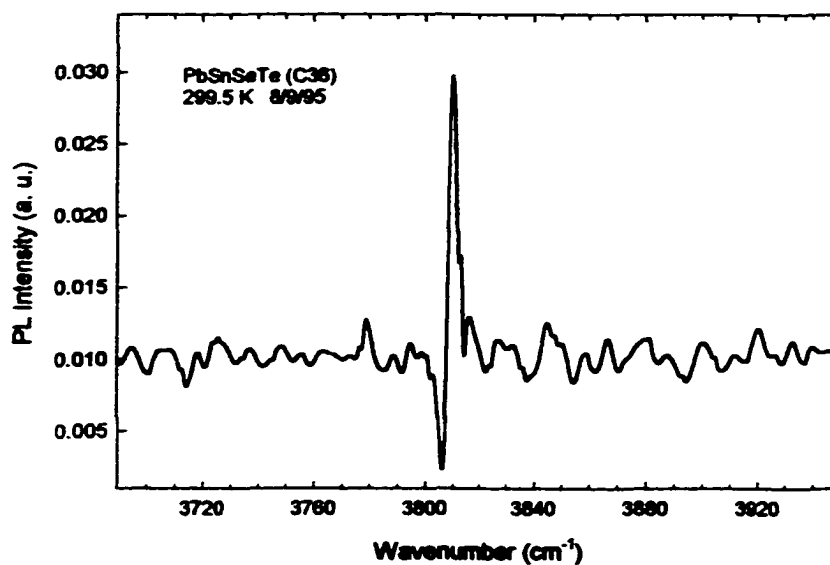


Figure 5.12 Room temperature PL spectrum of the PbSnSeTe layer (C36, [Sn]=5%). The pump laser current is 120 mA.

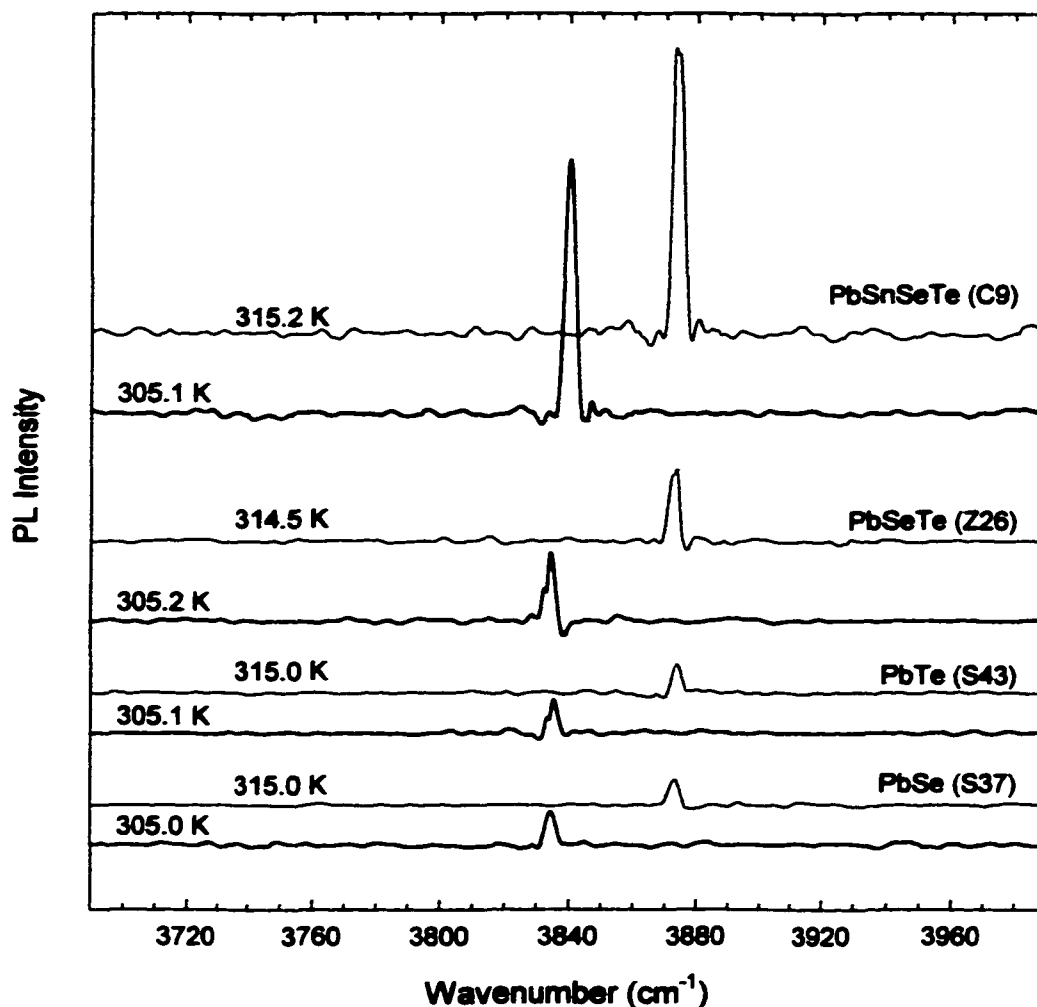


Figure 5.13 PL spectra for four different samples at two temperatures (~ 305 K and ~ 315 K) using 120 mA laser current. The ternary sample's 305 K spectrum was previously shown in Figure 5.10. The PL energies appear to have been pinned regardless of sample composition.

The quaternary sample (C9) whose top epilayer contains 40% tin was also subjected to a series of PL measurements while temperature was raised by small increments. Like the ternary sample (Z26), above room temperature photoluminescence was obtained from this sample up to 335 K, see Figure 5.14.

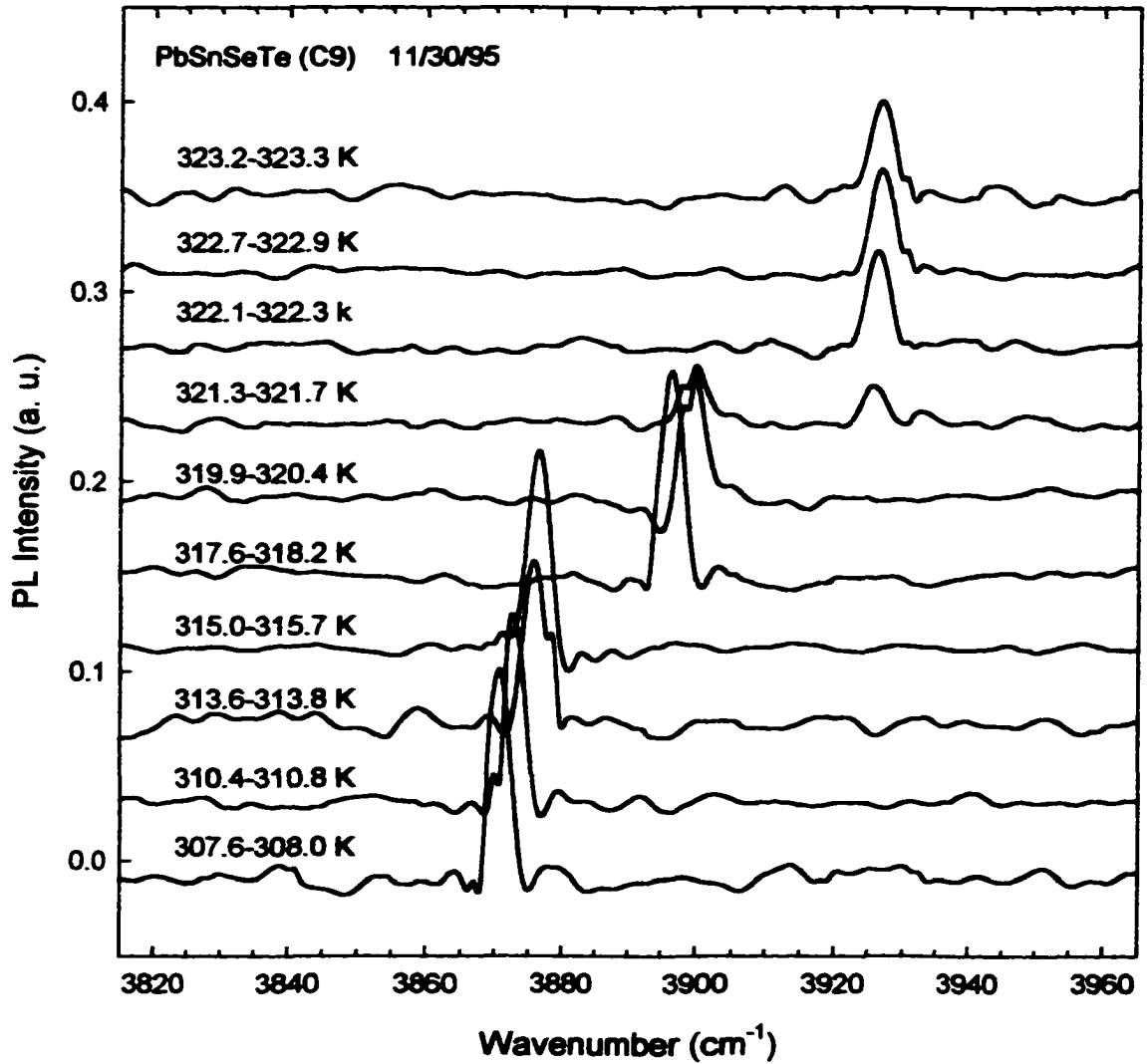


Figure 5.14 (a)

Figure 5.14 Room to high temperature PL spectra of PbSnSeTe (C9, [Sn]=40%) in four parts (this page and the next three pages). In parts (a), (b), and (c) the PL peaks below 3950 cm⁻¹ are real. A complex feature around 3950 cm⁻¹ comprised of the real and the alias PL peaks is observed in some spectra of parts (c) and (d), similar to what's previously seen in Figure 5.9. The top two spectra in part (d) show the real PL peaks around 3960 cm⁻¹.

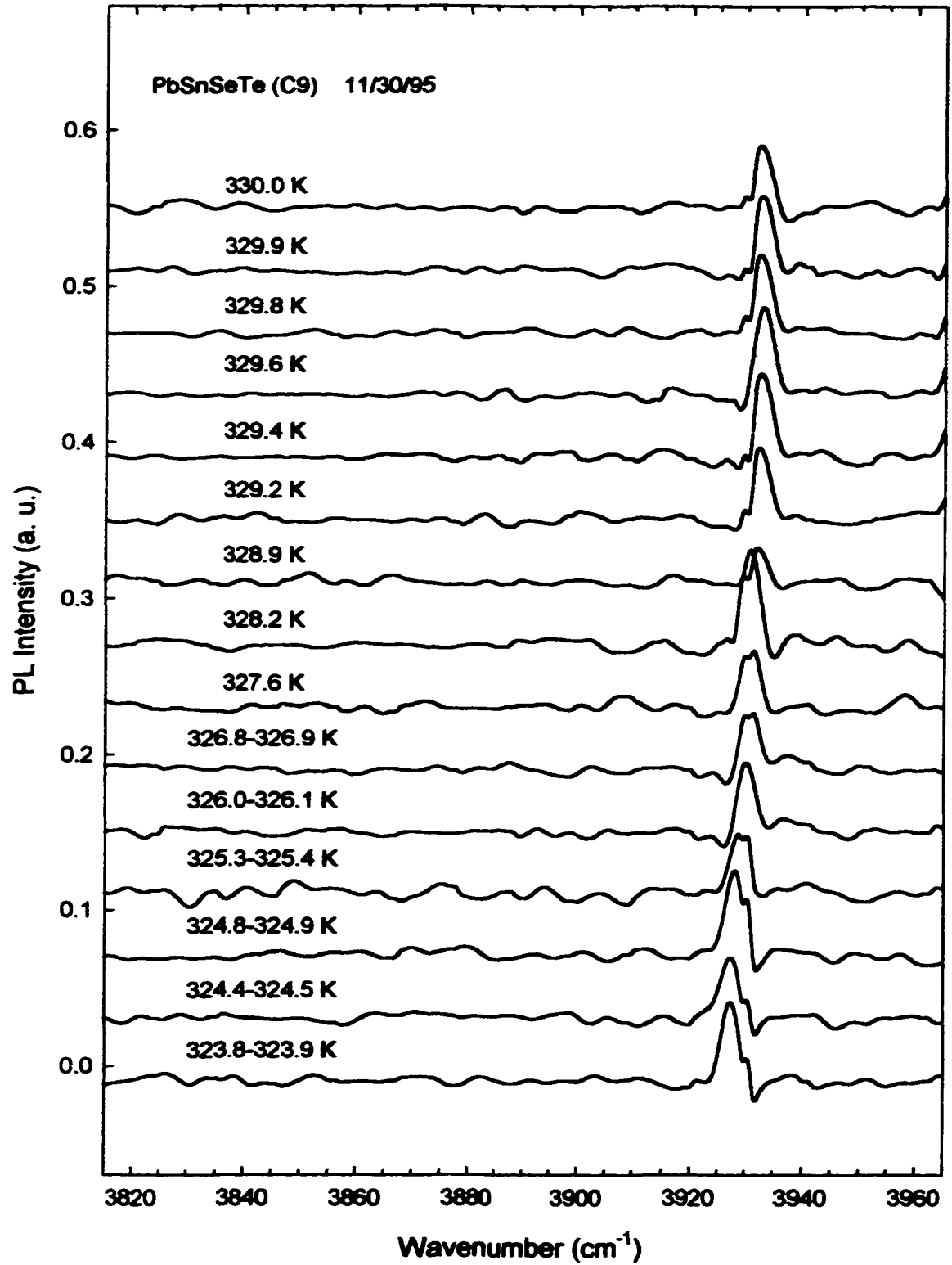


Figure 5.14 (b)

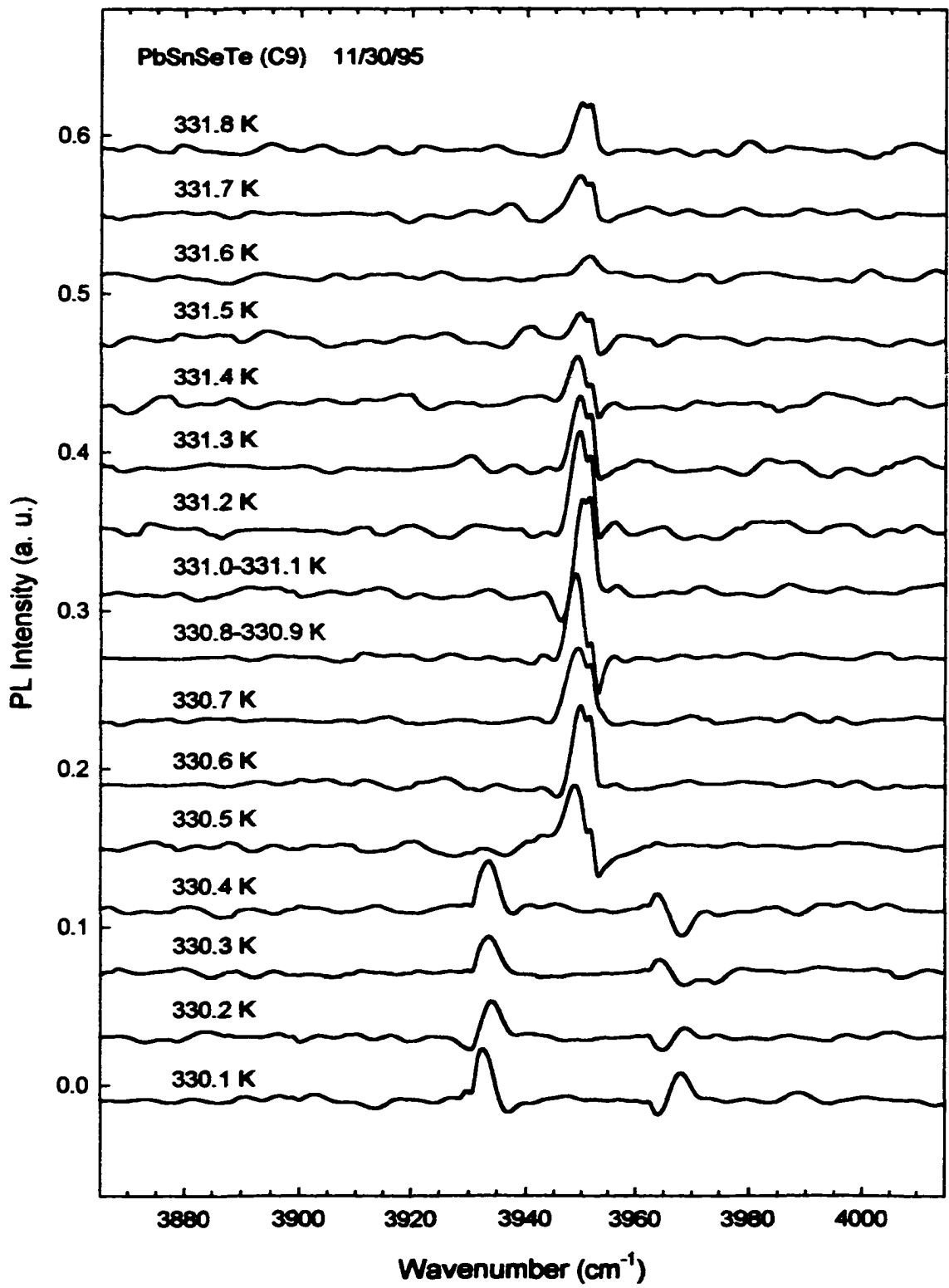


Figure 5.14 (c)

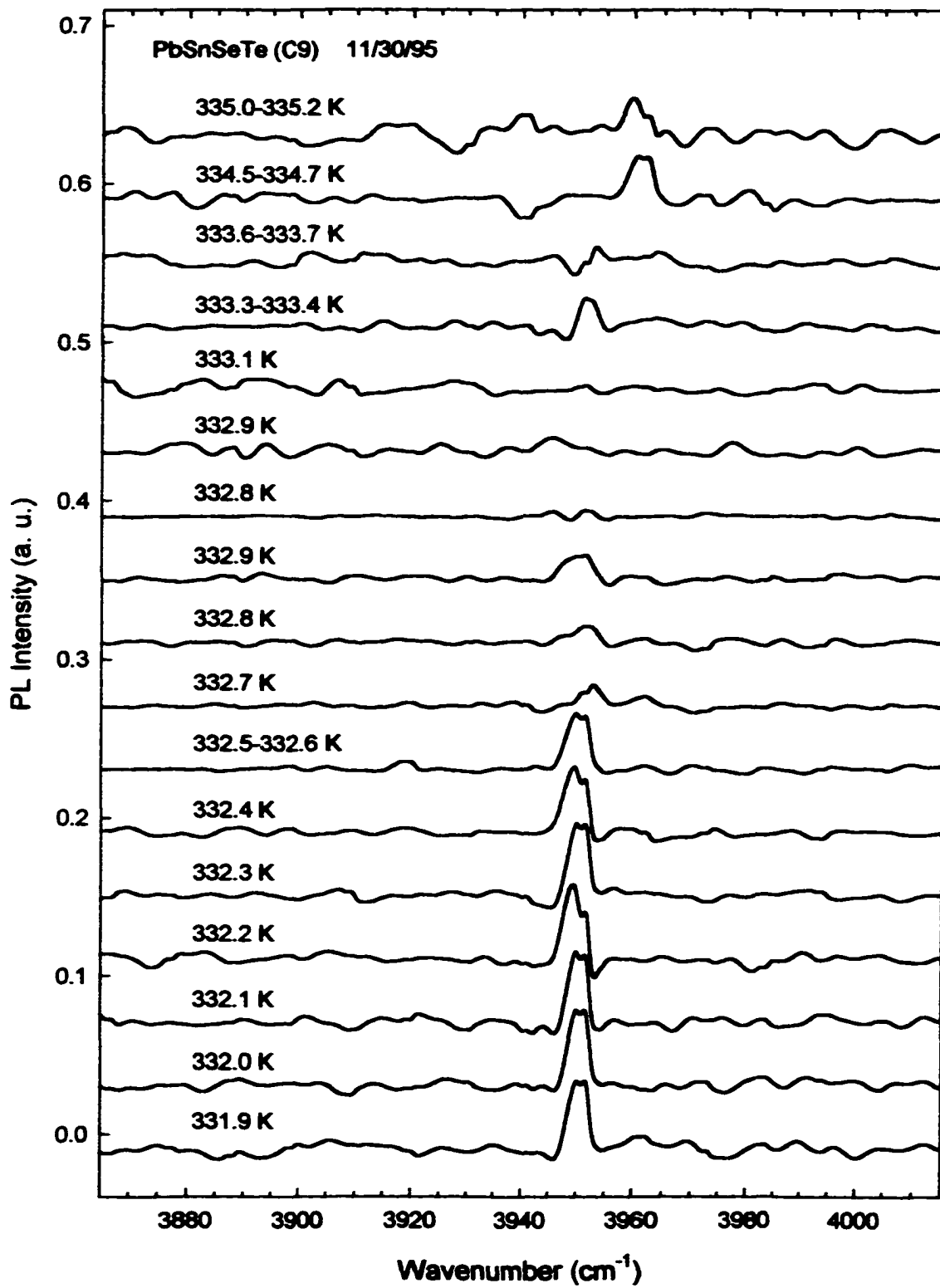


Figure 5.14 (d)

The peak PL energies obtained from the above spectral data are plotted as a function of temperature and shown in Figure 5.15. The “hopping” of PL energy is more pronounced for this sample than for sample Z26.

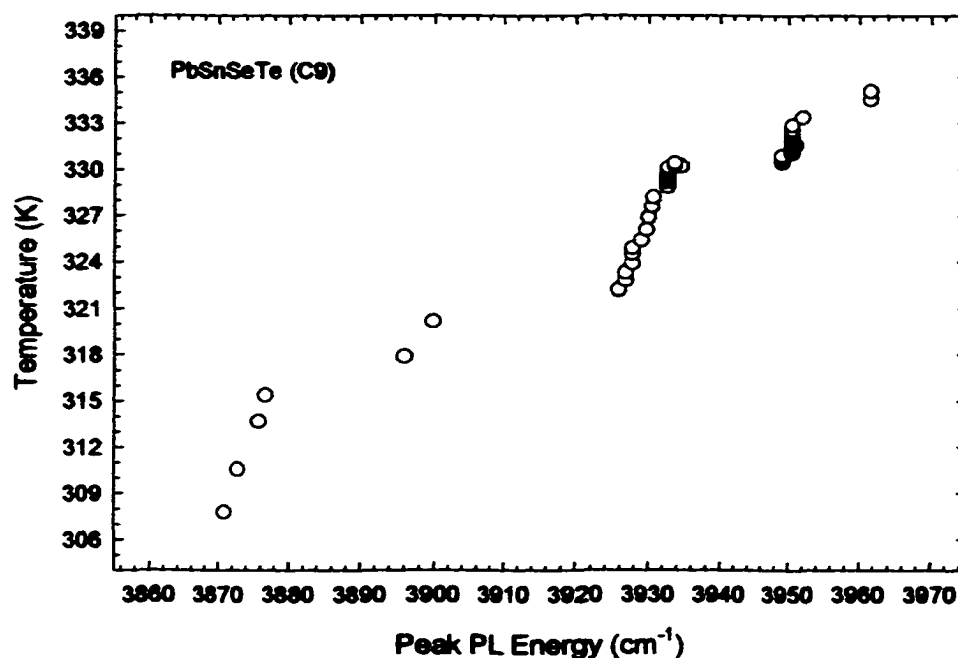


Figure 5.15 Peak PL energy as a function of temperature, obtained from a PbSnSeTe epilayer with 40% tin content.

All intrinsic *n*-type IV-VI epilayers mentioned in this study exhibited photoluminescence. PL experiments were performed at 305 K on a PbSeTe sample doped with thallium impurities (C42 with 3% Tl) right after testing samples S37 and S43 (whose PL spectra are shown in Figure 5.13). Although the experimental conditions were the same, no luminescence was observed from this *p*-type layer. Photoluminescence experiments were also attempted at room temperature using a custom designed sample holder allowing the laser beam to be incident on a 60° angle (relative to the normal line). The well-tested samples Z26 and C9, while exhibiting luminescence using the 45° apparatus, ceased to produce the expected PL peaks with

the 60° apparatus. This result suggests that the experimental geometry may be important.

Control studies were carried out during the photoluminescence characterization of these LPE-grown IV-VI epilayers, in which “dummy samples” were tested under the same experimental conditions. These samples includes a mirror, a (100) BaF₂ substrate used for the growth of the LPE layers, a silicon substrate, and a solidified melt of the residual LPE growth solution. None of these samples produced any identifiable features in their PL spectra.

It is unlikely that the observed PL is artificially generated by the experimental system. In a previous low temperature PL study of an *n*-PbSe_{0.78}Te_{0.22} sample [3], a broad feature with center energy above the familiar band-to-band transition was observed, see Figure 5.16. The PL spectrum was obtained from a different experimental system using a dispersive type spectrometer and the 514 nm (2.41 eV) emission line of an Argon laser as the pump source operated at 12 mW.

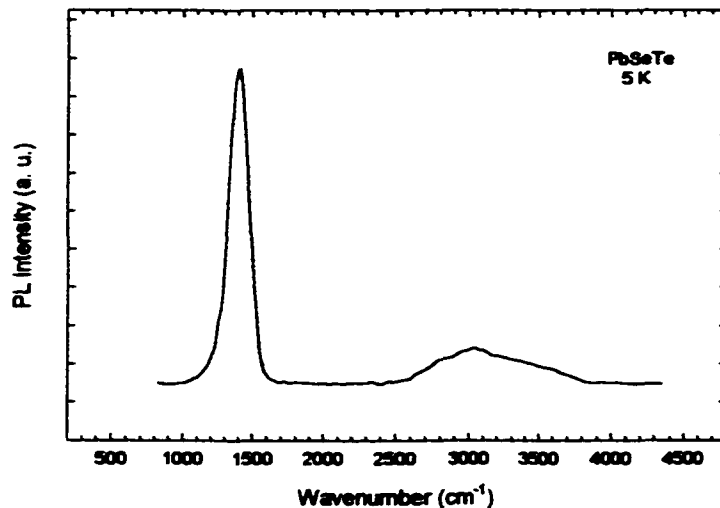


Figure 5.16 PL spectrum for an *n*-PbSe_{0.78}Te_{0.22} layer grown by LPE [3]. The sharp peak (FWHM 176 cm⁻¹) at 1404 cm⁻¹ (174 meV) is the band-to-band transition. The broad feature centered at 1404 cm⁻¹ (374 meV) was thought to be associated with the predicted group VI vacancy defect states [40].

5.4 Summary of Experimental Results

The characteristic and common features observed on all PL spectra obtained from different IV-VI samples (PbSe, PbTe, PbSeTe, PbSnSeTe, [Sn]=5% and 40%) are summarized below:

1. PL energy is strongly temperature dependent and increases with temperature like the band-to-band PL energy.
2. PL energy is insensitive to alloy composition, i.e., metal and chalcogen exchange. (PL energy at a given temperature shows no appreciable difference among different samples.)
3. PL energy exhibits very narrow linewidth ($\sim 5 \text{ cm}^{-1}$), much more narrower than that of the band-to-band PL. The actual linewidth can be less than 5 cm^{-1} due to the 4 cm^{-1} resolution of the FTIR spectrometer.
4. PL linewidth is insensitive to alloy composition, i.e., metal and chalcogen exchange. (The “apparent” linewidth shows no appreciable difference among different samples.)
5. There is no observable thermal broadening of the PL linewidth as seen for band-to-band transitions.
6. PL has a single peak at room temperature and above room temperatures.
7. PL energy is an intrinsic property of the IV-VI crystals (samples are as grown, native *n*-type, not doped, and not altered in any way).

Additional PL features for the PbSeTe sample (Z26) are:

1. PL spectra show a single luminescence peak in the measurement range of 273-342 K and multiple peaks at 81 K.
2. At 81 K PL energy and intensity increase monotonically with irradiation power of the pump laser.
3. At 81 K two features are present initially at lower optical pump power. These two features begin to separate more with increasing optical pump

power, while the higher energy PL feature becomes more resolved and splits into two peaks (10 cm^{-1} separation between the two peaks at 220 mA pump laser driving current compared to 6 cm^{-1} at 200 mA).

Some characteristic PL spectra of PbSeTe are grouped together and shown in Figure 5.17. In this figure PL spectra of $\text{PbSe}_{0.78}\text{Te}_{0.22}$ (sample Z26) are superimposed

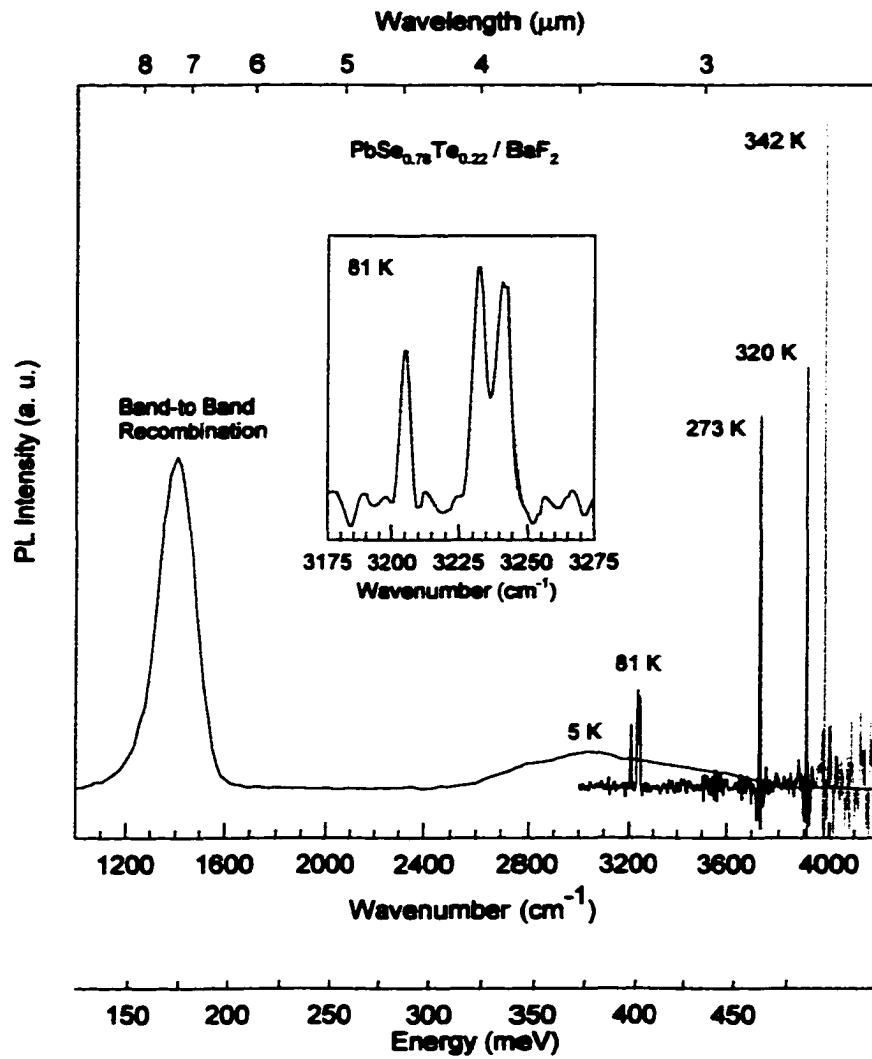


Figure 5.17 Spectra of photoluminescence from two different $\text{PbSe}_{0.78}\text{Te}_{0.22}$ epilayers. Characteristics PL spectra of PbSeTe in the temperature range of 81K to 342 K are superimposed on the 5K spectrum, previously seen in Figure 5.16 [3]. The 5K spectrum was obtained from a dispersive type spectrometer while the spectra at higher temperatures were obtained from an interferometric type spectrometer. The insert is a blowup of the 81 K spectrum.

on the 5 K PL spectrum of a similar sample seen in Figure 5.16 [3]. Notice the close proximity of the 5K and the 81 K spectra features. Also notice the much smaller PL linewidth (at higher temperatures) than that of the band-to-band transition.

The PL energies of sample Z26 (PbSeTe) measured at temperatures from 81 K to 342 K, together with PL at 5 K [3] are listed in Table 5.2. The values are taken as the wavenumbers at the peak luminescence intensity from spectra shown in Figures 5.5, 5.8, 5.9, and 5.16. All data for sample Z26 were collected with the GaAlAs pump laser operating at 120 mA and under similar experimental conditions.

Table 5.2 Photoluminescence energies of PbSeTe from 5 K to 342 K.

Temperature (K)	Wavenumber (cm^{-1})	Energy (meV)	Temperature (K)	Wavenumber (cm^{-1})	Energy (meV)
5	3020	374	330.7	3930.71	487.32
81.0	3159.23	391.67	330.8	3930.71	487.32
81.0	3178.51	394.06	330.9	3931.00	487.35
273.5	3728.20	462.21	331.0	3931.68	487.44
279.7	3751.34	465.08	331.1	3933.61	487.68
284.9	3766.77	466.99	331.5	3938.43	488.28
289.9	3785.09	469.27	331.8	3938.43	488.28
295.0	3808.24	472.13	332.0	3938.43	488.28
305.2	3834.28	475.36	332.2	3938.43	488.28
310.0	3868.99	479.67	332.5	3937.46	488.16
314.5	3872.85	480.15	332.8	3940.00	488.47
320.1	3907.57	484.45	333.0	3940.00	488.47
330.3	3929.75	487.20	333.2	3940.00	488.47
330.6	3929.75	487.20	333.4	3940.00	488.47

Temperature (K)	Wavenumber (cm ⁻¹)	Energy (meV)	Temperature (K)	Wavenumber (cm ⁻¹)	Energy (meV)
333.6	3940.00	488.47	337.0	3952.89	490.07
333.8	3940.30	488.51	337.4	3953.86	490.19
334.1	3940.30	488.51	338.4	3959.64	490.91
334.3	3940.30	488.51	338.6	3963.00	491.32
334.6	3940.30	488.51	338.8	3963.00	491.32
334.8	3940.30	488.51	339.1	3965.43	491.62
335.0	3940.30	488.51	339.3	3965.50	491.63
335.1	3940.36	488.51	339.8	3968.32	491.98
336.3	3951.93	489.95	340.3	3974.11	492.70
336.5	3952.30	490.00	340.5	3976.04	492.94
336.6	3952.50	490.02	342.0	3977.00	493.06
336.7	3953.5	490.14			

Figure 5.18 is a plot of PL energy vs. temperature, together with the plot of absorption edges obtained from FTIR absorption spectroscopy [3]. All PL data points in the PL plot are from Table 5.2. The PL energy varies with temperature at an approximate rate of 0.4 meV/K, comparable with the tuning rate of the absorption edge energy at temperatures above 200 K.

With the 40 mW (120 mA) pump laser beam focused, the laser power density irradiating an area of $\sim 1 \text{ mm}^2$ is about $\sim 4 \text{ W/cm}^2$. The temperature of the irradiated region cannot be tracked precisely by the temperature sensor due to the poor thermal conductivity of the IV-VI material and the BaF₂ substrate. The degree of the local heating can be derived by coupling the laser current vs. PL energy plot in Figure 5.6

with the temperature vs. PL energy plot in Figure 5.18, as seen in Figure 5.19. Based on this graphical method, a thirteen-degree increase in local sample temperature is brought about due to an 80-mA increase in laser current.

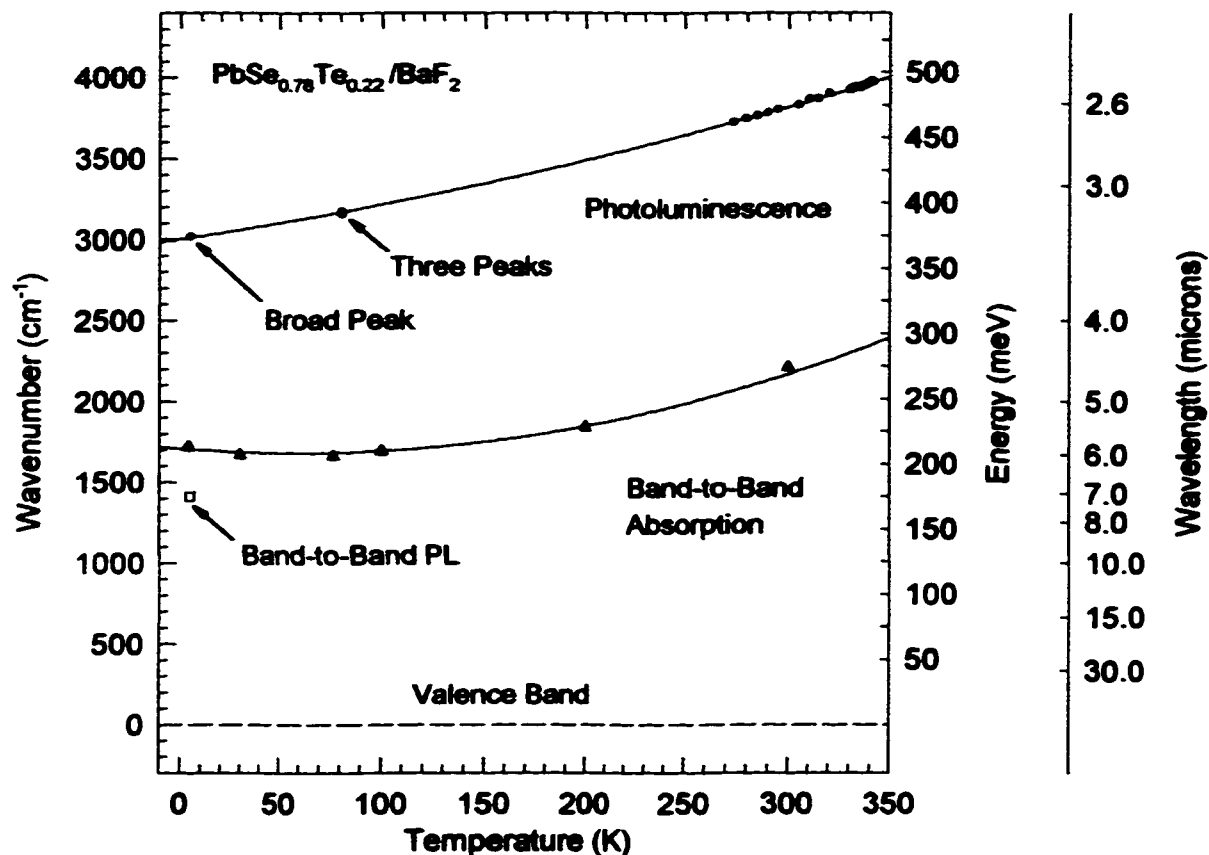


Figure 5.18 Photoluminescence energy vs. temperature plots of a PbSeTe sample (Z26) at all measurement temperatures except 5 K (obtained from another PbSeTe sample, see Figure 5.16)). The band-to-band absorption curve is obtained by FTIR transmission measurements from the same sample that exhibits the 5 K PL [3]. Three PL peaks were observed at 81 K (see Figure 5.7 when pump diode laser was operated at 220 mA. The gap between the band-to-band absorption energy and the band-to-band PL energy at 5 K is due to Burstein-Moss shift.

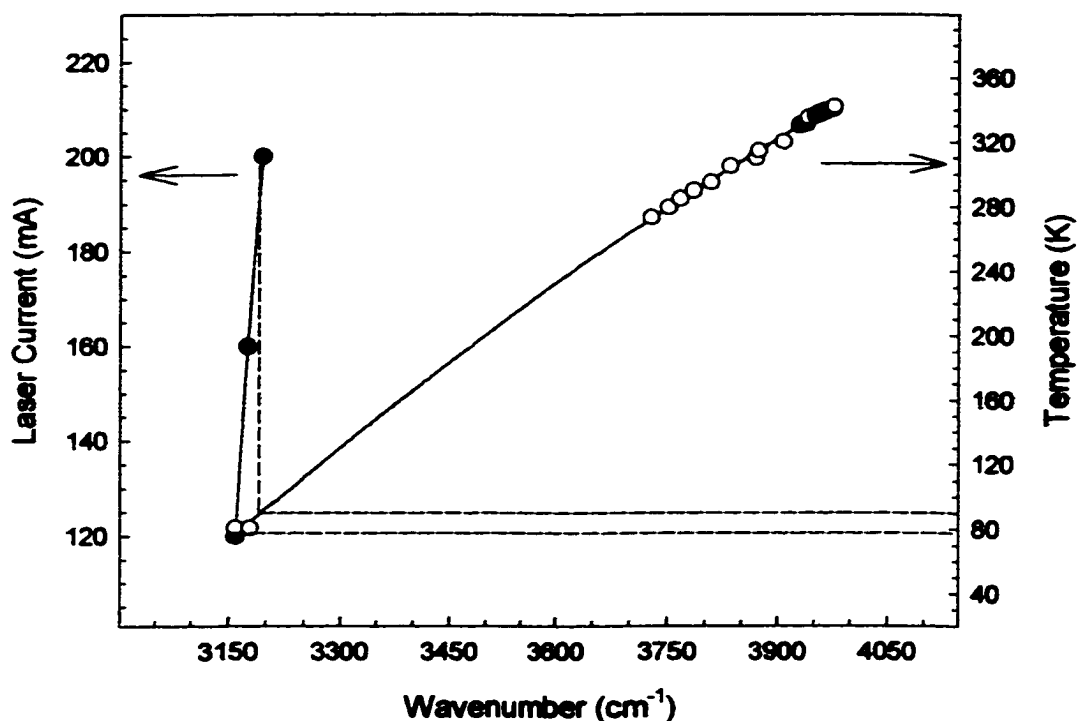


Figure 5.19 Degrees of local heating in the irradiated region of the sample caused by the laser beam. The solid circles pertain to current vs. wavenumber plot while the hollow circles pertain to temperature vs. wavenumber plot. The vertical dotted line represents the projection of the former plot onto the later. The horizontal dotted lines from the intercepts indicate the increase in sample temperature due to the increase in laser current.

5.5 Discussions

Having made these observations, one begins by investigating the crystal behavior at different temperatures. For heteroepitaxial growth a pertinent question to ask is: How does the measurement temperature affect different constituents of the sample? The IV-VI semiconductor layers were grown on (100) BaF₂ substrates having the same rock salt crystal structure and comparable thermal expansion coefficients at and above room temperature. As sample temperature is reduced, however, the coefficient becomes larger for IV-VI crystals than for the BaF₂ crystal. Thus when the

sample is cooled to liquid nitrogen temperature the IV-VI layers acquire an in-plane tensile strain (the IV-VI material wants to shrink faster than the BaF₂ material). The multiple-peaks on the 81-82 K PL spectra (Figures 5.4, 5.5, and 5.7) are consistent with crystal field splitting of degenerate electronic states in biaxially strained material. If at low temperatures the crystal field produced by the biaxial strain were coplanar with the in-plane components of the degenerate electronic states, then only two peaks would split out. In reality, however, this may not be the case due to the fact that the BaF₂ substrate and the IV-VI layers are not truly (100) oriented. Consequently the degeneracy of the in-plane components of the electronic states can also be lifted. This is evident by the splitting of the high energy PL feature.

The high energy PL feature becomes more resolved with increased optical pump power and becomes totally resolved at 220 mA (Figures 5.5 and 5.7). This behavior cannot be accounted for by the above explanations only. One must also consider the effect of the local heating of the sample by the pump laser power in addition to the global effect of sample heat sink temperature. Figure 5.19 shows that there is a 13-degree local heating in the sample corresponding to a 80-mA increase of laser driving current. This local heating enhances the effect of the crystal field, thus splits off the higher energy PL peak when the laser current is increased.

Since the resolution of the FTIR spectrometer is 4 cm⁻¹ the actual linewidth of the luminescence can be much smaller than the observed 5 cm⁻¹. The band-to-band PL spectrum of a PbSeTe epilayer, see Figure 5.16, has a linewidth of approximately 160 cm⁻¹ (~ 20 meV) measured at 5 K. The linewidth of PL due to intersubband transitions in a PbSe two-dimensional layer is approximately 36 cm⁻¹ (~ 5 meV) obtained at 10 K [68]. The narrow linewidth, together with the apparent lack of thermal broadening over a wide range of temperatures (81 to 342 K) are atypical of band-to-band transitions in semiconductors. Rather, these observations are more consistent with the type of transitions associated with discrete, localized electronic states such as atomic states.

The energies of the luminescence (~390 meV at 81 K, ~470 meV at 300K, see Table 5.2) are far greater than the narrow bandgap of the IV-VI alloys. A likely theoretical model that can account for the observed luminescence energies of these IV-VI semiconductors is the Parada-Pratt Model [40]. The construct of the Model is described below.

In the fcc crystal structure of PbTe a Te atom is surrounded by six neighboring Pb atoms. The valence band of PbTe is comprised of Pb-s, Te-s, and Te-p bands and the conduction band is formed by the Pb-p bands. A Te vacancy creates a localized vacancy potential that weakly perturbs the Pb-s states while strongly perturbs the Te states (2 *s* orbitals and 6 *p* orbitals). The perturbation lifts these eight states from the valence band to the conduction band while only six valence electrons ($5s^2p^4$) are actually lost. Thus two electrons from the valence band of the surrounding Pb atoms get promoted into the conduction band. A schematic of the predicted defect energy levels associated with Te vacancies in *n*-PbTe according to the Parada-Pratt Model is shown in Figure 5.1. The energy unit in Ryberg in the original band diagram is quoted, which is also converted to the unit of meV. The Figure shows that the predicted group VI vacancy states are at least ~160 meV above the bottom of the conduction band edge.

The predicted defect states are similar to the F centers associated with anion vacancies in alkali halide crystals such as sodium chloride. The difference is that the former is said to be resonant with the conduction band states while the latter lies within the bandgap. This is reasonable considering that the force between the electron and the attractive part of the Te vacancy potential is not as strong as that of Cl vacancy potential (NaCl is much more ionic than PbTe). Furthermore, screening due to the large dielectric constant of PbTe serves to reduce this Coulombic force.

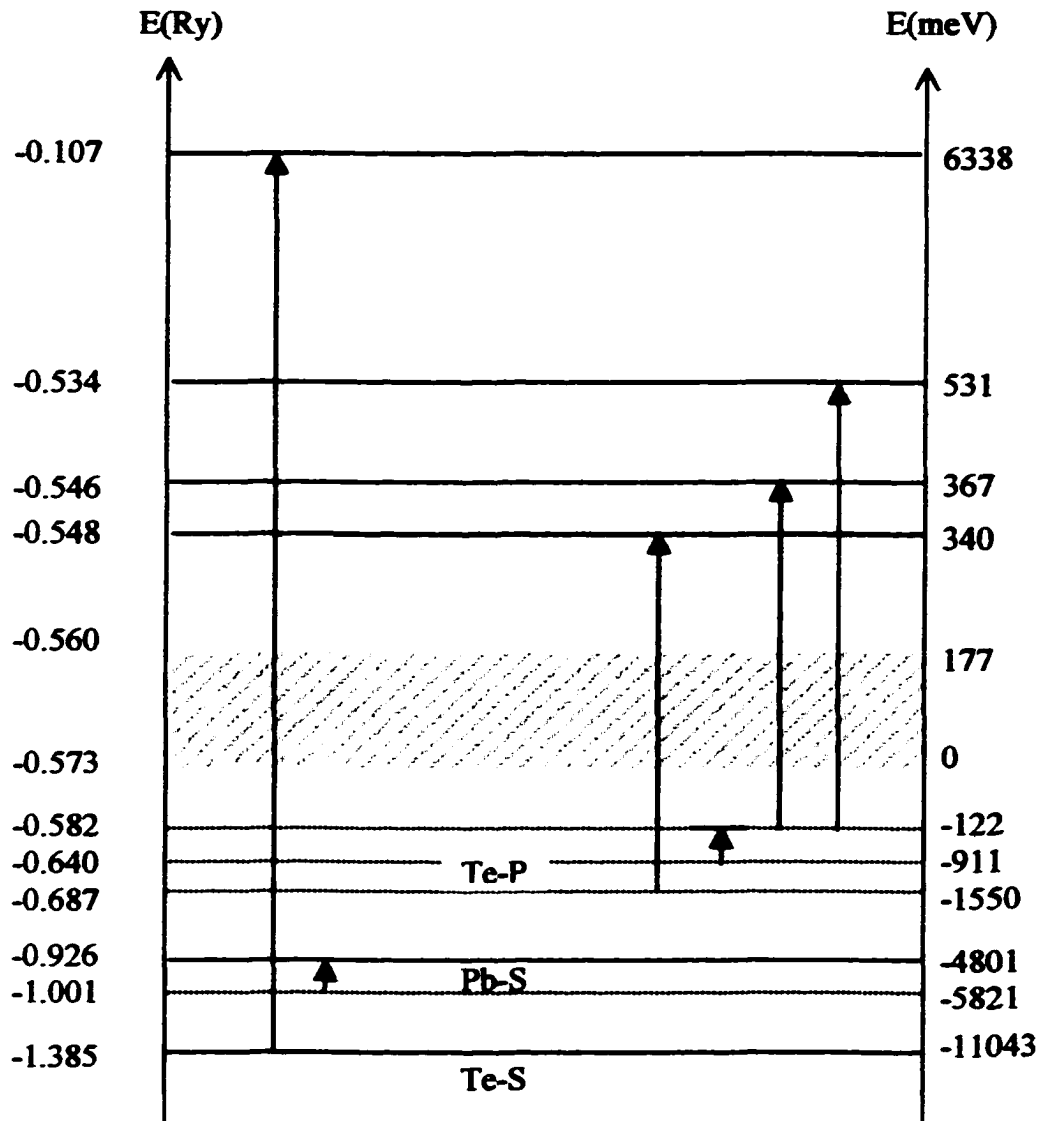


Figure 5.1 Schematic of the Parada-Pratt Model [40] showing states associated with Te vacancies in n -PbTe at the L point of the Brillouin zone. The crosshatched area represents the forbidden band. The arrows represent the lifting of valence band states (dotted line) to new levels (solid line).

According to the Parada-Pratt Model the defect states for n -PbTe have p -like orbitals and occupy energy levels that are greater than 340 meV above the valence band maximum. It is known that in the presence of spin-orbit interaction the six-fold

degenerate p states split into a four-fold degenerate $p_{3/2}$ level and a two-fold degenerate $p_{1/2}$ level. The predicted defect state energy and the p-like character are in line with the observed PL energy, its narrow linewidth, and its splitting. In addition, the concept of group VI “vacancy potential” is not inconsistent with the observed insensitivity of PL energy with group VI atom exchange. The Model, however, is short of explaining the observed insensitivity of PL linewidth to temperature from 81 K to 342 K, and the broad PL feature at 5 K [3]. A conjecture for the observed PL mechanism is: hot electrons that are optically excited into the higher conduction band states undergo rapid thermal relaxation to the defect states having relatively long lifetime before radiatively recombining with holes in the valence band.

In a many-electron frame of work [63], the authors found that the electron-electron interaction modifies greatly the Parada-Pratt Model and essentially determines the positions of the vacancy levels found experimentally. The proposed defect states were said to transform in accordance with irreducible representations of the O_h group: A_{1g} (singlet), E_g (doublet), and F_{1u} (triplet). The authors also suggested that if the splitting of the initial six-fold, quasi-degenerate level by electron-electron interaction is not too strong, the Jahn-Teller effect might be stronger. This effect can lift the degeneracy because of asymmetric distortion of the crystal environment of a defect.

The insensitivity of defect state energy to alloy composition has been reported [64, 65]. Damage induced defect levels in $PbSe_xTe_{1-x}$ samples ($0 \leq x \leq 1$) were derived from conductivity and Hall-effect measurements at low and high temperatures [64]. The results suggest that the levels were strongly temperature dependent but insensitive to anion exchange. Data extracted from absorption measurements of intrinsic p - $Pb_{1-x}Sn_xSe$ samples suggest a defect state energy level that lies ~ 205 meV below the valence band maximum. This level does not change appreciably in the range $0.01 \leq x \leq 0.06$. These works imply that the Fermi level of the IV-VI semiconductors is pinned by

the vacancy potential, which is not contradictive to the observe “pinning” of PL energy despite the anion and cation exchange.

CHAPTER 6

Emission Studies of Commercial IV-VI lasers

IV-VI semiconductor mid-infrared diode lasers manufactured by RMT Ltd., Moscow, Russia were characterized using an Oriel MIR 8000 Modular IR Fourier Spectrometer. The spectrometer is comprised of an interferometer module, a source module, a detector module, and a microcomputer. The source and the detector modules are externally coupled to the interferometer module, thus allowing maximum flexibility in experimental designs. For emission studies, home-made laser cryostats have been constructed at the OU Solid State Electronics Laboratory and used as the source modules. All spectral measurements in this work were made under open-path, non-purged conditions. Figure 6.1 shows the experimental setup of the emission studies.

The diode laser was mounted on a copper heat sink, which was housed inside a custom designed cryostat equipped with CaF₂ windows. The laser emission was collimated by an off-axis-parabolic mirror (OAPM) before exiting the cryostat. The cryostat was kept under vacuum at $\sim 10^{-6}$ Torr using a turbo pump and then cooled to the liquid nitrogen temperature using a closed-cycle Cryotiger compressor manufactured by APD Cryogenics Inc. A LakeShore 330 Autotuning temperature controller equipped with a silicon temperature sensor was used to set the laser heat sink temperatures to above the liquid nitrogen temperature. An ILX Lightwave LDC-3900 modular laser diode controller provided laser driving current.

The laser beam was optically coupled to the interferometer module that contains a linear scanning Michelson interferometer equipped with a KBr beamsplitter with a

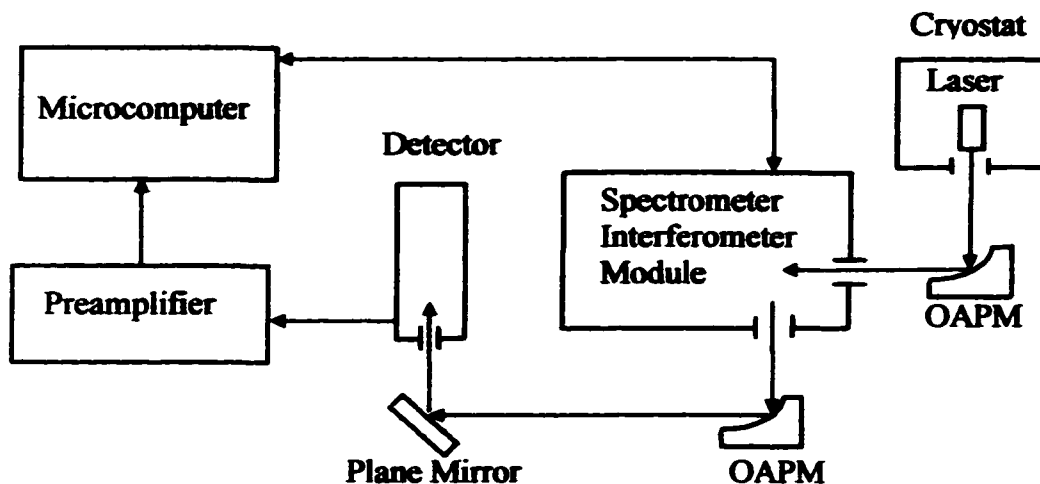


Figure 6.1 Schematic of experimental setup for emission measurement using a modular FTIR spectrometer. Externally mounted off-axis parabola mirrors (OAPM) and a plane mirror were used to collimate and align the laser beam.

spectral coverage from 350 cm^{-1} to $6,000\text{ cm}^{-1}$. The infrared radiation from the laser is modulated at its own characteristic Fourier frequency. The beam exiting the interferometer module was again optically coupled to a liquid nitrogen cooled MCT detector biased at 40 mA using a Keithley 220 programmable current source. The electrical signal from the detector was sent to a microcomputer via a Stanford Research System Model SR 560 low-noise preamplifier. Inside the microcomputer an electronic analog-to-digital conversion board communicates with the interferometer module to perform scan control and data acquisition.

Test parameters such as spectral range, number of scans, and resolution were chosen using the manufacturer provided software. All emission measurements were taken with five scans per test run at 0.5 cm^{-1} spectral resolution (the highest achievable resolution of the spectrometer). As the laser heat sink temperature varied, a sufficient

spectral measurement bandwidth was chosen to reflect all lasing modes at that temperature. Since the output power of the laser is much higher than the room-temperature blackbody radiation, there is no need to subtract the background spectrum from the emission spectrum.

The lasers are Fabry-Perot type resonant devices fabricated from $\text{Pb}_{1-x}\text{Eu}_x\text{Se}$ double heterostructures grown on PbSe substrates by molecular beam epitaxy. Several such lasers were characterized and test results of the best device (#42) are presented in this chapter. According to the manufacturer's data sheet, this continuous wave (CW) device has emission ranging from 1792 cm^{-1} at 78 K to 1980 cm^{-1} at 115 K. The maximum values of the operating temperature, the driving current, and power are specified at 120 K, 1200 mA, and $300\text{ }\mu\text{W}$ (78 K), respectively.

Since the lowest temperature obtainable with the cryogenic refrigerator is 89 K, testing was initiated at 90 K. Once a stable temperature was established, the driving current was gradually increased from a level much below the anticipated threshold until threshold lasing was observed on the spectral display. Current beyond the threshold level was then increased in 20-mA increments and above-threshold lasing spectra were recorded. A total of 491 spectral data files were collected for operating temperatures from 90 K to 116 K. Spectral plots of these data files are shown in Appendix E. The analysis of these spectra shows single continuous modes, and mode hops characteristic of Fabry-Perot resonant cavities. Multiple-mode emissions, which are consistent with the wide gain spectrum of semiconductor lasers, were observed at the transition of some of the mode hops. The stable, single-mode spectral regions with their corresponding current levels and operating temperatures are listed in Table 6.1.

Table 6.1 Listing of single stable mode of TDL #42 per current ramp and operating temperature. The highest injection current level is 1010 mA.

Temperature (K)	Current (mA)	Emission Wavenumber (cm⁻¹)
90	370 - 590	1847.9663 - 1851.3416
	610 - 730	1856.4044 - 1858.3331
91	390 - 470	1849.5282 - 1850.7336
	490 - 650	1857.2430 - 1859.8950
92	410 - 570	1857.2955 - 1859.9475
93	430 - 470	1858.7421 - 1859.4653
94	430 - 470	1866.1530 - 1866.8762
	550 - 570	1868.0817 - 1868.3228
95	450 - 470	1867.5366 - 1867.7777
	490 - 670	1874.5282 - 1877.4213
96	570 - 590	1877.1173 - 1877.3584
	610 - 730	1883.8678 - 1886.0376
97	450 - 490	1876.0272 - 1876.7505
	510 - 650	1883.5010 - 1885.6708
	670 - 810	1892.1802 - 1894.8322
98	450 - 550	1883.6163 - 1885.3040
	570 - 750	1892.0544 - 1894.9475
	790 - 850	1901.9391 - 1903.1445
99	490 - 690	1891.8134 - 1894.9475
	710 - 790	1901.6980 - 1903.1445
100	470 - 590	1892.4109 - 1894.3396
	610 - 730	1901.0901 - 1903.0188
	770 - 790	1908.5638 - 1908.8049
	810 - 850	1910.7336 - 1911.4569
	870 - 890	1913.3856 - 1913.8678
	910 - 1010	1918.9307 - 1920.6183
101	450 - 470	1893.1342 - 1893.6163
	510 - 650	1900.6079 - 1903.0188
	690 - 770	1908.3228 - 1911.4569
	810 - 930	1918.4485 - 1920.6183
	950 -	1927.1277 -
102	490 - 570	1901.2683 - 1902.7148
	610 - 650	1908.0188 - 1908.7421
	670 - 690	1910.6708 - 1911.1530
	730 - 870	1918.1445 - 1920.5554
	890 -	1927.3059 -
103	490 - 630	1908.9203 - 1911.3312
	650 -	1918.0817 -

104	510 - 530	1910.3040 - 1910.7861
	590 - 710	1917.7777 - 1920.1886
	730 -	1926.9391 -
105	510 - 630	1917.7148 - 1919.8846
	650 -	1926.6351 -
106	530 - 550	1919.4025 - 1919.6436
	570 - 670	1926.3940 - 1928.0817
	710 - 830	1935.0732 - 1937.2430
	850 - 970	1943.9935 - 1946.1530
	990 - 1010	1953.1445 - 1953.3856
107	510 - 610	1926.5094 - 1928.1970
	630 - 770	1934.9475 - 1937.5995
	790 - 930	1944.1089 - 1946.7609
	950 - 1010	1953.5114 - 1954.7168
108	550 - 690	1934.7064 - 1937.1173
	710 - 850	1943.8678 - 1946.5198
	870 - 1010	1953.2703 - 1955.7965
109	530 - 610	1935.5450 - 1936.7505
	630 - 750	1943.5010 - 1945.9119
	770 - 910	1952.6624 - 1955.3143
	930 -	1962.0648 -
110	550 - 670	1943.6163 - 1945.5450
	690 - 810	1952.2955 - 1954.7064
	830 - 990	1961.4569 - 1964.5911
111	570 - 590	1945.0629 - 1945.3040
	610 - 730	1952.0544 - 1954.4653
	750 - 950	1960.9747 - 1965.0732
112	570 - 650	1952.4738 - 1953.9203
	690 - 870	1961.1530 - 1964.5282
	930 - 970	1970.5554 - 1971.2787
113	610 - 810	1960.5450 - 1964.4025
	950 - 990	1978.3856 - 1979.1089
114	610 - 730	1961.7505 - 1964.1614
	750 - 870	1970.9119 - 1973.0817
	890 - 990	1978.3856 - 1980.3143
115	610 - 630	1962.9559 - 1963.1970
	650 - 810	1970.1886 - 1973.0817
	830 - 930	1978.3856 - 1980.3143
116	610 - 730	1970.5450 - 1972.9559
	770 - 830	1978.2599 - 1979.7064
	910 - 950	1987.6624 - 1988.6267

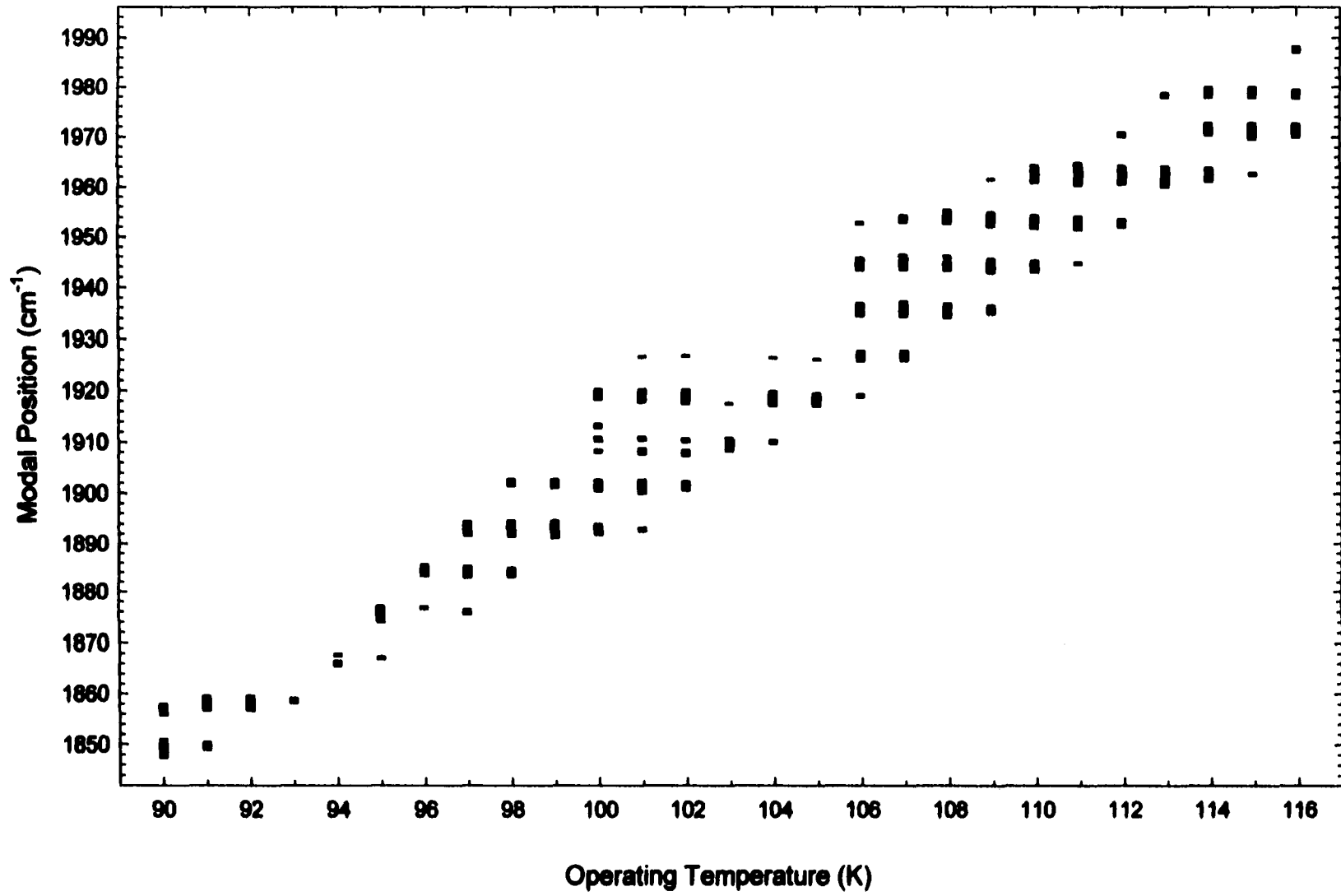


Figure 6.2 Modal distribution of tunable diode laser #42 as functions of operating temperature and driving current.

There are many spectral regions in which the laser exhibits stable, single-mode current tuning spanning 2 to 3 cm^{-1} . The largest tuning range observed is 4 cm^{-1} at 111 K with a tuning rate of 0.02 cm^{-1}/mA . Emission from this device spans 140 cm^{-1} from 1848 cm^{-1} (5.411 μm) to 1988 cm^{-1} (5.030 μm). Several gas molecules such as H_2O , N_2O , NO , NH_3 , and COF_2 have absorption features with linestrengths greater than $1 \times 10^{-22} \text{ cm}^{-1}/\text{molecule}\cdot\text{cm}^{-2}$ that fall within this spectral range. The modal distribution listed in Table 6.1 is plot in Figure 6.2, which reflects the complete single-mode tuning characteristics of the device.

Single-mode positions are plotted as a function of operating temperature at several injection current levels. Shown in figure 6.3 is one of these plots at 570 mA, which is typical of the temperature tuning characteristics of the device.

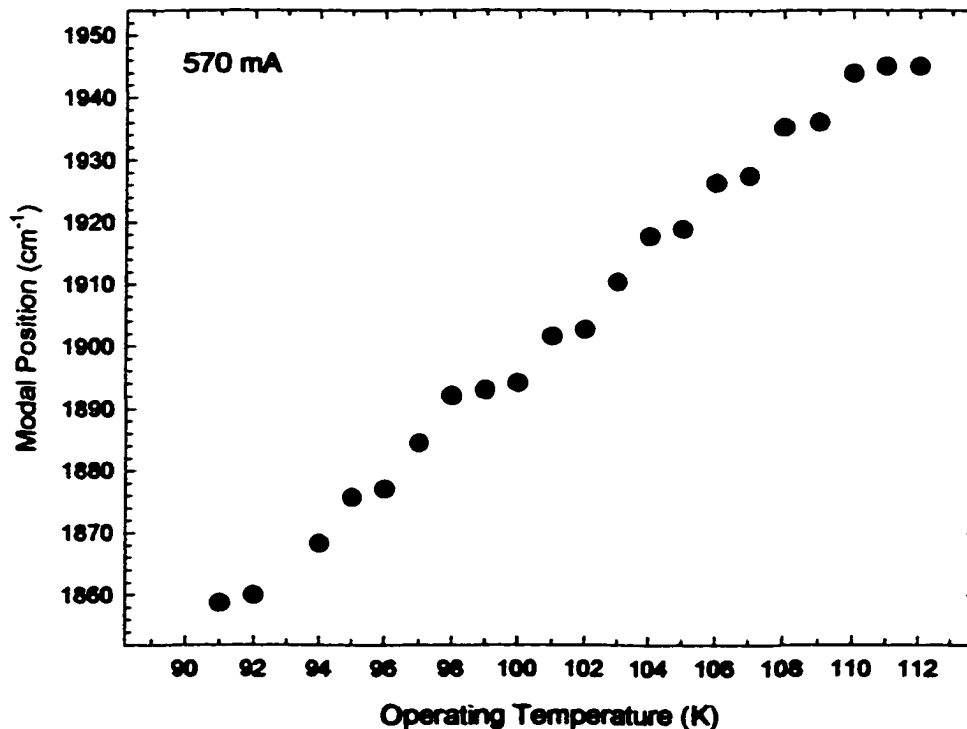


Figure 6.3 Emission frequency tuning curve of tunable diode laser #42 as a function of temperature. The current setting is at 570 mA.

Mode positions are plotted as a function of injection currents at several operating temperatures. Figure 6.4 shows such a plot at five operating temperatures, which is typical of the current tuning characteristics of the device.

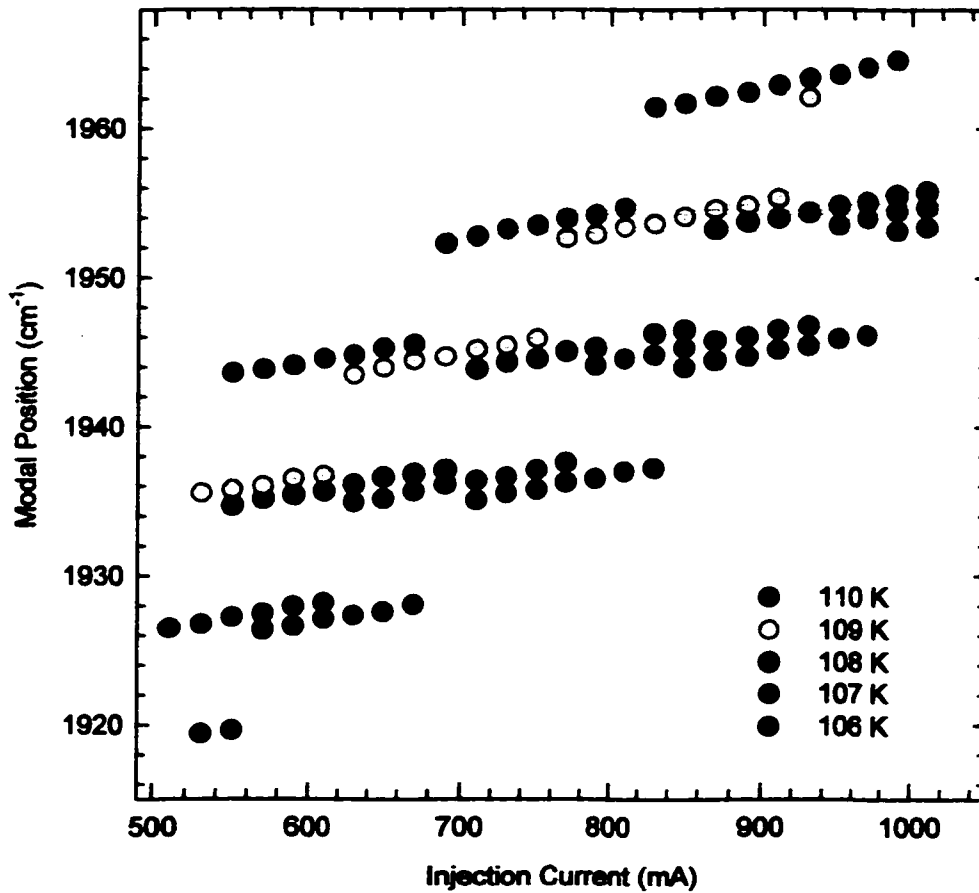


Figure 6.4 Emission frequency tuning curve of tunable diode laser #42 as function of current at five consecutive operating temperature settings.

The wide current and temperature tunability of this device makes it an excellent radiation source for mid-IR tunable diode laser absorption spectroscopy. With a multitude of monomodes spanning 140 cm^{-1} across 27 operating temperatures, this

device should offer much more versatility than the recently developed quantum cascade lasers [8].

Furthermore, it is possible to measure more than one gas species using such a single device at one specified current and temperature setting. For example, species such as H₂O, NO, and COF₂ have absorption features in the spectral regions of 1953–1956 cm⁻¹ (~ 5.12 μm). The result of laser characterization (see Table 6.1) shows that single-mode lasing of device #42 has a tuning range from 1953.2703 cm⁻¹ to 1955.7965 cm⁻¹ at 108 K. The absorption features of the three molecules mentioned above are well within the tuning range of this mode. This is demonstrated in Figure 6.5 (next page).

In fact, the absorption line of H₂O at 1954.9959 cm⁻¹ and the “sawtooth” lines of COF₂ has recently been measured using laser #42 operated around 900 mA and at 108 K by second harmonic detection [62]. With the inherently high resolution of the laser source, the double lines (separated by 0.0057 cm⁻¹) of NO shown in figure 6.5 should be resolvable using the same technique.

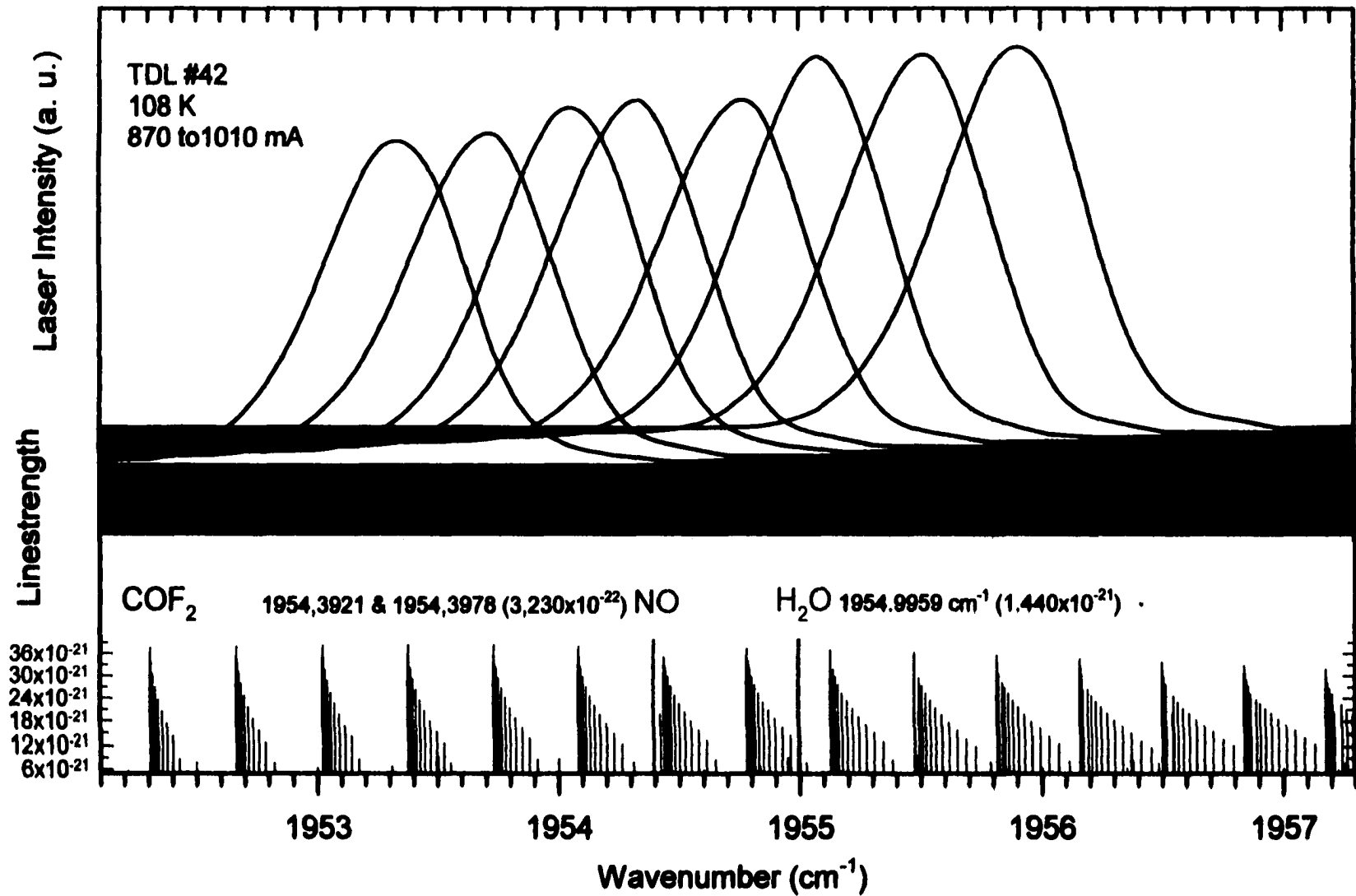


Figure 6.5 Emission spectra of tunable diode laser #42, top, and HITRAN spectra of three gas molecules, bottom. The linestrength for the H₂O and the NO absorption features is not in proportion to that of COF₂ and is indicated in parenthesis.

CHAPTER 7

Summary

IV-VI semiconductor as-grown epilayers and a IV-VI diode laser were characterized by Fourier transform infrared spectroscopy. A vacuum-bench FTIR spectrometer was used to perform transmission and photoluminescence experiments under a low vacuum condition while a modular FTIR spectrometer was used to perform emission experiments under an open-path condition.

The transmission measurements produced transmission spectra for $\text{Pb}_{1-x}\text{Eu}_x\text{Se}$ ($x = 0\%$, 2.44%, 7.32%) and $\text{Pb}_{1-x}\text{Sr}_x\text{Se}$ ($x = 0\%$, 7.83%, 15.7%, 26.1%) layers grown by MBE, and $\text{Pb}_{1-x}\text{Sn}_x\text{Se}$ ($x = 0\%$, 3%, 5%, 6%, 7%, 10%) layers grown by LPE on MBE-prepared substrates. The fundamental absorption edge energies for all alloys were derived from the transmission spectra. The refractive indices for $\text{Pb}_{1-x}\text{Sr}_x\text{Se}$ were calculated based on the interference fringes and the measured thicknesses of films.

The absorption edge energies of $\text{Pb}_{1-x}\text{Eu}_x\text{Se}$ alloys increase with temperature (at a rate of -0.5 meV/K for PbSe) but show a weaker dependence for alloys having a higher Eu content. They increase linearly with Eu contents at a rate of ~ 24 meV per % Eu, spanning a spectral range from 4.76 μm to 2.89 μm at room temperature for x up to 7.32%. The absorption edge energy of $\text{Pb}_{1-x}\text{Sr}_x\text{Se}$ initially increases linearly with Sr contents also at a rate of ~ 24 meV per % Sr for $x < 10\%$ but shows a quadratic dependence at higher Sr contents. The $\text{Pb}_{1-x}\text{Sr}_x\text{Se}$ alloys are expected to cover a spectral range from 4.71 μm to 1.79 μm at room temperature for x up to 26.1%. The refractive indices of these alloys decrease with increasing Sr contents. By controlling

the composition both electrical and optical confinements are expected for PbSrSe based heterostructures that will be used to fabricate diode lasers. The fundamental absorption edge energy is comparable for PbSe ($x=0$ in $Pb_{1-x}Eu_xSe$) grown by MBE on a Si(111) substrate and for PbSe ($x=0$ in $Pb_{1-x}Sr_xSe$) grown by MBE on a $BaF_2(111)$ substrate.

The $Pb_{1-x}Eu_xSe$ alloys exhibit increased absorption below the bandgap for samples with higher Eu contents (not observed for $Pb_{1-x}Sr_xSe$ system at higher Sr contents), the enhanced impurity and free carrier absorption below the bandgap in samples with higher hole concentrations, and the enhanced absorption above the bandgap also in samples with higher hole concentrations. These may be important considerations for designing lasers whose active region materials must have low absorption losses.

The absorption edge energies of the LPE-grown $Pb_{1-x}Sn_xSe$ layers increase with temperature uniformly across composition at a rate of ~ 0.48 meV/K. They decrease linearly with composition at a rate of ~ 8.7 meV per % Sn at both low temperatures and room temperature. For tin contents up to 10% these alloys can span a spectral range from $4.6 \mu m$ to $6.9 \mu m$ at room temperature and from $6.5 \mu m$ to $15 \mu m$ at low temperatures (109-125 k).

The absorption edge energy and refractive index dependence on composition for the three alloy systems (PbEuSe, PbSrSe, PbSnSe) can be manipulated to develop laser structures in which the PbSnSe serves as the active layer while the PbEuSnSe or PbSrSnSe serve as the confinement layers. The growth and characterization for such heterostructures may be an interesting future research project.

The growth of PbSnSe layers by LPE growth method on MBE-prepared PbSe/Si substrates is a novel technique with much improved growth morphology. An inherent problem is the tin out-diffusion during LPE growth due to the much higher growth temperature of PbSnSe than PbSe. More experimental work is needed to

explore the optical properties of these LPE layers and the suitability for using these materials to fabricate lasers.

While LPE-grown PbSe layers were crack free after growth all other samples containing tin were cracked. The in-plane tensile strain in the PbSe layer induced by its thermal expansion mismatch to the Si substrate was mostly absorbed by plastic deformation. The strain in the PbSnSe layers, however, was only partially absorbed by plastic deformation (the addition of tin caused solid solution hardening) and some residual strain was relieved through crack formation. It was observed that after cryogenic cycling the PbSe layer became cracked and the PbSnSe sustained more cracks. Interestingly the transmission spectra of these samples after a cryogenic cycle show red shifts (toward lower energy) of absorption edge energies, with the shift being greater for the binary than for the ternary layers. The amount of energy shifts was used to calculate the remaining residual strain in the crystal after growth, which was relieved through cracking due to cryogenic stress. The agreement between the calculated values and those obtained from HRXRD data indicates that transmission spectroscopy is a viable method of evaluating the residual strain in as-grown samples.

The photoluminescence experiments on PbSe, PbTe, PbSeTe, and PbSnSeTe (all are *n*-type) show unusual and strong PL at energies much above the bandgap energies and at temperatures from cryogenic to above room temperature. The main characteristics of the luminescence are strong temperature dependence of energy (similar to that of the band-to-band transitions), very narrow linewidth ($\ll 5 \text{ cm}^{-1}$), no thermal broadening of the linewidth, and insensitivity of the energy to alloy composition (metal or chalcogen exchange). A particularly interesting feature is the splitting of the energy by crystal field at low temperatures. This energy may originate from defect states associated with native anion vacancies in IV-VI materials. More research is needed to better understand the mechanism of the observed luminescence.

The optical pumping of the IV-VI layers by a diode laser focusing on a small area (mm^2) of the sample produced localized heating. The amount of this heating was graphically derived using two relations: laser driving current vs. PL energy and sample heat sink temperature vs. PL energy. The local heating effect may contribute to a greater degree of crystal field splitting of the PL energy. It may also be used to study the active region heating of a diode laser itself.

The observed luminescence makes the IV-VI semiconductors promising materials for fabricating room temperature lasers in the $2.6 \mu\text{m}$ region. The prospect of room temperature operation of such devices can lead to a breakthrough in the advancement of technology for mid-infrared tunable diode laser spectroscopy. Another possible future research project is to explore the aspect that the electrons occupying the defect states should experience little impurity ion scattering known in doped semiconductors.

The PL experiments were interrupted by the frequent repairing of the Bruker FTIR spectrometer. A major repair and optical alignment of the system was performed by the Bruker engineer. Despite the much-improved optical system the resumption of the PL experiment had not been successful in duplicating the previous results. A cryogenic sorption pump, previously used to vacuum the cryostat housing the pump laser and the IV-VI sample, was substituted with a turbo pump. The optical bench of the spectrometer had been purged with compressed air instead of the purified dry nitrogen previously used. It is known that humidity can degrade performance of the hygroscopic KBr beamsplitter. It is highly probably that the overlapping of the PL energies by water absorption bands contributed to the failure to observe the previously seen PL energy.

The characterization of tunable diode lasers is essential for their utilization as high-resolution radiation sources in molecular spectroscopy. Emission from a commercially available PbEuSe based diode laser was fully characterized over a range

of heat sink temperatures, from 90 K to 116 K, and laser injection currents, from 370 mA to 950 mA. This IV-VI laser exhibited several regions of strong single cw mode emission (as wide as 4 cm^{-1}) between 1848 cm^{-1} ($5.41\text{ }\mu\text{m}$) and 1989 cm^{-1} ($5.03\text{ }\mu\text{m}$) in the above temperature range. Multiple gas species, such as NO, COF₂, and H₂O have been measured using this single device as radiation source in a homemade laser spectrometer. While still requiring cryogenic cooling, the wide cw tuning characteristics make this device more versatile than the quantum cascade lasers.

From the characterization of laboratory-grown materials to commercial laser device, this work shows that the potential of IV-VI semiconductors is yet to be fully realized. Much research should and needs to be carried out on this interesting and still emerging materials system.

BIBLIOGRAPHY

1. E. Guber and U. Kohler, "FTIR Spectroscopy for Analysis of Selected Exhaust Gas Flows in Silicon Technology", *J. Molecular Structure* **348**, 209 (1995).
2. H. Saito and H. Shirai, "Determination of Interstitial Oxygen Concentration in Oxygen-Precipitated Silicon Wafers by Low-Temperature High-Resolution Infrared Spectroscopy", *Jpn. J. Appl. Phys.* **34**, L1097 (1995).
3. P. J. McCann and Lin Li; J. E. Furneaux; R. Wright, "Optical Properties of Ternary and Quaternary IV-VI Semiconductor Layers on (100) BaF₂ Substrates", *Appl. Phys. Lett.* **66**, 1355 (1995).
4. I. Chao, P. J. McCann, W. L. Yuan, E. A. O'Rear, and S. Yuan, "Growth and Characterization of IV-VI Semiconductor Heterostructures on (100) BaF₂", *Thin Solid Films* **323**, 126 (1998).
5. H. K. Sachar, I. Chao, P. J. McCann, and X. M. Fang, "Growth and Characterization of PbSe, and Pb_{1-x}Sn_xSe on Si (100)", *J. Appl. Phys.* **85**, 7398 (1999).
6. X. M. Fang, I-Na Chao, B. N. Strecker, and P. J. McCann; S. Yuan; W. K. Liu; and M. B. Santos, "Molecular Beam Epitaxial Growth of Bi₂Se₃- and Tl₂Se-Doped PbSe and PbEuSe on CaF₂/Si (111)", *J. Vac. Sci. Technol. B* **16**, 1459 (1998).
7. Z. Feit, R. Woods, D. Kostyk, R. Papez, Y. A. Mantz, M. Cummings, and A. W. Mantz, "Measurements of the Refractive Index of PbEuTe in the 3–10- μm Region of the Infrared", *Appl. Optics* **32**, 966 (1993).
8. J. Faist, A. Tredicucci, F. Capasso, C. Sirtori, D. L. Sivco, J. N. Baillargeon, A. L. Hutchinson, and A. Y. Cho, "High-Power Continuous-Wave Quantum Cascade lasers", *IEEE J. Quant. Elect.* **34**, 336 (1998).
9. I. Chao, unpublished data.
10. E. D. Hinkley, "High-Resolution Infrared Spectroscopy with A Tunable Diode Laser", *Appl. Phys. Lett.* **16**, 351 (1970).
11. Laser Components GmbH, Olching, Germany.
12. Laser Photonics, Andover, Massachusetts.
13. RMT Ltd., Moscow, Russia.
14. H. C. Sun, V. Patel, B. Singh, C. K. Ng, E. A. Whittaker, "Sensitive plasma etching endpoint detection using tunable diode laser absorption spectroscopy", *Appl. Phys. Lett.* **64**, 2779 (1994).

15. P. J. McCann, "High Temperature Semiconductor Diode Laser", U. S. Patent Number 5,454,002, Issued September 26, 1995.
16. K. R. Lewelling and P. J. McCann, "Finite-Element Modeling Predicts Possibility of Thermoelectrically Cooled Lead-Salt Diode Lasers", *IEEE Photonics Technol. Lett.* **9**, 297 (1997).
17. I. Chao, unpublished data.
18. J. Faist, C. Gmachl, F. Capasso, C. Sirtori, D. L. Sivco, J. N. Baillargeon, and A. Y. Cho, "Distributed Feedback Quantum Cascade Lasers", *Appl. Phys. Lett.* **70**, 2670 (1997).
19. R. U. Martinelli, "Mid-infrared wavelengths enhance trace-gas sensing", *Laser Focus World*, March, **77** (1996).
20. Z. Feit, M. McDonald, R. J. Woods, V. Archambault, and P. Mak, "Low Threshold PbEuSeTe/PbSe Separate Confinement Buried Heterostructure Diode Lasers", *Appl. Phys. Lett.* **68**, 738 (1996).
21. D. W. McAlister, P. J. McCann, H. Z. Wu, and X. M. Fang, "Fabrication of Thin Film Cleaved-Cavities Using a Bonding and Cleaving Fixture". Accepted for publication in IEEE Photonics Technology Letters, 1999.
22. P. R. Griffiths and J. A. de Haseth, Fourier Transform Infrared Spectrometry, John Wiley & Sons, 1986.
23. L. S. Rothman, J. Schroeder, A. McCann, R. R. Gamache, R. B. Wattson, J.-M. Flaud, A. Perrin, V. Dana, J.-Y. Mandin, A. Goldman, S. Massie, P. Varanasi, and K. Yoshino, "The HITRAN molecular spectroscopic database and HAWKS (HITRAN atmospheric workstation)", *J. Quant. Spectrosc. Radiat. Transfer* 1997.
24. M. Tacke, B. Spanger, A. Lambrecht, P. R. Norton, and H. Böttner, "Infrared Double-Heterostructure Diode Lasers Made by Molecular Beam Epitaxy of $Pb_{1-x}Eu_xSe$ ", *Appl. Phys. Lett.* **55**, 2260 (1988).
25. B. Spanger, U. Schiessl, A. Lambrecht, H. Böttner, and M. Tacke, "Near-Room Temperature Operation of $Pb_{1-x}Sr_xSe$ Infrared Diode Lasers Using Molecular Beam epitaxy Techniques", *Appl. Phys. Lett.* **53**, 2582 (1988).
26. A. Lambrecht; N. Henes; B. Spanger, S. Kuhn, H. Böttner, M. Tacke; and J. Evers, "Molecular Beam Epitaxy of $Pb_{1-x}Sr_xTe$ for the Use in IR Devices", *J. Cryst. Growth* **108**, 301 (1991).
27. H. Zogg, A. Fach, C. Maissen, J. Masek, and S. Blunier, "Photovoltaic Lead-Chalcogenide on Silicon Infrared Sensor Arrays", *Optical Engineering* **33m** 1440 (1994).

28. S. Yuan, H. Krenn, G. Springholz, and G. Bauer, M. Kriechbaum, "Large Refractive Index Enhancement in PbTe/Pb_{1-x}Eu_xTe Multiquantum-Well Structures", *App. Phys. Lett.* **62**, 885 (1993).
29. S. Yuan, H. Krenn, G. Springholz, and G. Bauer, "Dispersion of Absorption and Refractive Index of PbTe and Pb_{1-x}Eu_xTe ($x < 0.05$) Below and Above the Fundamental Gap", *Phys. Rev.* **B47**, 7213 (1993).
30. Z. Shi, W. Chen, H. Song, B. Yu, and Y. Fu, "Infrared Transmission Spectra of MBE-Grown Pb_{1-x}Eu_xTe Films", *J. Infrared Millim. Waves* **10**, 101 (1991).
31. V. Mathet, P. Galtier, F. Nguyen-Van-Dau, G. Padeletti, and J. Olivier, "A Microstructural Study of Crystalline Defects in PbSe/BaF₂/CaF₂ on (111) Si Grown by Molecular Beam Epitaxy", *J. Cryst. Growth* **132**, 241 (1993).
32. P. J. McCann, X. M. Fang, W. K. Liu, B. N. Strecker, and M. B. Santos, "MBE Growth of PbSe/CaF₂/Si(111) Heterostructures", *J. Cryst. Growth* **175/176**, 1057 (1997).
33. Optical Design Data, Janos Technology Inc., Townshend, Vermont.
34. J. N. Zemel, J. D. Jensen, and R. B. Schoolar, "Electrical and Optical Properties of Epitaxial Films of PbS, PbSe, PbTe, and SnTe", *Phys. Rev.* **140**, A330 (1965).
35. A. J. Strauss, "Inversion of Conduction and Valence Bands in Pb_{1-x}Sn_xSe Alloys", *Physical Review* **157**, 608 (1967).
36. H. Preier, "Recent Advances in Lead-Chalcogenide Diode Lasers", *Appl. Phys.* **20**, 189 (1979).
37. K. H. Herrmann, K. -P. Möllmann, and J. W. Tomm; H. Böttner, A. Lambrecht, and M. Tacke, "Some Band Structure Related Optical and Photoelectrical Properties of Pb_{1-x}Eu_xTe ($0 < x < 0.2$)", *J. Appl. Phys.* **72**, 1399 (1992).
38. V. E. Kondrashov, *Optika Fotocatodov* Vol. 17, Nauka, Moscow, 1976. Quoted in reference #30.
39. K. Seeger, Semiconductor Physics—An Introduction, Springer-Verlag Berlin Heidelberg 1982.
40. N. J. Parada and G. W. Pratt Jr., "New model for vacancy states in PbTe", *Phys. Rev. Lett.* **22**, 180 (1969).
41. Y. Shani, R. Rosman, and A. Katzir, "Calculation of the Refractive Indexes of Lead Chalcogenide Salts and Its Application for Injection Lasers", *IEEE J. Quantum electron.* **QE-21**, 51 (1985).

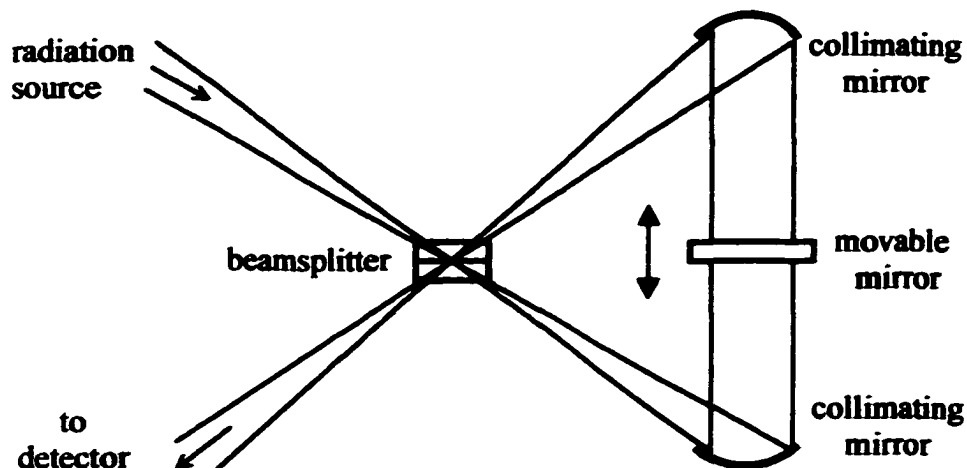
42. E. D. Palik, editor, Handbook of Optical Constants of Solids, Academic Press, 1985.
43. W. G. Opyd, "The Refractive Index of $\text{Pb}_{(1-x)}\text{Sn}_x\text{Te}$, $\text{Pb}_{(1-y)}\text{Sn}_y\text{Se}$, and $\text{PbS}_{(1-x)}\text{Se}_x$ and Theoretical Calculations for $\text{Pb}_{(1-x)}\text{Sn}_x\text{Te}$ and $\text{Pb}_{(1-y)}\text{Sn}_y\text{Se}$ 10.6 Micron Heterostructure Injection Lasers", Master's Thesis, Naval Postgraduate School, Monterey, Calif. (1973).
44. N. Suzuki, K. Sawai, and S. Adachi, "Optical Properties of PbSe", *J. Appl. Phys.* **77**, 1249 (1995).
45. P. K. Cheo, editor, Handbook of Solid-State Lasers, Marcel Dekker, New York, 1989.
46. P. Klocek, editor, Handbook of Infrared Optical Materials, Marcel Dekker, Inc., New York, 1991.
47. H. A. Macleod, Thin-Film Optical Filters, Macmillan, New York, 1986.
48. H. Zogg and M. Hüppi, "Growth of High Quality Epitaxial PbSe onto Si using a (Ca, Ba) F_2 Buffer Layer", *Appl. Phys. Lett.* **47**, 133 (1985).
49. H. Zogg, C. Maissen, J. Masek, S. Blunier, A. Lambrecht, and M. Tacke, "Heteroepitaxial $\text{Pb}_{1-x}\text{Sn}_x\text{Se}$ on Si Infrared Sensor Array with 12 μm Cutoff Wavelength", *Appl. Phys. Lett.* **55**, 969 (1989).
50. H. Z. Wu, X. M. Fang, R. Salas Jr., D. McAlister, and P. J. McCann, "Transfer of PbSe/PbEuSe Epilayers Grown by MBE on BaF_2 -coated Si(111)", accepted for publication in *Thin Solid Films*, 1999.
51. P. Muller, A. Fach, J. John, A. N. Tiwari, H. Zogg, and G. Kostorz, "Structure of Epitaxial PbSe Grown on Si(111) and Si(100) without a Fluoride Buffer Layer", *J. Appl. Phys.* **79**, 1911 (1996).
52. B. S. Strecker, P. J. McCann, X. M. Fang, R. J. Hauenstein, M. O'Steen, and M. B. Johnson, "LPE Growth of Crack-Free PbSe Layers on Si (100) using MBE-Grown PbSe/ BaF_2 / CaF_2 Buffer Layers", *J. Electron. Mater.* **26**, 444 (1997).
53. O. Madelung, editor, Semiconductors Other Than Group IV and III-V Compounds, p.44, Springer, Berlin, 1992.
54. P. J. McCann, J. Fuchs, Z. Feit, and C. G. Fonstad, "Phase Equilibria and Liquid Phase Epitaxy Growth of PbSnSeTe Lattice-Matched to PbSe", *J. Appl. Phys.* **62**, 2994 (1987).
55. T. C. Harmon, A. R. Calawa, I. Melngailis, and J. O. Dimmock, "Temperature and Compositional Dependence of Laser Emission in $\text{Pb}_{1-x}\text{Sn}_x\text{Se}$ ", *Appl. Phys. Lett.* **14**, 333 (1969).

56. J. W. Tomm, L. Werner, D. Genzow, K. Herrmann, D. Schikora, and J. Griesche, "Experimental Evidence of Strain-Induced Gap Shifts in PbTe Epitaxial Layers by Photoluminescence", *Phys. Status Solidi A* **106**, 509 (1988).
57. D. Eger, M. Oron, A. Zussman and A. Zemel, "The Spectral Response of PbTe/Pb_{1-x}Sn_xTe Heterostructure Diodes at Low Temperatures", *Infrared Phys.* **23**, 69 (1983).
58. P. J. McCann, S. Aanegola, and J. E. Furneaux, "Growth and characterization of thallium and gold doped PbSe_{0.78}Te_{0.22} layers lattice matched with BaF₂ substrates", *Appl. Phys. Lett.* **65**, 2185 (1994).
59. T. C. Harman, "Control of imperfections in crystals of Pb_{1-x}Sn_xSe and PbS_{1-x}Se_x", *J. Nonmetals* **1**, 189 (1973).
60. G. W. Pratt, Jr., "Vacancy and Interstitial States in the Lead Salts", *J. Nonmetals* **1**, 103 (1973).
61. L. A. Hemstreet, Jr., "Cluster Calculations of the Effects of Single Vacancies of the Electronic Properties of PbS", *Phys. Rev.* **B11**, 2260 (1975).
62. L. A. Hemstreet, Jr., "Cluster Calculations of the Effects of Lattice Vacancies in PbTe and SnTe", *Phys. Rev.* **B12**, 1212 (1975).
63. O. A. Pankratov and P. P. Povarov, "Many-Electron Effects and Charge States of Vacancies in IV-VI Semiconductors", *Sov. Phys. Solid State* **30**, 508 (1988).
64. G. Brunthaler, K. Lischka and L. Palmetshofer, "Localized "Deep" Defect States in PbSe_xTe_{1-x} Mixed Crystals" in *Physics of Narrow Gap Semiconductors* edited by Rauluszkiewicz et al. Elsevier Scientific, Amsterdam, 1981, p. 458.
65. A. N. Veis and N. A. Suvorova, "Characteristic Features of the Defect Formation Process in Pb_{1-x}Sn_xSe (x≤0.06)", *Semiconductors* **32**, 397 (1998).
66. R. A. Stradling and P. C. Klipstein, editors, Growth and Characterization of Semiconductors, Adam Hilger, Bristol, 1990.
67. D. H. Chow, R. H. Miles, T. C. Hasenberg, A. R. Kost, Y.-H. Zhang, H. L. Dunlap, and L. West, "Mid-Wave Infrared Diode Lasers Based on GaInSb/InAs and InAs/AlSb Superlattices", *Appl. Phys. Lett.* **67**, 3700 (1995).
68. K. H. Herrmann, J. W. Tomm, S. Haertel, M. Tacke, and H. Böttner, "Observation of Higher Subband Emission from PbSe Two-Dimensional Layers", *IEEE J. Quant. Elect.* **31**, 1201 (1995).
69. P. J. McCann, K. Namjou, and I-Na Chao, "Using Mid-IR Lasers in Semiconductor Manufacturing", *MICRO* July/August, 93 (1999).

Appendix A

The Genzel Interferometer

The Genzel-type interferometer was first developed by Genzel in Germany and formed the basis of the FTIR spectrometer manufactured by Bruker. A schematic of the Genzel type interferometer is shown below.



This interferometer incorporates a double-sided movable mirror located midway between the two fixed collimating mirrors. The beamsplitter is located at a focal plane of the collimating mirrors. The collimating mirrors are also positioned such that the transmitted and the reflected beams from the beamsplitter travel colinearly toward each other. For this configuration the mirror displacement x results in an optical path difference of $4x$, compared to the value of $2x$ generated in a Michelson-type interferometer.

Appendix B

Frequency Modulation Imposed by Interferometer

The amplitude of any cosine wave of frequency f_v is described by $A(t) = A_o \cos(2\pi f_v t)$, where A_o is the maximum amplitude of the wave. A comparing of this expression to Equation (2.1) and substitute ζ by $V_{op} t$ gives the frequency of the cosine interferogram seen in Figure 2.1 (a)

$$f_v = \nu V_{op} \quad (B-1)$$

The frequency f_v is called modulation or Fourier frequency and is expressed in Hz (s^{-1}). For example, a $5 \mu\text{m}$ (or 2000 cm^{-1}) source radiation exiting the interferometer with a typical mid-infrared scan speed of 1.582 cm/s has a frequency of $3,164 \text{ Hz}$. It should be pointed out that the Fourier frequency is only a fraction of the original, unmodulated signal frequency. Using the numbers in the above example, the original frequency of the source radiation is $6 \times 10^{13} \text{ Hz}$, obtained by multiplying 2000 cm^{-1} times by the speed of light. It can be seen that the frequency of the source radiation has been stepped down by the interferometer from optical frequency to audio frequency for the ease of electronic data processing. The recovery of the Fourier frequencies, i.e., the computation of the spectrum of interest, is achieved by performing a Fourier transform on the interferogram.

Appendix C

Sampling and Spectral Aliasing

The mathematical model of an ideal sampler is the uniform impulse train $p(t)$

$$p(t) = \sum_{n=-\infty}^{+\infty} \delta(t - nT_s) \quad (\text{C-1})$$

where T_s is the sampling period and n is an integer. The resultant sampled signal $y(t)$ is the unsampled analog signal $x(t)$ multiplied by the uniform impulse train $p(t)$.

$$y(t) = x(t) \cdot p(t) = \sum_{n=-\infty}^{+\infty} x(t) \cdot \delta(t - nT_s) = \sum_{n=-\infty}^{+\infty} x(nT_s) \cdot \delta(t - nT_s) \quad (\text{C-2})$$

In actuality the continuous-time impulse function can never be realized. Instead, a sample/hold circuit is used to generate a discrete-time sequence $x[n]$, which should be a very close approximation of $x(nT_s)$. Since the continuous-time analysis is sufficient to illustrate the point ahead, it is thereof applied for simplicity purposes.

A Fourier transform is performed to obtain the spectrum $Y(\omega)$ of the sampled signal $y(t)$. In linear system analysis, multiplication of two functions in time domain corresponds to convolution of these two functions in the frequency domain. It can be shown [C1] that the Fourier transform of $y(t)$ results in

$$Y(\omega) = \frac{1}{2\pi} X(\omega) * P(\omega) = \frac{1}{T_s} \sum_{n=-\infty}^{\infty} X(\omega - n\omega_s) \quad (C-2)$$

where ω_s is the sampling frequency ($\omega_s = 2\pi/T_s = 2\pi f_s$); $X(\omega)$ and $P(\omega)$ are the Fourier transform pairs of $x(t)$ and $p(t)$, respectively. Clearly, the spectrum $Y(\omega)$ is comprised of the spectrum $X(\omega)$ of the original unsampled signal $x(t)$ and the replicas of $X(\omega)$ repeated with a periodicity of T_s , for all n . If there is no *a priori* knowledge of $X(\omega)$, then it is not evident from $Y(\omega)$ alone as to which component represents the spectrum of the original unsampled signal $x(t)$. The effect of sampling a hypothetical analog signal having a certain bandwidth (i.e., a polychromatic radiation) is illustrated in Figure C.1 for two cases where different sampling frequencies are used.

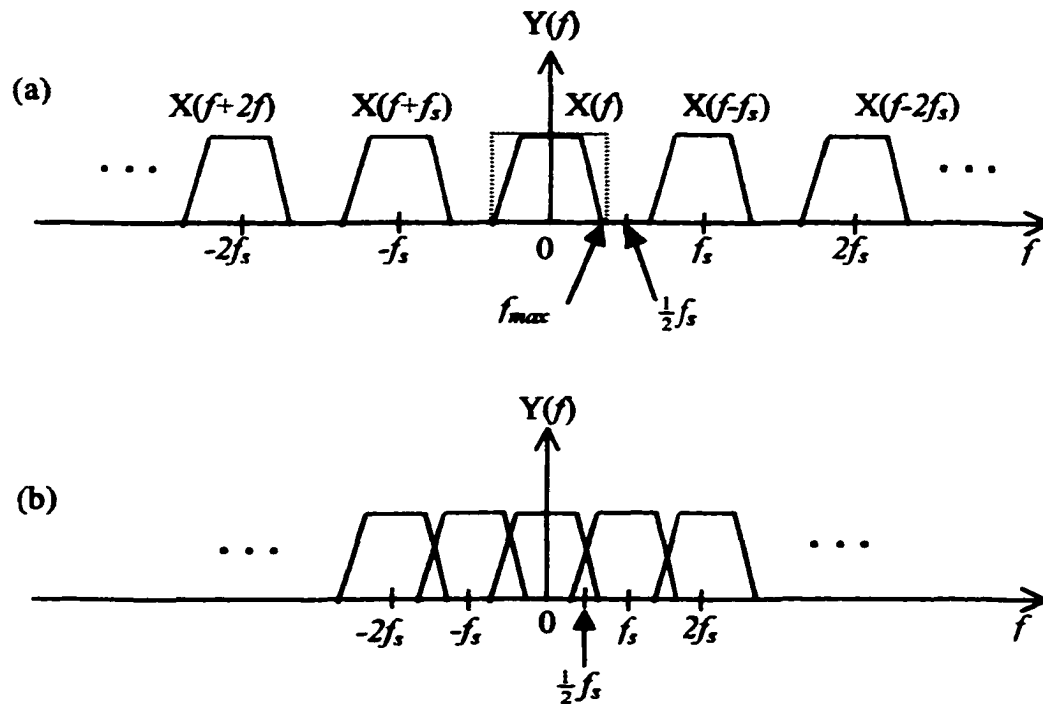


Figure C.1 Schematic of spectrum replication caused by sampling. Case (a) shows the spectrum sequences when f_s , the sampling frequency, is greater than twice of f_{max} , the highest frequency component in $X(\omega)$. The dotted box represents an idealized band-pass filter. Case (b) shows the overlapped spectrum sequence when $\frac{1}{2} f_s < f_{max}$.

For arbitrary values of f_s , the quantity $\frac{1}{2} f_s$ is called the Nyquist frequency or folding frequency. It defines the cutoff frequencies of the lowpass analog filters that are required in digital signal processing operations. Using a band pass filter with a cutoff at $\pm \frac{1}{2} f_s$, the original spectrum $X(f)$ in case (a) of Figure C.1 can be unambiguously recovered. In case (b), however, overlapping of spectra in the positive and negative frequency regions prohibits correct recovery of the original spectrum. In this case, spectral features would appear at incorrect wavenumbers, a phenomenon known as aliasing or folding. Because of the spectrum replication, it is critical that an appropriate sampling frequency be used to sample the analog signal of interest. According to the sampling theorem, an analog signal as a function of time or distance can be digitized unambiguously using a sampling frequency that is at least twice the bandwidth of the signal. In other words, the maximum allowable bandwidth of a signal must not exceed the Nyquist frequency or half of the sampling frequency.

When a hypothetical monochromatic analog signal is sampled, the recovered spectrum using sampling conditions applied in case (b) can look like what is shown in Figure C.2. The folded lines are symmetric with the true and duplicated lines with

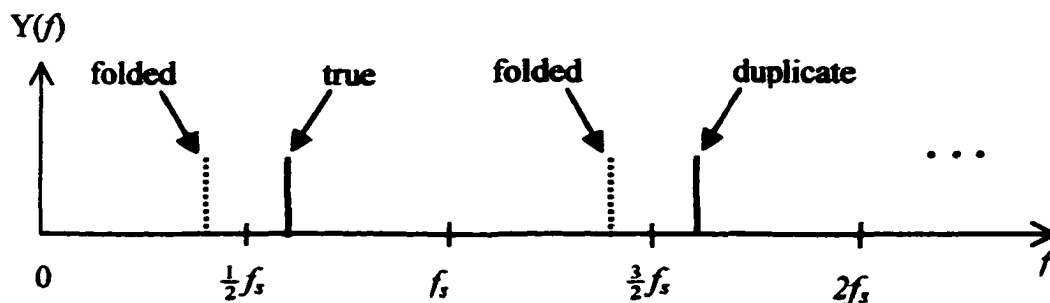


Figure C.2 Schematic of spectral folding of a hypothetical sinusoidal signal that is inadequately sampled.

respect to $\frac{1}{2} f_s$ and $\frac{3}{2} f_s$, respectively. The spectrum recovered using a filter with cutoff at $\frac{1}{2} f_s$ would show the folded line spectrum at a frequency to the left of $\frac{1}{2} f_s$, which is not the true spectrum. Spectral folding has been observed in atomic emission spectroscopy of alkali metals using the FTIR technique [C2]. The sodium doublet at 16,978 and 16,961 cm^{-1} were observed at the folded line positions of 14622 and 14639 cm^{-1} when the interferogram was sampled at 31600 cm^{-1} .

Reference:

- C1 L. B. Jackson, Signals, Systems, and Transforms, Chapter 4: Properties and Applications of the Fourier Transform, pg. 170, Addison-Wesley Publishing company, Inc. 1991.
- C2 J. F. Edwards and G. L. Schrader, *Appl. Spectrosc.*, **35**, 559(1981).

Appendix D

Important FTIR Measurement Parameters

The Bruker IFS 113 spectrometer's computing software and hardware are based on the early 1980's technology. Two versions of software, the ATS (older version) and the ATS88G (newer version), were used to perform infrared measurements using the spectrometer's ASPECT 2000 computer. Some of the software-controlled test parameters are described below.

A set of mirror velocities can be user specified by the parameter VEL (velocity). There are several scan velocity settings with rapid scan capacity for modulation in the mid IR range. A set of cutoff frequencies for the electronic filters can also be user specified by the parameters HPF (high pass filter) and LPF (low pass filter). Since in reality no filters have sharp cutoff values, the actual maximum allowed bandwidth (called the "folding limit" but not to be confused with spectral folding) is controlled by additional parameters "HFQ" (high frequency cutoff) and "LFQ" (low frequency cutoff). Values of HFQ and LFQ determine the folding limits wavenumber as the next divisor integer of the He-Ne laser wavenumber. For example, a HFQ of 5000 sets the high-frequency folding limit to 7950 cm^{-1} (15800 cm^{-1} divided by 2), and a LFQ of 1000 sets the low frequency folding limit to 987.5 cm^{-1} (15800 divided by 16). When the parameter SSP (sample spacing) is specified at the default value of -1 , the HFQ also sets the sampling frequency as twice the folding limit. After Fourier computation, only the spectrum in the wavenumber region between HFQ and LFQ is saved to the data file.

For mid-infrared measurements the manufacturer recommended parameter settings are: VEL = 11 (corresponding to an optical velocity of 1.582 cm/s), HFQ=5000 (folds at 7900), HPF=4 (low frequency cutoff at 550 Hz), LPF=1 (high frequency cutoff at 12500 Hz). The corresponding wavenumber cutoffs for the high and the low pass filters calculated using Equation (B-1) are 348 cm^{-1} and 7901 cm^{-1} , respectively.

Inappropriate parameter settings can result in spectral aliasing discussed in Appendix C, an example of which is shown in figure D.1. In this figure two spectra of

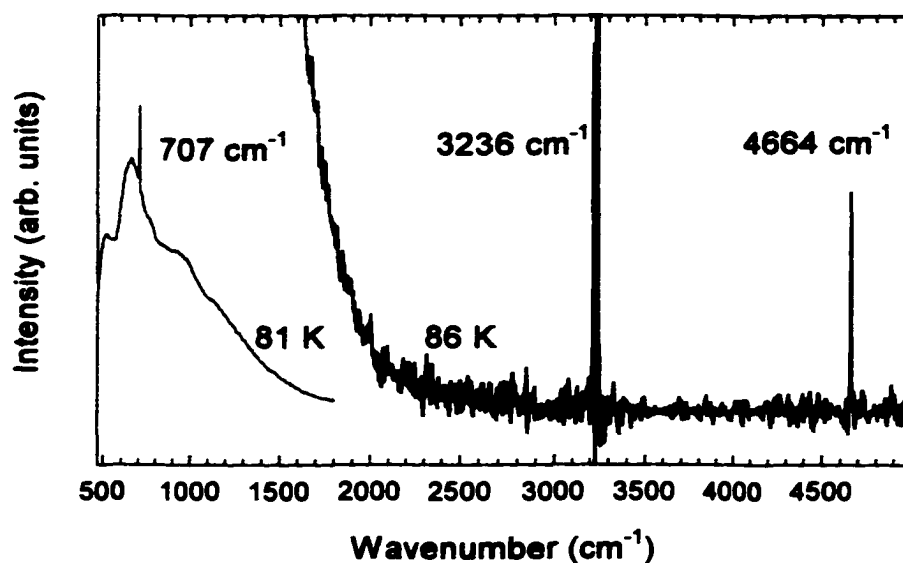


Figure D.1 Spectral aliasing seen in the emission (above threshold) spectra of a commercial PbEuSe diode laser. The manufacturer's specification for this laser shows an emission range of $3250\text{-}3275\text{ cm}^{-1}$ with threshold emissions at 3200 cm^{-1} (80 K) and 3220 cm^{-1} (85 K).

a PbEuSe based diode laser manufactured by Laser Components GmbH were obtained using different parameter settings. The right spectrum, obtained at 86 K, shows the actual laser emission at 3236 cm^{-1} . A spectral aliasing feature appears at 4664 cm^{-1} ,

which is the “fold back” of a spectral duplicate at 7186 cm^{-1} , assuming a sampling frequency of 3950 cm^{-1} . The left spectrum shows a feature at 707 cm^{-1} , near the peak of the 81 K blackbody radiation. This spectrum was obtained by purposely setting $\text{HFQ}=1800$, which prescribes the maximum wavenumber to be digitized unambiguously as 1975 cm^{-1} . Because the actual lasing wavenumber is above this limit, spectral aliasing at 707 cm^{-1} (“fold back” from 3236 cm^{-1}) occurs as a result of inadequate sampling. By correctly setting HFQ to at least 3500 (folding limit of 3950 cm^{-1} and sampling frequency of 7900 cm^{-1}), correct spectra without aliasing were obtained (not shown).

Appendix E

Emission Spectra of Tunable Diode Laser #42

The complete emission spectra of PbEuSe-based tunable diode laser #42 fabricated by RMT Ltd., Moscow, Russian are shown in the following pages. The general procedure for obtaining these spectra is described below. At a given laser heat sink temperature the laser driving current is increased slowly until the threshold lasing is observed on the computer screen. Then the current is increased 10-20 mA above the threshold current and the first above-threshold emission spectrum is recorded. The laser heat sink temperature is incremented by one degree and the laser driving current is incremented by 20 mA. The highest temperature measured and the highest current injected at a given temperature are below manufacturer recommended values.

